



Norges miljø- og
biovitenskapelige
universitet

Master's Thesis 2018 30 ECTS

Faculty of Science and Technology
Associate Professor Ingunn Burud

Assessment of Models Predicting the Maximum Surface Temperature in an Urban Setting Using VIS/NIR/IR Imaging from UAVs

Marija Vukovic

Environmental Physics and Renewable Energy
Faculty of Science and Technology

Acknowledgment

With this thesis I complete my master degree in Environmental Physics and Renewable Energy at the Norwegian University of Life Sciences (NMBU). The thesis is a result of the research activity of a group from NMBU and the Norwegian University of Science and Technology (NTNU) studying urban surfaces.

I would like to thank my supervisor, Ingunn Burud, for introducing me to the field of image analysis. It has been a pleasure to learn from her both on a professional and personal level. Her patience and willingness to help me gain a better understanding of the subject and for always being there despite her busy schedule are highly appreciated. I am also grateful to her for including me in her research activities with the rest of the team both at the university and internationally.

My gratitude goes to my co-supervisor, Thomas Kringlebotn Thiis. It has been a rewarding experience to listen to his insightful and interesting perspective on research problems. I would like to thank him for his help and support during the laboratory work with thermal cameras.

My appreciation also goes to Niki Gaitani, a member of the team from NTNU, for finding time to give me useful input.

Further, I would like to thank Arne Auen Grimenes and Jorge Mario Marchetti from NMBU for advice and support which were greatly appreciated during my whole study period at the university.

Last but not least, I would like to thank my parents, my sister and my partner who have not only believed and supported me unconditionally during these past months, but have been the reason why this thesis has come into being only three years after the enrolment at the university.

Ås, 14 May 2018
Marija Vukovic



Summary

Investigating surface temperature of the materials in urban settings is an important way of analyzing how urban heat islands can be mitigated. The present thesis investigates models for prediction of the maximum surface temperature of urban materials in Ymittos, Athens, based on image analysis of data collected in VIS, NIR and IR spectrum with a UAV in spring 2016 and summer 2017. The main aim of the thesis is to assess the potential and limitations of three models in predicting daily maximum surface temperature: model of apparent thermal inertia, linear regression of maximum surface temperature as a function of material's absorptivity and parametrization of maximum surface temperature. The model of apparent thermal inertia captures temperature differences based on moisture, but more research is necessary to conclude how well it performs on dry surfaces. Linear regression model and parametrization of maximum surface temperature give promising results. Furthermore, it has been shown with statistical methods that asphalt, marble, vegetation and concrete can be identified based on five bands: red, blue, green, NIR and NDVI. Since two different IR cameras were used in Athens in 2016 and 2017, *Optris 640* and *Flir Vue Pro*, the study is also based on the data collected in laboratory experiments which makes it possible to compare their performance. It has been shown that the former is more reliable and accurate. Correction factor for the latter has been obtained.

Abbreviations

ATI	Apparent thermal inertia
DSM	Digital Surface Model
FFC	Flat Field Correction
NDVI	Normalized Difference Vegetation Index
NIR	Near infra-red
IR	Infra-red
RGB	Red, green, blue
TI	Thermal inertia
TIR	Thermal infra-red
UAV	Unmanned Aerial Vehicle
UHI	Urban Heat Island
VIS	Visible

Contents

Acknowledgment	i
Summary	ii
Abbreviations	iii
1 Introduction	1
2 Theory	3
2.1 Electromagnetic radiation	3
2.1.1 Reflected radiation - VIS and NIR regions	4
2.1.2 Thermal radiation - IR region	4
2.1.3 Atmospheric effects in the TIR region	8
2.2 Surface property: Thermal inertia (TI) and apparent thermal inertia (ATI)	10
2.2.1 Different approaches to thermal inertia (TI)	10
2.2.2 Apparent thermal inertia (ATI)	13
3 Methodology	15
3.1 Data collection	15
3.1.1 Remote sensing in Athens	15
3.1.2 Laboratory experiments	17
3.2 Data processing	21
3.2.1 Processing of laboratory data	21
3.2.2 Processing of data collected in Athens	22
3.2.2.1 Processing in Pix4D	24
3.2.2.2 Light calibration and albedo	25
3.2.2.3 Emissivity correction and material classification with NDVI threshold, PCA, k-means and MLC	26
3.2.2.4 Solar irradiation maps	28
3.2.2.5 Temperature, TI and ATI maps	30
3.2.2.6 Parametrization of the maximum surface temperature T_{smax}	31

4 Results	33
4.1 Laboratory experiments on <i>FLIR Vue Pro</i> and <i>Optris 640</i>	33
4.1.1 Comparison between <i>FLIR Vue Pro</i> and <i>Optris 640</i>	33
4.1.2 The new conversion factor c_f	36
4.2 Emissivity correction and material classification with NDVI threshold, PCA, k-means and MLC	40
4.3 The maximum surface temperature T_{smax}	45
4.3.1 Weather conditions and solar irradiation	45
4.3.2 Temperature, albedo and ATI maps	49
4.3.3 The model based on thermal inertia (TI)	54
4.3.4 Parametrization of the maximum surface temperature T_{smax}	56
5 Discussion	58
5.1 Laboratory experiments on <i>FLIR Vue Pro</i> and <i>Optris 640</i>	58
5.1.1 Comparison between <i>FLIR Vue Pro</i> and <i>Optris 640</i>	58
5.1.2 Effects of the regressed conversion factor c_f on the data from Athens	60
5.2 Material classification with NDVI threshold, PCA, k-means and MLC	62
5.3 The maximum surface temperature T_{smax}	64
5.3.1 The model of apparent thermal inertia (ATI)	64
5.3.1.1 Comparison of the temperature and ATI maps based on the weather conditions	64
5.3.1.2 Material-wise comparison of the ATI maps of dry surfaces	66
5.3.1.3 The ATI model	70
5.3.2 The model based on thermal inertia (TI)	70
5.3.3 Parametrization of the maximum surface temperature T_{smax}	72
5.4 Overview	74
6 Conclusion	76
Bibliography	78
A Appendix	84

1. Introduction

Global warming and climate change as well as warmer cities and technological achievements have lead to an increased focus on the subject of urban heat islands (UHI) [1]. UHI is a phenomenon describing the higher rate of warming in the cities compared to the average global warming [2]. In other words, the cities have considerably higher temperature as opposed to the non-urbanized surroundings [1], [3]. It is caused by urban structures that absorb more radiation, heat added by human activities, traffic, industry and buildings. UHI in combination with ever more occurring heat waves results in decrease in human comfort, and in extreme scenarios, human mortality [2].

Considering this background, it is not surprising that "urban heat island studies probably still represent the majority of urban climate studies currently undertaken" [4]. Studying urban climatology implies that special emphasis needs to be given to the surface temperature [3]. Surface temperature affects, among others, the energy balance of the surface and energy exchanges affecting the comfort of city dwellers. It also affects the air temperature of the lowest layers of the urban atmosphere [3]. It is precisely these modifications in urban surfaces and atmosphere that lead to warmer thermal climate e.g. UHI [3].

As opposed to earlier ground observations, new methods of studying UHI have emerged based on thermal remote sensing technology using satellites and aircraft platforms [3]. The present study, however, is based on remote sensing with Unmanned Aerial Vehicle (UAV) used as sensor platform for small imaging sensors. This enables flexibility and, at the same time, obtaining images at a very high spatial resolution [5].

The present study uses high resolution images in visible (VIS), near infrared (NIR) and infra-red (IR) bands collected with a UAV during two study trips to a suburb of Athens, Municipality of Ymittos, in April 2016 and June 2017. The study is also based on the data collected in the laboratory. Due

to the fact that two different IR cameras were used in 2016 and 2017, *Optris* 640 and *Flir Vue Pro*, laboratory experiments have been performed during which the cameras were tested.

The analysis of the collected data focuses on three areas. The aim of the first part of the analysis is to compare and assess the performance of the two cameras as well as to draw conclusions about the possible implications on the images collected. The second part of the analysis assesses different unsupervised and supervised classification methods of the materials using the RGB and NIR images. The goal of this part of the study is to assess the classification methods with respect to the present investigation.

The results of the data analysis mentioned above is used in the third and main part of the thesis, the aim of which is to study the temperature of the surface materials in the urban setting. Here the focus is on three concepts and methods such as thermal inertia (TI), apparent thermal inertia (ATI) and parametrization of the maximum surface temperature. The aim is to assess how and whether it is possible to predict the maximum diurnal surface temperature of the urban materials as well as to acquire a better understanding of how the surface temperature of the materials behaves with respect to the mentioned parameters. It falls outside the scope of this thesis to evaluate how good every particular material is in order to contribute to UHI mitigation. The goal is directed towards investigating different parameters which can model the maximum surface temperature.

Parts of this work were presented in the article "Urban Surfaces Studied by VIS/NIR/IR imaging from UAV - Possibilities and Limitations" on the Sixth International Conference on Remote Sensing and Geoinformation of Environment, which took place on Cyprus 26-29 March 2018. The article is attached in Appendix A and will be referred to in the thesis.

2. Theory

The present chapter elaborates on the theoretical foundation which the following analysis is built upon. Firstly, the concept of electromagnetic spectrum is elaborated with emphasis on VIS, NIR and IR spectral regions. Secondly, the concepts of thermal inertia (TI) and apparent thermal inertia (ATI) as material properties are presented.

2.1 Electromagnetic radiation

The theory of radiation is founded on the postulate that "accelerated charges or changing electric currents give rise to electric and magnetic fields" [6] which transport energy and travel at the speed of light. They are called electromagnetic radiation or electromagnetic waves. Matter emits energy this way due to alternations in atomic or molecular electronic configurations. The postulate was laid by James Clark Maxwell in 1864 [6].

The transport of energy by electromagnetic waves is viewed in the light of quantum theory as proposed in 1900 by Max Planck [6]. It is considered to be the "propagation of a collection of discrete packets of energy called photons or quanta" [6]. The energy carried by a photon is given by

$$e = h \frac{c}{\lambda} \quad (1)$$

where h is Planck's constant ($6.63 \cdot 10^{-34} Js$), c is the speed of light ($3.00 \cdot 10^8 ms^{-1}$) and λ is the wavelength of the electromagnetic wave. The electromagnetic radiation spectrum comprises of a range of wavelengths "from less than $10^{-10} \mu m$ for cosmic rays to more than $10^{10} \mu m$ for electrical power waves" [6]. Waves with different wavelengths behave differently [6].

The spectrum of electromagnetic radiation originates in the Sun's nuclear reactions. It is first transmitted through space and then the atmosphere as it approaches the Earth's surface. In the interaction with the Earth's surface, the radiation can either be reflected or absorbed. Absorbed radiation is later re-radiated again as thermal energy [7]. Reflected radiation and thermal radiation are the very basis of the investigation undertaken in this thesis. In the following sub-chapters different parts of the electromagnetic spectrum defined by different wavelengths will be elaborated more closely: VIS, NIR and IR regions.

2.1.1 Reflected radiation - VIS and NIR regions

Isaac Newton, who was the first to investigate the optical properties of the visible region, found that it consists of three segments which are today known as blue, green and red. They correspond to the range of wavelengths 0.4-0.5 μm , 0.5-0.6 μm and 0.6-0.7 μm respectively. The color of an object that the human eye sees is defined by the color of the light that it reflects [7].

The region of the electromagnetic spectrum closest to the red part of the visible region is near infra-red (NIR) region. It comprises wavelengths in the range 0.72-1.30 μm [7], [8], [9]. From the optical point of view, radiation from this part of the spectrum up to 1.0 μm behaves analogously to the radiation in the visible region. This is why remote sensing equipment detecting radiation in NIR region up to 1.0 μm is designed similarly to the equipment detecting the visible radiation. Above that wavelength another type of detectors is necessary for the short infra-red region (SWIR) [7], (Ingunn Burud, private communication).

2.1.2 Thermal radiation - IR region

The portion of the electromagnetic spectrum which is not reflected but rather emitted is defined as the far infra-red (IR) region [7]. This type of electromagnetic radiation originating from "energy transitions of molecules, atoms and electrons of a substance" [6] is called thermal radiation and it is related to heat transfer. Transfer of energy in the form of heat by radiation is the fastest of the three ways of heat transfer since it takes place at the speed of

light. It can take place in vacuum and does not need presence of a material medium such as the case is with the other two heat transfer mechanism - conduction and convection [6].

A physical definition of the thermal infra-red (TIR) domain of the electromagnetic spectrum does not exist. It is defined differently by different authors [10], [8]. Definitions of thermal radiation that can be found include "the entire visible and infra-red (IR) radiation as well as a portion of the ultraviolet (UV) radiation [6]". It can be found in the literature that the TIR region comprises wavelengths from 7.0-1000 μm [7]. There is a broad agreement that TIR deals with emitted radiation as opposed to VIS and NIR domains that deal with reflected radiation [10], [8]. In the following analysis the definition used for the TIR region will be the latter one.

Accounting for the theory of radiation in the TIR region means accounting for the concept of blackbody radiation and thus Planck's law. Fundamental physics teaches that "every object at any given absolute temperature above 0 K emits thermal radiation" [11]. The object's temperature is the parameter solely responsible for the amount of the radiant power emitted by it. This aspect has lead to the term thermal radiation mentioned above [11].

In order to be able to analyze an object radiating energy, it is necessary to introduce the concept of *blackbody* e.g. "perfect emitter and absorber of radiation" [6]. It means that the surface of such an object emits the maximum possible amount of energy at a certain temperature and wavelength [6]. This amount of energy, referred to as spectral exitance [11] or spectral blackbody emissive power [6], radiated at the body's temperature T [K] for specific wavelengths λ [μm] is given by the famous Planck's law

$$E_{b\lambda}(T)d\lambda = \frac{2\pi hc^2}{\lambda^5} \frac{1}{e^{\frac{hc}{\lambda kT}} - 1} d\lambda \quad (2)$$

where $E_{b\lambda}$ [$\text{W m}^{-2} \mu\text{m}^{-1}$] is the spectral black body emissive power, h is Planck's constant ($6.63 \cdot 10^{-34} \text{ Js}$), c is the speed of light ($3.00 \cdot 10^8 \text{ ms}^{-1}$) and k is Boltzmann constant ($1.38 \cdot 10^{-23} \text{ J K}^{-1}$) [11].

By integrating Planck's law from zero to infinity one can represent the emissive power of a black body $E_b(T)$ [W m^{-2}] for the whole spectrum by the means of Stefan-Boltzmann law [11]

$$E_b(T) = \int_0^{\infty} E_{\lambda}(T) d\lambda = \sigma T^4 \quad (3)$$

where σ is Stefan-Boltzmann constant ($5.67 \cdot 10^{-8} W m^{-2} K^{-4}$) and $T [K]$ is the temperature of the black body. However, for the TIR imaging one detects only the radiation from the TIR spectrum and not the whole spectrum [11].

So far, the radiation theory from a surface defined as black body has been presented. However, such surfaces are "idealizations and no real object can emit this maximum thermal radiation at a given temperature" [11]. The radiation of a real body is given by scaling the radiation of a black body by a factor ϵ called emissivity. The definition of emissivity is "the ratio of the radiation emitted by the surface at a given temperature to the radiation emitted by a blackbody at the same temperature" [6]. Emissivity is therefore a value in the range $0 \leq \epsilon \leq 1$ [11].

Emissivity is a function of the wavelength, the direction of the emitted radiation as well as of the surface temperature [6]. It is given by

$$\epsilon(\lambda, \theta, \phi, T) = \frac{E(\lambda, \theta, \phi, T)}{E_b(\lambda, T)} \quad (4)$$

where $E(\lambda, \theta, \phi, T)$ is the emissive power of the real body, λ is a specified wavelength at which the radiation is emitted for the real body and black body, θ and ϕ are directions in which the radiation is emitted and $T [K]$ is the temperature of the real body and black body [6]. Averaging over all directions and wavelengths, one comes to equation

$$\epsilon(T) = \frac{E(T)}{E_b(T)} \quad (5)$$

which is called the total hemispherical emissivity. Thus, in the light of complexity that arises due to spectral and directional dependence of emissivity, one usually uses the total hemispherical emissivity (also referred to as average emissivity). In order to do that one assumes that the object in question can be approximated as a gray and diffuse body. The properties of a diffuse surface are independent of direction, while the properties of a gray surface are independent of wavelength. Emissivity thus becomes a constant value at a given temperature T [6].

Another approximation that the present analysis is founded on is that the materials and objects analyzed are opaque to thermal radiation. This means that radiation is considered to be surface phenomenon and that it is emitted and absorbed within the first few microns of the surface. Materials that this applies to are most materials encountered in the every day life such as metals, wood and rocks [6].

Another way to describe opaque materials is to say that they do not transmit radiation. The physical property of transmittance τ , a fraction of radiation transmitted through a surface, is in this case considered to be zero. When radiation strikes a surface, it can also be absorbed or reflected. The fraction of radiation absorbed is referred to as absorptivity α and the fraction reflected as reflectivity ρ [6]. Due to conservation of energy it is required that

$$\alpha + \rho + \tau = 1 \quad (6)$$

meaning that incident radiation on a surface can either be absorbed, reflected or transmitted [6]. This equation can be rewritten according to Kirchhoff's law stating that for an object "the emittance at a given wavelength is equal to its absorbance at the same wavelength" [10]

$$\alpha = \epsilon. \quad (7)$$

As mentioned earlier, opaque surfaces do not transmit radiation and in their case Eq. 6 can be written as [10]

$$\epsilon + \rho = 1. \quad (8)$$

Variations of Eq. 6 depending on what kind of absorbent, transmissive and reflective properties an object in question has, will be used in the following elaboration of the atmospheric effects.

2.1.3 Atmospheric effects in the TIR region

Theoretical background of thermal radiation elaborated in the last sub-chapter has paved the way into aspects of thermal imaging that need to be taken into account when retrieving the correct kinetic temperature of the imaged object. In order to understand them it is necessary to look into the operational aspects of a thermal camera.

The total radiation, Q [Wm^{-2}], received by a thermal camera is a sum of contributions from three radiation sources expressed in a following way

$$Q = Q_{obj} + Q_{refl} + Q_{atm} \quad (9)$$

where Q_{obj} is the radiation emitted from the target object, Q_{ref} is the radiation from the surroundings reflected of the target object and Q_{atm} is the radiation from the atmosphere [12]. Using Stefan-Boltzmann's law, radiation emitted from the object, Q_{obj} , is expressed as

$$Q_{obj} = \epsilon_{obj} \tau_{atm} \sigma T_{obj}^4 \quad (10)$$

where ϵ_{obj} is the emittance of the object, τ_{atm} is the transmittance of the atmosphere, σ is Stefan-Boltzmann constant and T_{obj} is the objects temperature [12]. Accordingly, radiation from the surroundings reflected by the target object, Q_{ref} , is given by

$$Q_{ref} = \rho_{obj} \tau_{atm} \sigma T_{refl}^4 \quad (11)$$

where ρ_{obj} is objects reflectivity and T_{refl} is the temperature of the surroundings reflected by the object [12]. Using Eq. 8 it is possible to rewrite Eq. 11 as

$$Q_{ref} = (1 - \epsilon_{obj}) \tau_{atm} \sigma T_{refl}^4. \quad (12)$$

In the same way the radiation emitted from the atmosphere, Q_{atm} , is expressed as

$$Q_{atm} = \epsilon_{atm}\sigma T_{atm}^4 \quad (13)$$

where ϵ_{atm} is the emittance and T_{atm} is the temperature of the atmosphere. Assuming that $\rho_{atm} = 0$ and using Eq. 6, Eq. 13 can be rewritten [12] as

$$Q_{atm} = (1 - \tau_{atm})\sigma T_{atm}^4 \quad (14)$$

Solving for object's temperature T_{obj} , Eq. 9 can be written as

$$T_{obj} = \sqrt[4]{\frac{Q - (1 - \epsilon_{obj})\tau_{atm}\sigma T_{refl}^4 - (1 - \tau_{atm})\sigma T_{atm}^4}{\epsilon_{obj}\tau_{atm}\sigma}}. \quad (15)$$

In order to perform the necessary corrections according to Eq. 15, the parameters that need to be set up in the camera are objects emissivity ϵ_{obj} , atmospheric transmittance τ_{atm} , reflected temperature T_{refl} and atmospheric temperature T_{atm} [13]. Since the atmospheric transmittance τ_{atm} is very close to one [12], the influence of the atmosphere is considered neglectable for thermal infrared imaging (8-14 μm) with UAV [14]. Object's emissivity, ϵ_{obj} , and the reflected temperature from the surroundings, T_{refl} , have a considerable influence on the temperature measurement. The correction of reflected temperature T_{refl} when obtaining the kinetic temperature of the measured object is particularly important when the measured object has low emissivity and thus, according to Eq. 8, high reflectance [12]. As it will be shown in subsequent chapters, the emissivity values of the materials studied in this analysis are close to 1. Thus the correction of the reflection temperature T_{refl} will be neglected.

Elaborating on the importance of emissivity correction is in order before concluding the subject of atmospheric effects on thermal radiation images. Emissivity correction is necessary because, as mentioned earlier, real materials have emissivity below one. The measured radiance temperature, T_{rad} of an object, is thus lower than the real kinetic (surface) temperature, T_{kin} [10]. Combining Eq. 3 and the definition of emissivity [10], this relationship can be written as

$$T_{rad} = \epsilon^{1/4}T_{kin}. \quad (16)$$

This means that, due to different emissivity values, temperature sensed with thermal camera, radiance temperature, can differ significantly even if objects have the same kinetic temperature. Therefore, in order to retrieve correct kinetic temperature of an object, an image needs to be corrected for emissivity [10].

2.2 Surface property: Thermal inertia (TI) and apparent thermal inertia (ATI)

The following section will lay the theoretical background for the concepts of thermal inertia (TI) and apparent thermal inertia (ATI). In Section 2.2.1, which deals with TI, it is necessary to carry through a detailed overview of the literature in order to arrive at the mathematical equation used later on in the analysis. Section 2.2.2 will elaborate on the concept of ATI.

2.2.1 Different approaches to thermal inertia (TI)

Thermal inertia P [$Jm^{-2}K^{-1}s^{-\frac{1}{2}}$] is defined as

$$P = \sqrt{k\rho c} \quad (17)$$

where k [$Wm^{-1}K^{-1}$] is thermal conductivity, ρ [$kg m^{-3}$] is density and c [$Jkg^{-1}K^{-1}$] is heat capacity.

An investigation of this research field shows that the concept of TI has been used in a wide range of research subjects in the last decades. It has been applied in, among other things, deducing soil heat flux, monitoring soil moisture, analyzing UHIs, studying lithology and producing geological maps [15]. A more detailed look into the literature on TI from these fields of study reveals that there is more than one approach to the mathematical Eq. 17. In fact, two approaches have been identified which appear to interpret the concept of TI in opposite ways.

According to one approach, TI is defined as a measure of the thermal response of a material to temperature changes [16], [17], [18], e.g. as a "resistance of

an object to its heating for 1 K” [19]. In the words of Tramutoli, it ”represents the measure of the material resistance to the temperature changes imposed by the outside, meaning that, for a given incoming heat flux, the variation of [material’s] temperature is inversely proportional to its thermal inertia” [20]. Schieldge et al refer to thermal inertia as ”a scalar quantity that provides a measure of a material’s ability to resist a change in temperature [21]. High temperature indicates low resistance, low thermal inertia, and low temperature indicates high resistance to heating, high thermal inertia. Studying thermal inertia implies studying these temperature changes occurring diurnally [19].

It was mentioned in the introduction that the concept of UHI implies that the cities have higher rate of warming and thus higher temperature than the surrounding areas. According to the approach to TI described above, one would expect that the studies of TI conducted on UHIs would claim lower values of TI in the cities compared to the rural areas. This is, however, not the case.

The study of urban climatology as of 1970’s focuses on the surface energy balance which in its simplest form, neglecting other terms such as the anthropogenic heat flux, can be written as

$$Q^* = Q_H + Q_E + Q_G \quad (18)$$

where Q^* is the net radiation, Q_H is the sensible heat flux, Q_E is the latent heat flux and Q_G is the ground heat flux [4], [22], [23]. As Roth states, the ”formation of the UHI is related to the energy balance of the urban area” [23]. The latent heat flux or evapotranspiration Q_E is reduced in the cities and because of this, incoming heat is transformed into sensible heat flux Q_H and ground heat flux Q_G .

Sensible heat flux Q_H and ground heat flux Q_G result in a warmer environment in the cities due to urban materials which are dense and have a relatively high heat capacity [23]. They also have ”the ability to efficiently accept and retain heat during daytime for periods longer than that of natural surfaces and release it at night” [23]. This aspect is exactly what the interpretation of TI comprises of in this approach. The term *thermal admittance* is sometimes used interchangeably with TI and it is referred to as the ”ability to store and release heat” [24]. Urban materials are thus said to have high thermal admittance while rural areas are said to have low thermal ad-

mittance [23], [24]. In the words of Ryu et al "the large thermal inertia of impervious materials means a high capability to store heat, which is closely related to the low moisture availability of impervious materials as well as the thermal properties such as heat capacity and thermal conductivity" [25].

The background of the latter definition of TI which is based on the surface energy balance is not to say that the first approach to TI is not based on the same premises. Also studies which base their approach on the first definition of TI use the surface energy balance as the starting point [21], [26]. The main difference between these two approaches, however, seems to be originating from the focus of their studies and the parameters affecting the analysis. The first definition describes the TI as a function of the diurnal temperature difference and in that way seeks to, for example, identify geologic materials [21] or assess the amount of soil moisture [20], [27], [28], [29]. The second approach seems to build the model of TI on more parameters. These are latent heat flux Q_E as mentioned earlier, but also canopy geometry and thermal properties (Niki Gaitani, private communication). Thus in this approach, urban surfaces are assessed through the lenses of the low latent heat flux Q_E and high ground heat flux Q_G e.g. higher absorbance of heat. The rural areas, however, are assessed through lower ground heat flux Q_G and higher latent heat flux Q_E e.g. better ability to release heat [23].

The first approach can also be found in connection to the study of UHIs [26]. Qin studies pavement surface temperature with the goal of mitigating UHI [26] since "[p]redicting the variation of the surface temperature of a pavement is [...] important for estimating the pavement performance and the urban thermal environment" [26]. But, in accordance to the comparison between the two approaches given above, Qin neglects latent heat flux Q_E and assumes that the surfaces are dry. Looking at the ground heat flux Q_G through the energy balance equation and the heat equation, the theoretical model relating thermal inertia P and maximum surface temperature T_{smax} has been derived [26], [30], [31] as

$$T_{smax} = \gamma \frac{(1 - \alpha)I_0}{P\sqrt{\omega}} + T_0 \quad (19)$$

where γ is the percentage of the absorption to the thermal conduction, α is the albedo, I_0 [Wm^{-2}] is the daily zenith solar irradiation, $\omega = 2\pi/24 \cdot 3600$ [s^{-1}] is the angular frequency and T_0 is a regressed constant [30].

This thesis will be focusing on the first approach to thermal inertia by using Eq. 19. The attempt will be made to use linear regression of this model to relate the TI of the materials in Ymittos to the development of their maximum surface temperature. The same way Qin neglects the latent heat flux Q_E in deducing Eq. 19, the data used for linear regression will be from sunny surfaces assuming they do not contain moisture.

2.2.2 Apparent thermal inertia (ATI)

Due to the fact that remote sensing methods are generally not adequate in acquiring information about parameters thermal conductivity k , density ρ , and heat capacity c [20], an approach has been developed to determine apparent thermal inertia, ATI [K^{-1}]. According to Kahle, the mathematical expression for ATI does not take into account topographic and atmospheric effects [32]. This approach has been employed in many studies in order to find soil moisture estimation by using satellite images [18], [19], [20], [27], [28], [29], [33], [34].

Apparent thermal inertia is given by

$$ATI = \frac{S(1 - \alpha)}{\Delta T} \quad (20)$$

where S is the solar correction factor, α is the albedo and ΔT is the diurnal temperature difference e.g. difference between the lowest nighttime temperature and the highest daytime temperature [16]. The solar correction factor S is given by

$$S = \sin(\phi) \sin(\delta) (1 - \tan^2(\phi) \tan^2(\delta))^{1/2} + \cos(\phi) \cos(\delta) \arccos(-\tan(\phi) \tan(\delta)) \quad (21)$$

where ϕ [rad] is the latitude and δ [rad] is the solar declination given by

$$\begin{aligned} \delta = & 0.006918 - 0.399912 \cos(\Gamma) + 0.070257 \sin(\Gamma) - 0.006758 \cos(2\Gamma) + \\ & 0.000907 \sin(2\Gamma) - 0.002697 \cos(3\Gamma) + 0.00148 \sin(3\Gamma). \end{aligned} \quad (22)$$

The argument Γ [rad] is the day angle given by

$$\Gamma = \frac{2\pi(n_d - 1)}{365.25} \quad (23)$$

where n_d is the day of the year [28].

Albedo α is defined as "the ratio of the reflected solar radiation to the incident solar radiation at the surface" [35]. It is given by

$$\alpha = \frac{\int_{\lambda_1}^{\lambda_2} \int_0^{2\pi} K_{up} \cos \theta d\omega d\lambda}{\int_{\lambda_1}^{\lambda_2} \int_0^{2\pi} K_{down} \cos \theta d\omega d\lambda} \quad (24)$$

where λ_1 and λ_2 is the range of wavelengths appropriate to the context of use, K_{up} and K_{down} [Wm^{-2}] is reflected and incident radiant intensity, θ is zenith angle, ω is solid angle. Average albedo is found by averaging over the daylight hours [36]. Albedo is thus a value between 0 and 1 meaning no and perfect reflectivity respectively [35].

The concept of ATI is "a measure of the temperature increase caused by the proportion of radiant energy that is absorbed by the Earth's surface" [28]. The solar correction factor S normalizes for variations in solar flux with latitude and solar declination over space and time [28]. The term $(1 - \alpha)$ represents "the quantity of heat absorbed by the surface" [20].

3. Methodology

This chapter accounts for the data collection (Section 3.1) and data processing (Section 3.2).

3.1 Data collection

The first part of this section (3.1.1) describes how the data collection was carried out by remote sensing using a UAV in Athens in 2016 and 2017. The second part (3.1.2) deals with data collection in the laboratory during which the two IR cameras used in Athens were tested.

3.1.1 Remote sensing in Athens

Municipality of Ymittos is a suburb of Athens, Greece. It occupies an area of 2.35 square kilometers, has a population of 33 628 inhabitants according to official census of 2011 and is situated 2.5 km southeast from the center of Athens. The climate here is typical for the Mediterranean region with dry and hot summers [5], [37], [38]. The study area is affected by UHI [5] and rehabilitation measures were undertaken in the period 2012-2014 in order to counteract it [37], [38].

The area of the study is shown in Fig. 3.1. It is important to mention that some of the images used in the data analysis will not exactly display the study area shown in Fig. 3.1. This is particularly the case for images obtained in 2016. There are two reasons for this. The first one is that the area mapped in 2016 was much smaller to begin with and thus cropping of those images that had to be carried through was performed on already smaller area. Secondly, as already mentioned, another camera was used in 2017 as opposed to 2016 which had a different lens.

The interest of the study are the materials numbered in Fig. 3.1. They

are numbered in the following way: 1) asphalt with cool coating, 2a) and 2b) old conventional asphalt, 3) new conventional asphalt, 4) marble and 5) concrete [37]. Additionally, vegetation will also be addressed in the analysis, even though the focus will be on the materials numbered here. All the roofs are masked out because they are not the object of the present analysis. The roofs differ considerably from each other and it is not possible to know what kind of materials each roof consists of. The roofs will thus be masked in every displayed image.



Figure 3.1: The study area in the Municipality of Ymittos, Athens, with the indication of where the different materials addressed in this study are: 1) asphalt with cool coating, 2a) and 2b) old conventional asphalt, 3) new conventional asphalt, 4) marble, 5) concrete [37].

The first study trip was conducted between 11 and 15 April 2016. The second study trip, with the aim of validating the data collected in 2016, was conducted between 19 and 21 June 2017. Table 3.1 illustrates on which days and at what times of the day the data used in this thesis was collected.

Table 3.1: Summery over the dates and times of the day when the data used in this thesis was collected in Athens.

Day	Morning	Midday	Afternoon	Evening
12 April 2016	06:30 am	12:30 pm		
19 June 2017	05:30 am 10:30 am	01:30 pm	05:30 pm	09:30 pm
20 June 2017	05:30 am	01:30 pm		10:30 pm
21 June 2017		01:30 pm		

Both years, an RGB camera and a *Canon SX2 80* RGB camera, where the blue channel was replaced by *Maxmax.com* with the NIR channel, were mounted on the UAV of type *DJI Phantom 4*. The time resolution was 2 seconds for the both cameras. A predetermined pattern was followed during the flight at about 100 m above the ground [5], [37]. In April 2016 IR camera *Opbris 640s*, hereafter referred to as *Opbris*, was mounted separately on the UAV and the same route was followed. The time resolution with the IR camera was 1 second. The spatial resolution was 2-3 cm. In June 2017 the same set-up was used with the same procedure apart from the IR camera which was for practical reasons replaced with *FLIR Vue Pro* camera, hereafter referred to as *FLIR*, with a 9 mm lens. The spatial resolution was 5-6 cm. In addition to the data collected with the UAV, measurements of weather conditions were carried out both years. Air temperature and the relative humidity were recorded continuously during the days when data was collected. The information about hourly radiation was obtained from the local weather station. A white plate reflecting 60% of the solar radiation was recorded with the RGB and NIR cameras for later light calibration [5], [37], [38].

3.1.2 Laboratory experiments

Since the two different IR cameras were used in order to collect the data about the study area in 2016 and 2017, it was necessary to compare and assess their performance. Laboratory experiments with the *FLIR* and *Opbris* were carried out in different settings while measuring the temperature of different objects as illustrated in Fig. 3.2, 3.3 and 3.4. The idea was to test the cameras' performance against a reference temperature in different ambient conditions while recording the temperature of different objects.

Image 3.2 shows the experimental set-up of Experiment 1 during which the temperature of a plate was measured with a temperature sensor and both IR cameras in the laboratory setting at the ambient temperature of 20°C. The *FLIR* camera, indicated with letter F, is connected to the drone on the left side of the image and *Optris*, labelled with O, is visible in the middle of the image. The green cable of the temperature sensor, S, was connected to the plate, P, of approximately constant temperature. The measurements obtained by the sensor were used as reference temperature. Recordings, R, made by *Optris* are shown on the computer screen on the right side of the image. Recordings by the sensor were also conducted on the computer, while the temperature measurements by the *FLIR* camera were done on a disk inside the camera. The temperature with both cameras was recorded at the same time every 30 seconds for approximately 3 hours.

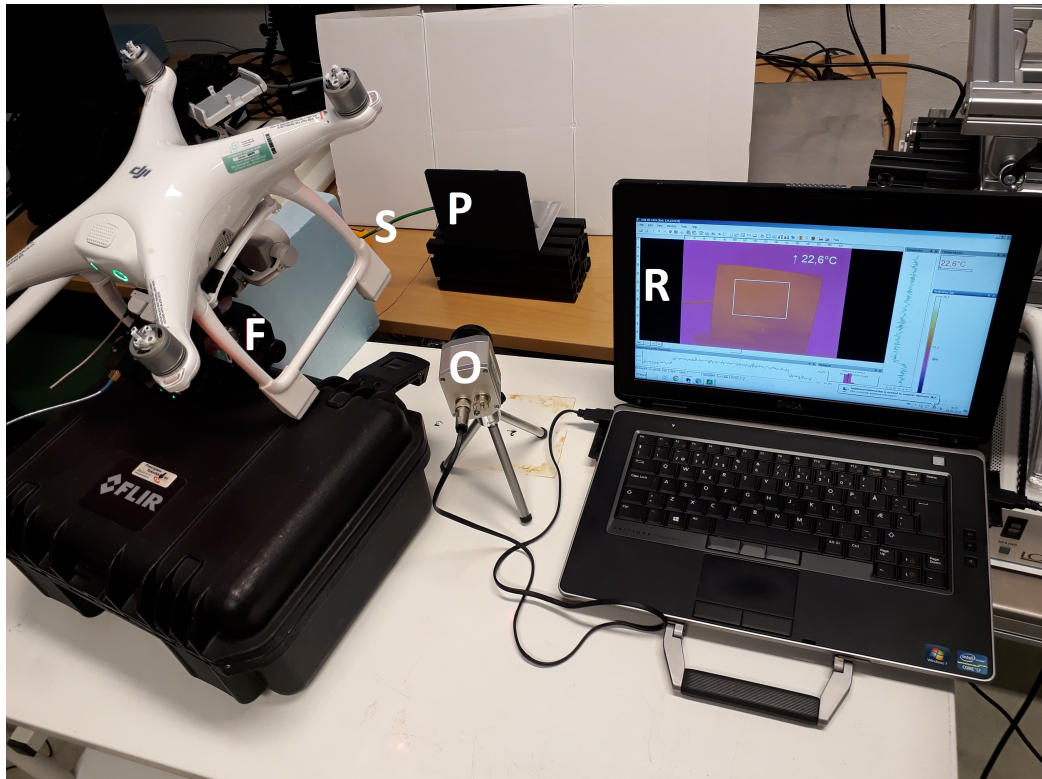


Figure 3.2: The set-up of Experiment 1 in which temperature of the plate was measured at the ambient temperature of 20°C.

After having carried out the experiment described above, the exactly same

set-up was used to test the cameras' performance at a different ambient temperature, 0°C, in Experiment 2. This is illustrated in Fig. 3.3. The same labels as in Fig. 3.2 are used to describe the equipment. The temperature sensor was also attached to the plate in this experiment, but it is not visible.

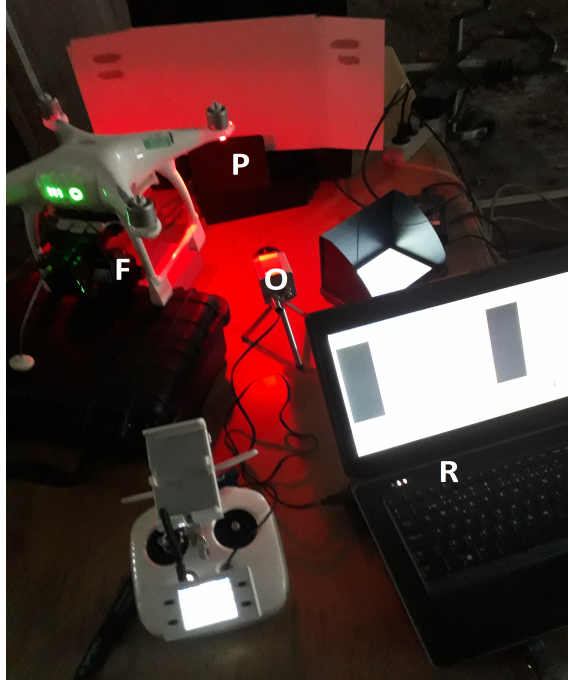


Figure 3.3: The set-up of Experiment 2 in which the temperature of the plate was measured at the ambient temperature of 0°C.

After the analysis of the data collected in the two experiments it became clear that more tests were necessary on objects with different temperatures. The most practical way to do that was to preheat a cup with boiling water and to cool down another cup outside in the snow for about 15 minutes. Approximately simultaneously as the first cup was filled with freshly boiled water, the second cup was filled with snow and brought inside. Experiment 3 was again conducted at room temperature at 20°C together with both cups and the same black plate as shown in Fig. 3.4. The two cups are labelled HC for *hot cup* and CC for *cold cup*. Due to heating and cooling of the two cups at room temperature, their temperature was changing and thus the experiment lasted only for 15 minutes. The measurements with the IR cameras were also this time recorded every 30 seconds.

The difference between this experiment and the two previous was the lack of possibility to connect the sensor to all three objects due to practical reasons. As it will be shown in Chapter 4, the two first experiments showed very little deviation in the measurements recorded with *Opbris* and the sensor. Thus the sensor remained connected to the plate as indicated in Fig. 3.4 and the measurements of the *Opbris* camera were considered accurate enough to be used as reference temperature for both cups.

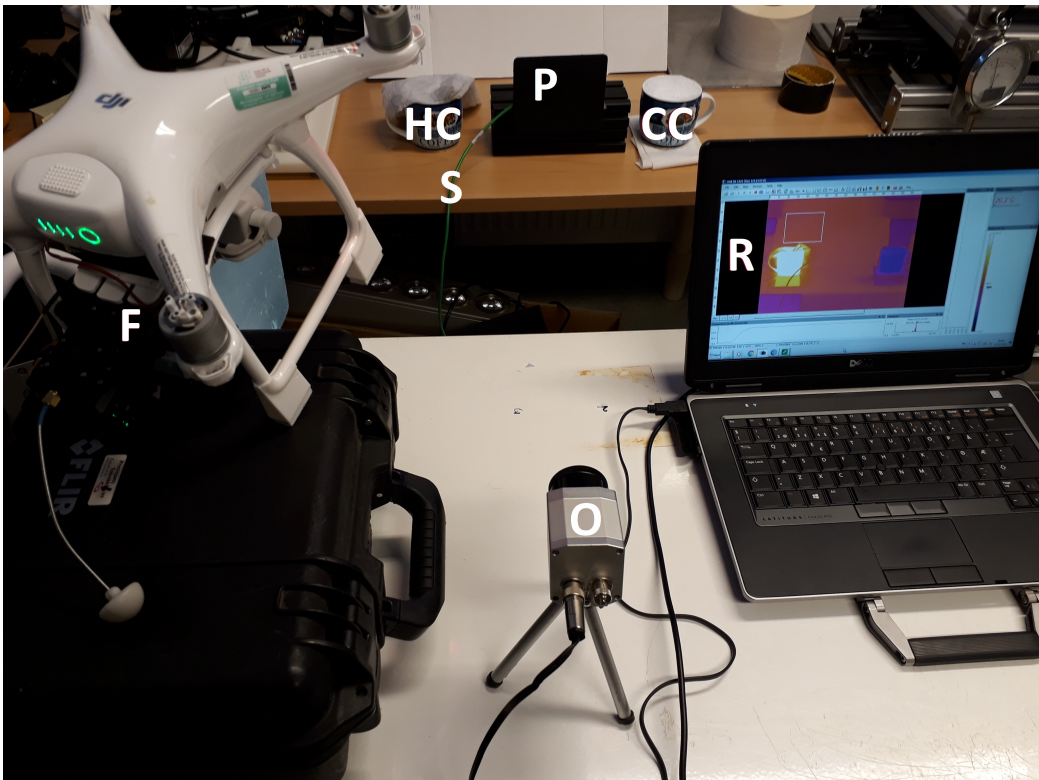


Figure 3.4: The set-up of Experiment 3 in which temperature of a hot cup, plate and a cold cup was measured at the ambient temperature of 20°C.

An overview of the experimental equipment, the objects measured and the camera parameters in the three experiments is shown in Table 3.2. Columns 2 and 3 show which measuring device measured which object. Columns 4 and 5 indicate how the parameters described in Section 2.1.3, ambient temperature $T_{ambient}$, atmospheric temperature T_{atm} , emissivity ϵ and transmittance τ , were set in the two cameras. The purpose with these experiments was not to correct the measurements for emissivity or reflectance by the surrounding

objects. The goal was to compare the two cameras operating in the same conditions and with the same parameters.

Table 3.2: Overview of the three experiments with respect to the measuring devices used, the objects measured as well as the parameters set in the two cameras.

Experiment	Device	Object	$T_{ambient}/$	ϵ	τ
			T_{atm} [°C]		
1) Fig. 3.2	Sensor	plate			
	<i>FLIR</i>	plate	20	1	1
	<i>Optris</i>	plate	20	1	1
2) Fig. 3.3	Sensor	plate			
	<i>FLIR</i>	plate	0	1	1
	<i>Optris</i>	plate	0	1	1
3) Fig. 3.4	Sensor	plate			
	<i>FLIR</i>	hot cup, plate, cold cup	20	1	1
	<i>Optris</i>	hot cup, plate, cold cup	20	1	1

3.2 Data processing

This section describes how the data was processed. Section 3.2.1 will describe how the laboratory data from the IR cameras was processed in order for it to be used in the processing of the IR images from Athens. Section 3.2.2 describes the processing of the data collected in Athens.

3.2.1 Processing of laboratory data

The images from the laboratory taken by both cameras were analyzed in Python. Temperature curves were obtained for every object measured in every experiment. As the results in Section 4.1 will show, *FLIR* camera is not accurate enough. The data from the three experiments was then used to create a regression model which would make it possible to retrieve correct temperature values from the *FLIR* images collected in Athens in 2017.

Temperature values are used in Celsius scale throughout this thesis. The pixel values obtained from *Optris* during the laboratory experiments as well as in Athens in 2016 are given in [°C] using TIF-format. However, using the same format, *FLIR* values needed to be converted in order to obtain

temperature values [°C]. The conversion formula is given by

$$T = p_v \cdot c_f - 273.15 \quad (25)$$

where T [°C] is temperature of the object, c_f is the conversion factor and p_v is the pixel value. The conversion factor c_f is a constant with the value 0.04 (FLIR technical support, private communication). The regression model used to retrieve temperature values for *FLIR* camera has lead to the adjustment of the conversion factor of $c_f = 0.04$. This will be dealt with in detail in Section 4.1 and 5.1.

Before concluding the methodology on the laboratory data, an aspect of the *FLIR* camera, which needs to be mentioned, is Flat Field Correction (FFC). FFC is "a process whereby off set terms are updated to improve image quality. This is done by presenting a uniform temperature (a flat field) to every detector element" [39]. The effect of FFC is that temperature readings from the same object will be somewhat different on an image taken just before and the other taken just after FFC (FLIR technical support, private communication). FFC has a time and a temperature component. Current settings are 4 minutes and 0.5 degrees (FLIR technical support, private communication). The temperature component will also be addressed in Chapter 4.

3.2.2 Processing of data collected in Athens

This section refers to the data processing steps based on the flowchart in Fig. 3.5, which is a further developed version of Fig. 3 in [5]. The descriptions here refer only to the processing of the data from June 2017. The data from April 2016 had been processed beforehand. The flowchart illustrates three starting points. The first one is based on RGB and NIR images, the second on IR images and the last one on the Digital Surface Model (DSM). It will be referred to Fig. 3.5 throughout the sections here. Section 3.2.2.1 accounts for how the RGB, NIR and IR maps were created in Pix4D out of the images taken with the UAV, while Section 3.2.2.2 deals with light calibration of the RGB and NIR maps. In Section 3.2.2.3 material classification is addressed. The last sections, 3.2.2.4, 3.2.2.5 and 3.2.2.6, describe how the irradiation, temperature and ATI maps were created and how linear regression and parametrization based on the temperature maps were performed.

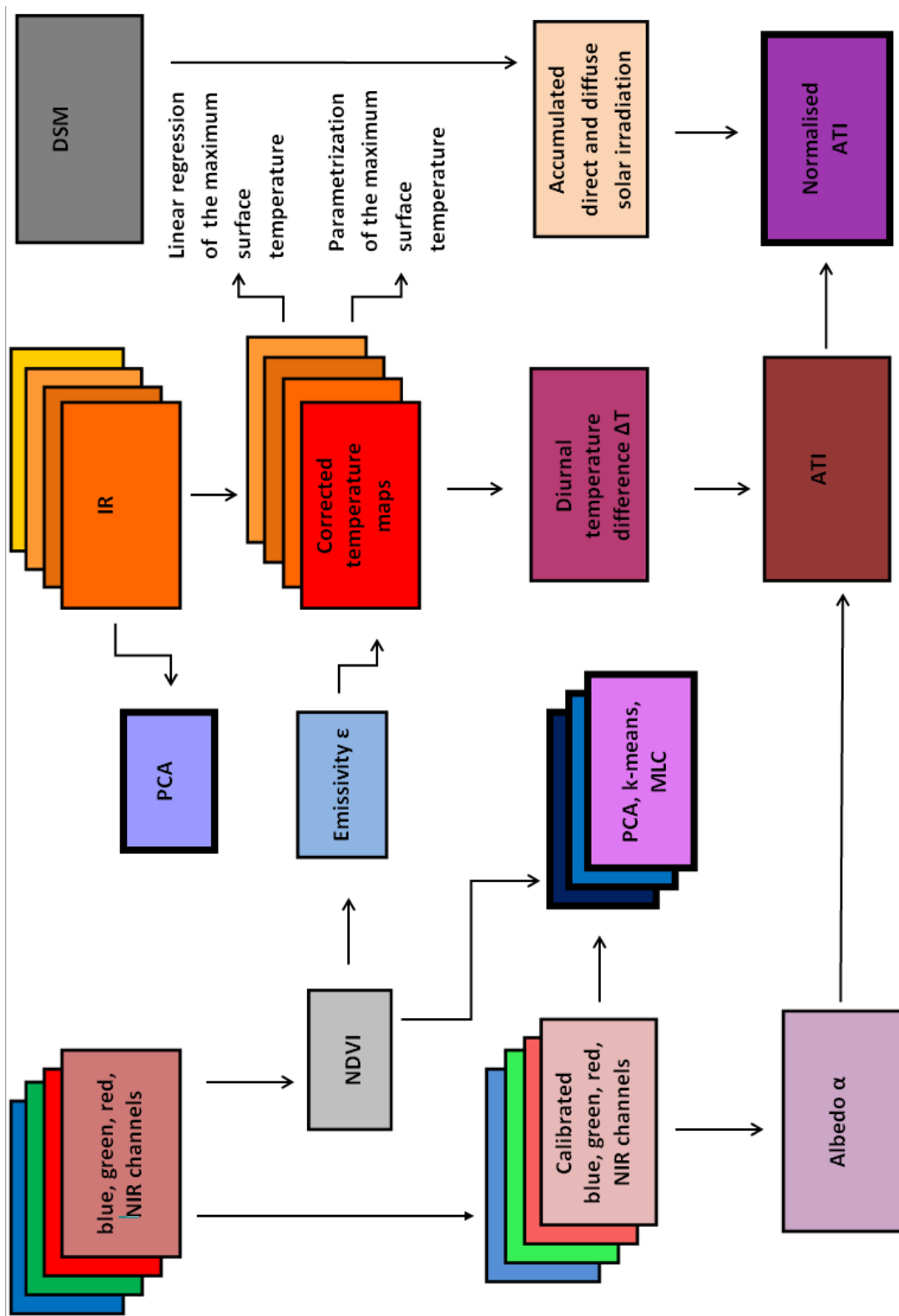


Figure 3.5: Flowchart illustrating the procedure for data processing.

3.2.2.1 Processing in Pix4D

The processing of the RGB, NIR and IR images collected in Athens started in Pix4D, a software with which one, among other things, obtains georeferenced maps from drone imagery [40]. First, it was necessary to georeference the images. The RGB and NIR cameras had build-in GPS loggers, but the IR camera did not. The GPS logger from the RGB camera was used to georeference the IR images.

Creating maps in Pix4D is based on orthorectification. This implies combining the images and correcting their perspective distortions [41]. The images need to have at least 60% overlap in order for the software to find key points and match them [42]. Several attempts based on trial and failure method were made in order to produce satisfactory results. Firstly, the adequate processing method had to be chosen based on the quality of the alignment of the images combined into a map. Another challenge in the case of IR images was the considerable differences in intensity values up to several degrees caused by FFC. These images were not used for processing.

Firstly, Pix4D creates a DSM. Each pixel in a DSM contains altitude information [43]. Based on it, orthomosaic and reflectance maps can be created which are 2D maps corrected for camera perspective. When creating them, each pixel value of the original images is weighted and averaged [44]. If the input images are multispectral or thermal, the reflectance maps are produced rather than orthomosaic maps. In this case one reflectance map is produced for each band [45].

Thus orthomosaic maps were obtained for the RGB and NIR images and reflectance maps for the thermal IR images. All together several RGB and NIR maps and nine IR maps from each drone flying session in June 2017 were created. One of the RGB and NIR maps was chosen for the analysis from the middle of the day with as little shadow as possible. Also one DSM map was used in the data analysis together with 10 IR maps, one from 12 April 2016 and nine from June 2017. The IR and DSM maps are 32 bits images, while the RGB and NIR maps are 8 bits images. The study area displayed with an RGB, NIR, DSM and IR map is shown in Fig. 3.6. The role of these maps in the data analysis procedure is shown in the flowchart in Fig. 3.5.

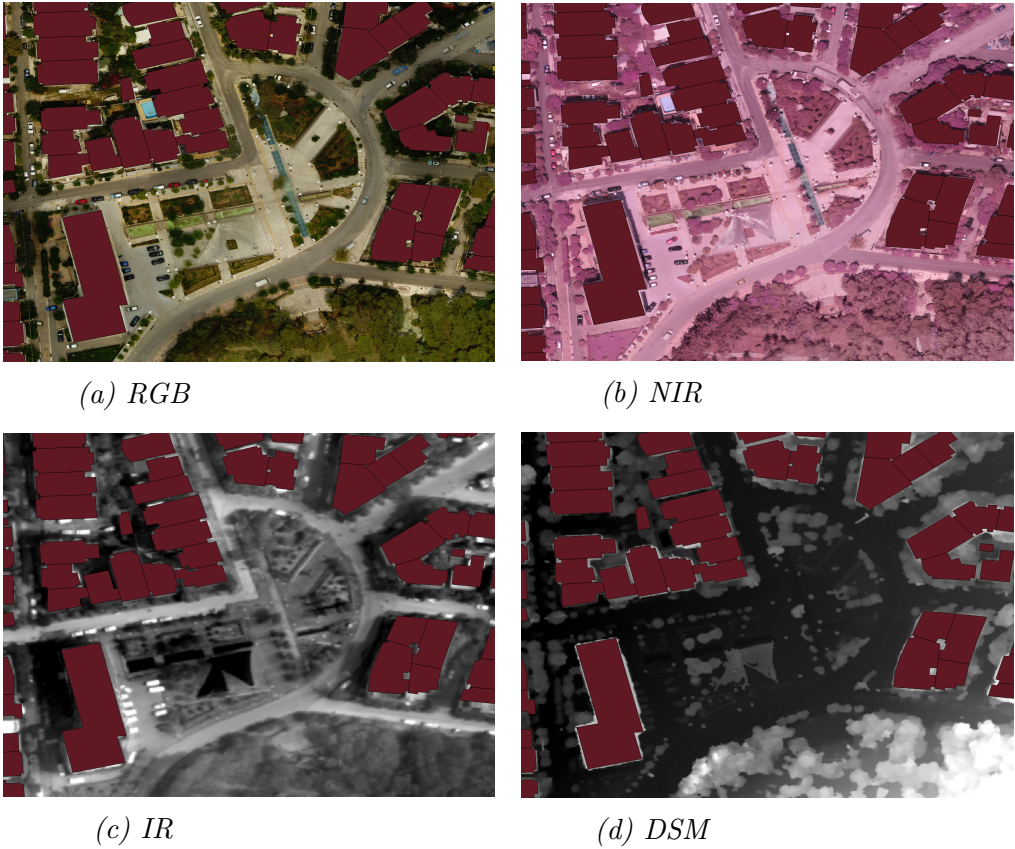


Figure 3.6: RGB, NIR, IR and DSM maps of the study area created in Pix4D.

3.2.2.2 Light calibration and albedo

As the flowchart in Fig. 3.5 indicates, the RGB and NIR maps had to be calibrated for light conditions. The correction of RGB and NIR maps was performed using an RGB and a NIR image of a white plate whose reflection was known, as illustrated in Fig. 3.7. The correction factor for a particular channel, $c_{channel}$, (red, green, blue or NIR) was calculated using

$$c_{channel} = \frac{\rho_{marble_{channel}}}{\rho_{white_{channel}}} \cdot 0.60 \quad (26)$$

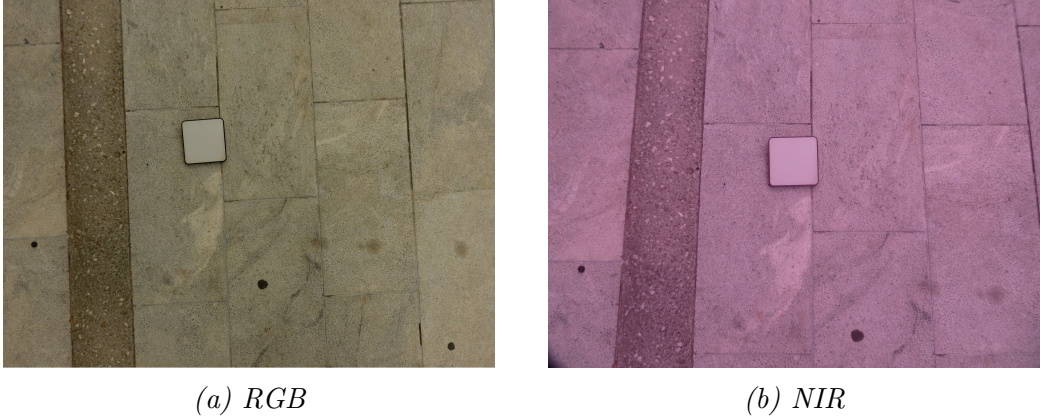


Figure 3.7: RGB and NIR images of a white plate with known reflection on marble.

where $\rho_{marble_{channel}}$ is the average of pixel values for marble for a particular channel from the corresponding image in 3.7, $\rho_{white_{channel}}$ is the average of pixel values for the white plate in that same channel and the value 0.60 is the known reflection of the white plate. With the correction factor $c_{channel}$ for every channel found in this way, the red, green, blue and NIR channels in the maps from Pix4D were corrected for light conditions.

The red, green, blue and NIR channels corrected for light effects were used to calculate the map of albedo α as indicated in flowchart in Fig. 3.5 based on

$$\alpha = 0.17b - 0.13g + 0.33r + 0.54nir \quad (27)$$

where b , g , r and nir is the reflectivity in the blue, green, red and NIR bands respectively. This method of calculating albedo is derived from remotely sensed reflectance [46]. The underlying assumption of this formula is that the surface is assumed to reflect equally in all directions (isotropically) [37].

3.2.2.3 Emissivity correction and material classification with NDVI threshold, PCA, k-means and MLC

Identification of materials labelled with numbers 1-5 in Fig. 3.1 was performed with different techniques: Normalized Difference Vegetation Index

(NDVI), Principal Component Analysis (PCA), k-means clustering and Maximum Likelihood Classification (MLC). The aim has been to assess their performance on the data collected in June 2017.

PCA was first performed on a stack comprised of nine IR maps obtained from the flying series in June 2017. PCA is an unsupervised classification algorithm with which dimensionality reduction on a data set is performed [47]. PCA performed on a stack containing several bands transforms it into a stack with uncorrelated features [48]. The result is a new data set of uncorrelated variables which displays information about the largest variation in the original data set [47]. Performing PCA on a stack of IR maps makes it possible to detect where the largest variation in temperature is.

The NDVI map was created with the red and NIR channels from the RGB and NIR maps. The formula for NDVI is given by

$$NDVI = \frac{nir - r}{nir + r} \quad (28)$$

where nir and r are the reflectivities in the red and NIR bands respectively. Different types of matter such as vegetation, soil, snow, rocks and water reflect differently in the visible and NIR spectra. This fact is used in the NDVI index to obtain values in the range [-1, 1] which can for example be used to study and monitor agricultural production. Values close to 1 are indicative of healthy plants because they reflect strongly in the NIR band, while values around 0 are indicative of rocks and soil [49].

This type of information contained in an NDVI map was used, as flowchart in Fig. 3.5 indicates, for emissivity correction of the IR maps using Eq. 16. Using the NDVI-threshold method [50], pixels with a particular range of NDVI values representing materials in the study area were assigned a certain emissivity value in the corresponding emissivity map. Measurements of the emissivity values in the study area were carried through in earlier studies giving emissivity of 0.95 for asphalt and marble and 0.97 for vegetation. Emissivity for concrete is not given [38]. As opposed to Eq. 5 in Section 2.1.2, emissivity is here considered to be constant despite the temperature.

The NDVI image and the corrected red, blue, green and NIR channels were stacked into a 3D matrix in order to make use of as many available channels as possible. This stack was used to see where the biggest variation in re-

flectivity could be detected by performing PCA. Material classification was performed with k-means and MLC with the aim to classify different materials in the study area based on the variation in reflectivity. For this the Semi-Automatic Classification Plugin (SCP) from the open-source system QGIS was used. This is indicated in Fig. 3.5.

K-means algorithm "is a technique that allows us to find groups of similar objects, objects that are more related to each other than to objects in other groups" [51]. It regroups pixels into clusters by recomputing the position of clusters' centroids (centers). This continues until the pixels belonging to a cluster are at a minimum distance to its centroid [51], [48]. MLC, however, is a type of supervised classification which was carried out based on region growing algorithm as an image segmentation method. Pixels with spectral distance below a certain threshold value were selected as a region of interest [52] (Appendix A). When training the data set, knowledge of the different materials in the study area, the RGB image from Fig. 3.6a and the results of PCA and k-means clustering were used as orientation. Several attempts were made with different number of classes. The result shown in Chapter 4 contains 10 classes.

3.2.2.4 Solar irradiation maps

Having an insight into the weather conditions would enable a better understanding of the surface temperature maps. The air temperature, the relative humidity and the direct daily irradiation were obtained as described earlier. At the same time, it was important to have the information about the incoming direct and diffuse solar irradiation not only on hourly basis for the whole day, but also pixel for pixel. In that way it would be possible to identify the parts of the study area that received a lot of incoming radiation and those that were predominantly in the shadow. This was necessary in order to conduct linear regression with respect to Eq. 19 and for parametrization of the maximum surface temperature.

The goal was achieved by using the DSM map as shown on the right side of the flowchart in Fig. 3.5. The first step was to run the DSM map through the UMEP plug-in [53] in QGIS in order to produce binary shadow maps having values 0 in the shadow and 1 in the sunlit areas as indicated in Fig. 3.8. The shadow maps were created for all four days (12 April and 19-21 June) with a resolution of one hour from the sunrise at 06:00 am until the hour of interest.

Secondly, maps of direct solar irradiation for every hour and every day were also created having only one constant value for the whole map. These direct solar irradiation maps were then corrected for the shadows by multiplying them with the shadow map for the same hour.

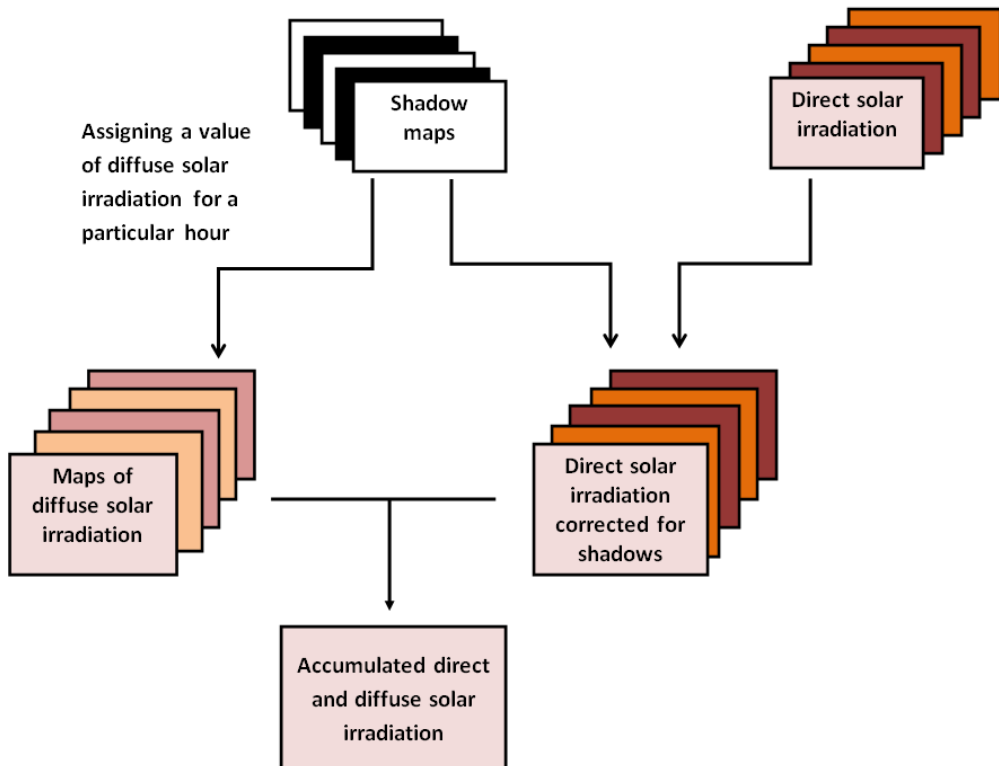


Figure 3.8: Method for creating maps of accumulated solar irradiation.

In addition, information about diffuse solar irradiation was obtained for Athens through the Clear Sky Model [54]. The next step was to create maps of diffuse solar irradiation by assigning the diffuse solar irradiation value for every hour to the shadowed areas. This meant that there were at the end two maps for each hour of each day up until the hour of interest: one with direct solar irradiation corrected for shadows and one with diffuse solar irradiation created from the shadow maps. At the end, the maps of direct and diffuse solar irradiation were added for every day to give one map of accumulated solar irradiation in each pixel up until the hour of interest.

3.2.2.5 Temperature, TI and ATI maps

IR reflectance maps obtained from Pix4D were first corrected with respect to the conversion factor c_f which was the result of the laboratory experiments of the *FLIR* camera as described in Section 3.2.1. After that the emissivity correction was done on the IR maps as described in Section 3.2.2.3. Thus the temperature maps for the nine flying sessions in June 2017 could be obtained.

They were further used to calculate the diurnal temperature difference ΔT maps, which are the maps of the temperature difference between the highest and the lowest temperatures of the day. The highest and the lowest temperatures of the day were recorded at 06:30 am and 12:30 pm in 2016 and 05:30 am and 01:30 pm in 2017. As shown in Fig. 3.5, based on the ΔT maps and the albedo maps, the map of ATI values could be generated for a day of interest. In addition, the map of accumulated solar irradiation was created as described above and normalized. By multiplying the ATI map for each day by the map of normalized solar irradiation for that same day, the ATI maps were corrected for solar irradiation and shadow. Differences between ATI images obtained in this way indicate that they are caused by other factors than solar irradiation. ATI maps will be used to analyze differences in temperature on a daily bases as well as material-wise differences considering the five material groups labelled in image 3.1.

The nine temperature maps from June 2017 were also used to illustrate how the temperature of the materials developed from early morning on 19 June until midday of 21 June. For that it was necessary to choose areas on the maps which received as much sunlight as possible during a day. Maps of accumulated irradiation until 05:00 pm were used to identify those areas. Since it was difficult to accomplish that for all five materials, it was possible to find one place for asphalt and marble which did not seem to be under shadow until 05:00 pm. Concrete did get some shadow until afternoon. Therefore, this part of the analysis will be based on three groups: asphalt, concrete and marble.

This procedure provided the basis for linear regression of the maximum surface temperature as a function of absorptivity according to Eq. 19. Linear regression was based on three temperature points obtained per material for concrete, asphalt and marble. They were obtained from temperature maps from 20 and 21 June at 01:30 pm as well as from 12 April at 12:30 pm. The temperatures from the middle of the day are the highest surface temperatures obtainable from the data. The temperature measurements from 19

June were not used here. This model assumes that there is no latent heat flux Q_E as mentioned in Section 2.2.1. It will be shown in Section 5.3.1 that the surface on 19 June was still moist and that latent heat flux Q_E is not possible to neglect that day.

3.2.2.6 Parametrization of the maximum surface temperature T_{smax}

An attempt has also been made to understand the diurnal development of the surface temperature based on the model by Bogren et al [55] and Lindberg et al [56], [57]. The model for estimating the temperature on sun-exposed surfaces is based on "linear relationship between maximum solar elevation and maximum difference between T_a and T_s during clear day conditions $T_{diffmax}$ " [56]. The variable T_a represents the air temperature, T_s the surface temperature and $T_{diffmax}$ is the maximum difference between them which occurs when T_s is at its maximum [56], [57]. This linear relationship model parametrizes the surface temperature according to

$$T_{diffmax} = \eta x + b \quad (29)$$

where x is the maximum solar elevation on a particular day while η and b are the regression constants. Such parameterization makes it possible to describe the surface temperature T_s on a clear day as a sinusoidal function [56]. Its "amplitude is taken from the linear relationship [...]" and the period for a certain day of the year is established based on the time between sunrise of the day of interest" [56] and the time when the maximum difference between T_s and T_a occurs [56]. The sinusoidal equation is written in the following way (Lindberg, private communication)

$$T_s = T_a + \eta x \sin\left(\frac{(t_{dec} - \lfloor t_{dec_{max}} \rfloor) - \frac{t_{sunrise}}{24}}{\frac{t_{max}}{24} - \frac{t_{sunrise}}{24}} \cdot \frac{\pi}{2}\right) + b \quad (30)$$

where t_{dec} is the decimal time, $\lfloor t_{dec_{max}} \rfloor$ is the largest integer of t_{dec} , $t_{sunrise}$ and t_{max} are the time of the sunrise and the time of the highest surface temperature respectively.

Equation 30 has been used to derive sinusoidal curves for asphalt, concrete

and marble based on the measurements obtained in June 2017. This implies using a trial and error technique to draw sinusoidal curves which fit the measurement points from that day because regression constants η and b are unknown. The regression constant b was set to -3 (Lindberg, private communication) and kept at that value while η was adjusted. The aim is to obtain η and thus Eq. 29 for all three materials. Lindberg et al provide parameterization equation for asphalt [56], [57] which will be used in order to compare the parametrization equation obtained for that material.

The measurement points will be used only from 20 June 2017 because that is when the weather conditions were favorable, e.g. as sunny as possible. Also in this part of the analysis it is important to choose sunlit areas. Therefore the focus will be on three groups of materials due to earlier mentioned difficulties in finding spots on the images without shadow. The solar elevation x on 20 June in Athens was found to be 75.44° [54]. Sunrise in Athens is at 06:00 am in June and the highest surface temperature was assumed to be around 03:00 pm. The reason for that is Fig. 4.21 shown in Section 4.3.3 which indicates that the maximum surface temperature of the materials probably occurred somewhere between 01:30 pm and 05:00 pm. Qin also points out that the maximum pavement surface temperature appears a couple of hours after the solar noon [26]. Solar noon is around 01:30 pm in Athens [58].

4. Results

The results in this chapter are presented in three main parts. Section 4.1 presents results concerning the laboratory experiments on *FLIR* and *Optris* cameras. Section 4.2 deals with the attempt to differentiate and identify materials based on the NDVI map, a stack of IR maps and a stack of blue, green, red, NIR and NDVI channels. Section 4.3 presents the surface temperature maps and the results of three approaches to predicting surface temperature: ATI, linear regression based on Eq. 19 and parametrization of the maximum surface temperature based on Eq. 30.

4.1 Laboratory experiments on *FLIR Vue Pro* and *Optris 640*

Section 4.1.1 displays the results from the laboratory experiments. In Section 4.1.2 these results are used to obtain a regression model for the conversion factor c_f .

4.1.1 Comparison between *FLIR Vue Pro* and *Optris 640*

The results of Experiments 1 and 2, the set-up of which is illustrated in Fig. 3.2 and 3.3, are shown in Fig. 4.1. The temperature measured by *FLIR*, *Optris* and the sensor connected to the black plate (reference temperature) are indicated by the blue, orange and green lines respectively. These two experiments show that the measurements by *Optris* are reliable compared to the temperature sensor. However, *FLIR* has a considerable offset compared to the reference temperature. The offset depends on the temperature of the object measured. The systematic error for the *FLIR* is +/- 5°C, while the error for *Optris* is +/- 2°C.

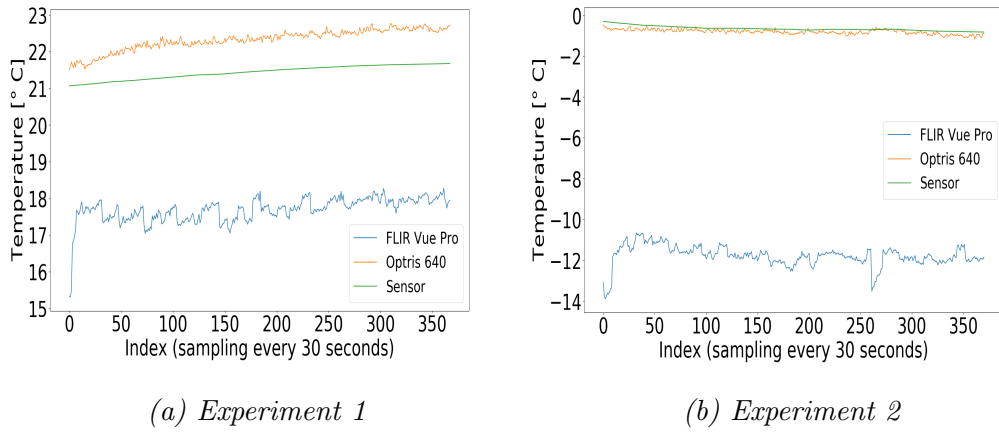


Figure 4.1: Temperature measurements of a black plate with *FLIR* and *Optris* at $T_{\text{ambient}} = 20^{\circ}\text{C}$ (Experiment 1) and $T_{\text{ambient}} = 0^{\circ}\text{C}$ (Experiment 2).

Due to the results indicating that *FLIR* offset depends on the temperature recorded, further measurements were conducted. The results of Experiment 3 with three objects having different temperatures, a hot cup, the black plate and a cold cup, are shown in Fig. 4.2a, 4.2b and 4.2c respectively. Measurements by the *FLIR* are shown with the blue line, *Optris* with the orange line and the sensor with the green line. In Fig. 4.2d the measurements by both cameras from Fig. 4.2a, 4.2b and 4.2c are shown together. The two top lines indicate the temperature of the hot cup (HC) measured by *FLIR* and *Optris* while the two middle and bottom lines indicate the temperature of the black plate (P) and of the cold cup (CC) respectively. It is confirmed in Fig. 4.2d that the difference between the measurements of the two cameras increases with lower temperature of the object measured.

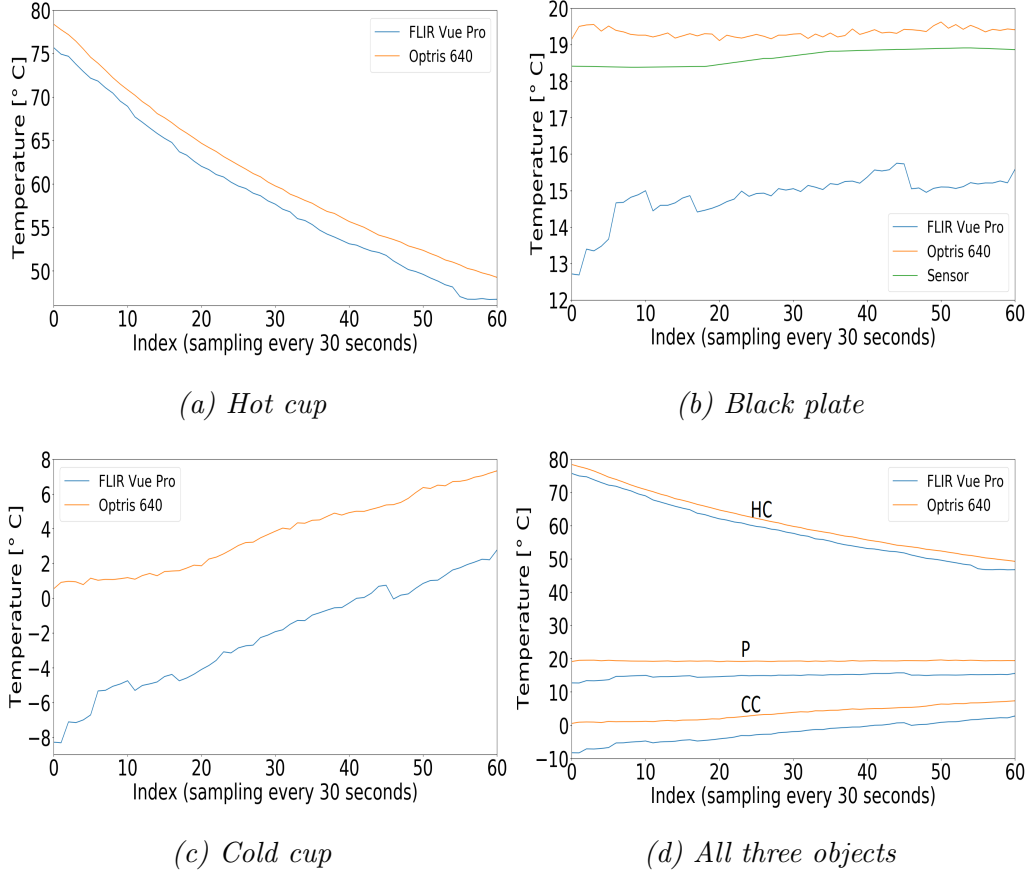


Figure 4.2: Temperature measurements from Experiment 3 in which the temperatures of a hot object, black plate and a cold object are displayed separately and together.

Numerical values have been drawn out from Fig. 4.1a, 4.1b and 4.2b for further analysis in Table 4.1. These are the values from the measurements of constant temperature of the black plate which will illustrate the tendencies in the measurements by *FLIR* and *Optris* cameras. An overview of the maximum, mean and minimum temperature T_{max} , T_m , T_{min} , are shown in columns 3, 4 and 5. The differences between the mean temperature of each camera and the sensor, ΔT_m , are shown in column 6. The last column of the table displays the biggest fluctuation F_{max} for each camera, meaning the biggest temperature rise or drop.

Table 4.1: Overview of the numerical values recorded from Fig. 4.1a, 4.1b and 4.2b.

Experiment	Device	T_{max} [°C]	T_m [°C]	T_{min} [°C]	$ \Delta T_m $ [°C]	F_{max} [°C]
1	Sensor	21.7	21.4	21.1		
Fig. 4.1a	<i>Optris</i>	22.8	22.4	21.9	1.0	0.290
	<i>FLIR</i>	18.3	17.7	17.1	3.7	1.19
2	Sensor	-0.299	-0.647	-0.819		
Fig. 4.1b	<i>Optris</i>	-0.470	-0.800	-1.17	0.153	0.270
	<i>FLIR</i>	-10.7	-11.7	-13.5	11.1	1.50
3	Sensor	18.9	18.7	18.4		
Fig. 4.2b	<i>Optris</i>	19.6	19.3	19.1	0.6	0.180
	<i>FLIR</i>	15.8	15.0	14.4	3.7	1.00

4.1.2 The new conversion factor c_f

The results so far show that c_f is hardly a constant. It is legitimate to think that the ambient temperature also affects the measurement difference between the two cameras. That is why the results from the three mentioned lab experiments were used to deduce an expression for the conversion factor c_f given the pixel values of the *FLIR* camera. Using Eq. 25 together with temperature measurements of *Optris* as reference points and pixel values p_v of *FLIR*, conversion factor c_f was calculated for every measurement point. Conversion factor c_f calculated in such way is shown in Fig. 4.3 as the function of the pixel values p_v for *FLIR* with $R^2 = 0.996$. The labels next to the cloud of measurement points indicate the objects, plate (P), hot cup (HC), cold cup (CC), from Experiments 1, 2 and 3. All the measurement points were fitted by the curve of a fifth degree polynomial given by

$$c_f = -8.476 \cdot 10^{-19} \cdot p_v^5 + 3.295 \cdot 10^{-14} \cdot p_v^4 - 5.114 \cdot 10^{-10} \cdot p_v^3 + 3.960 \cdot 10^{-6} \cdot p_v^2 - 0.015 \cdot p_v + 23.7. \quad (31)$$

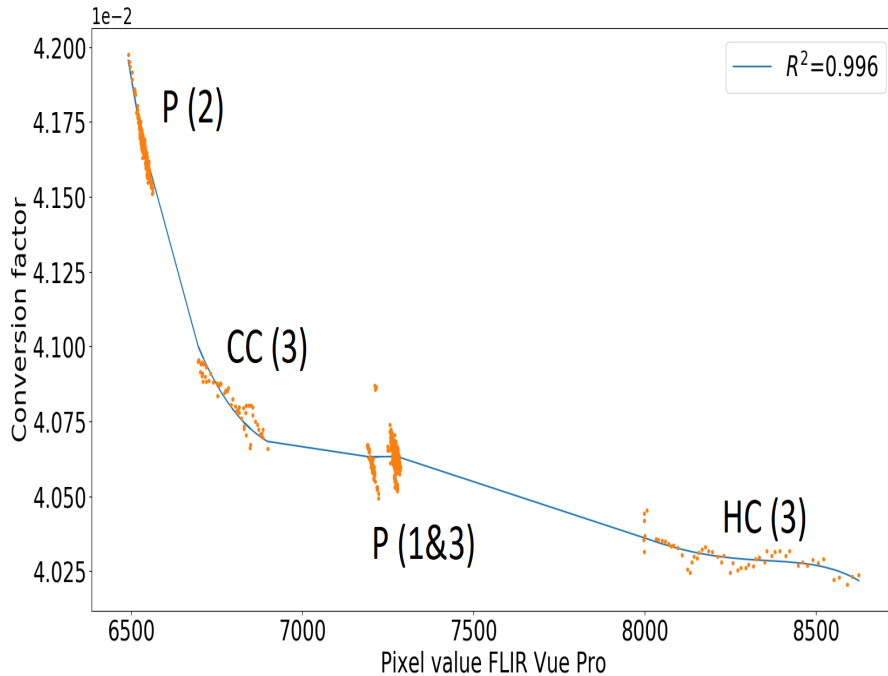


Figure 4.3: The conversion factor c_f described as a function of pixel values p_v of the FLIR camera.

The residual plot of the polynomial regression is shown in Fig. 4.4. Fig. 4.5 shows the temperature difference between the reference temperature, in this case *Optris*, and the fitted values of *FLIR* as a function of the *FLIR* pixel values. The same labels are used in these two figures as in Fig. 4.3 to indicate which object and which experiment is represented by which cloud of points.

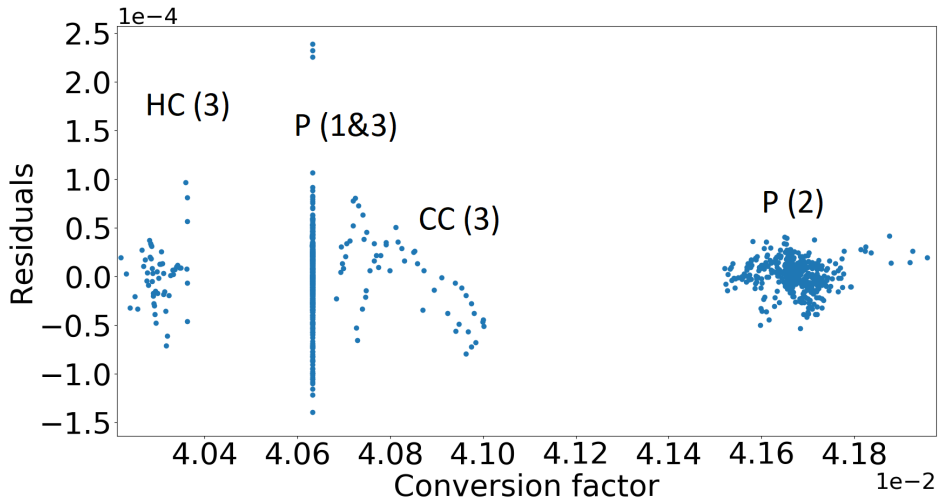


Figure 4.4: Residual plot for the data points shown in Fig. 4.3.

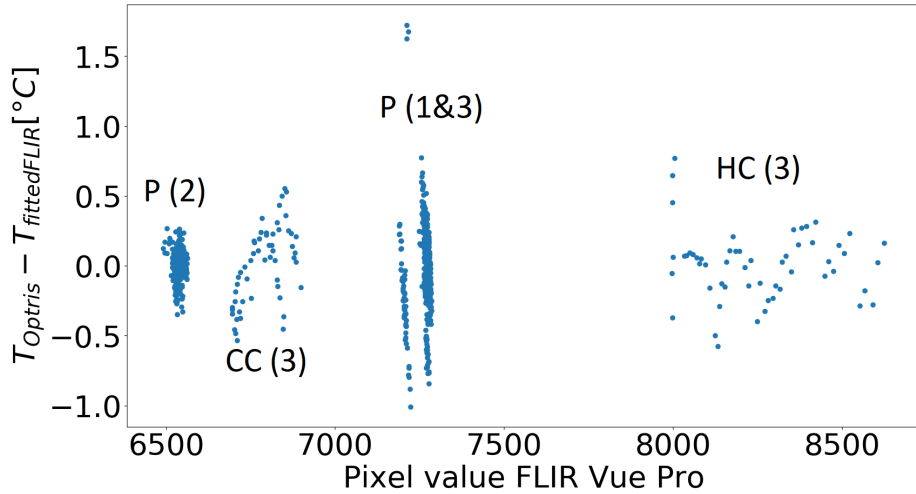
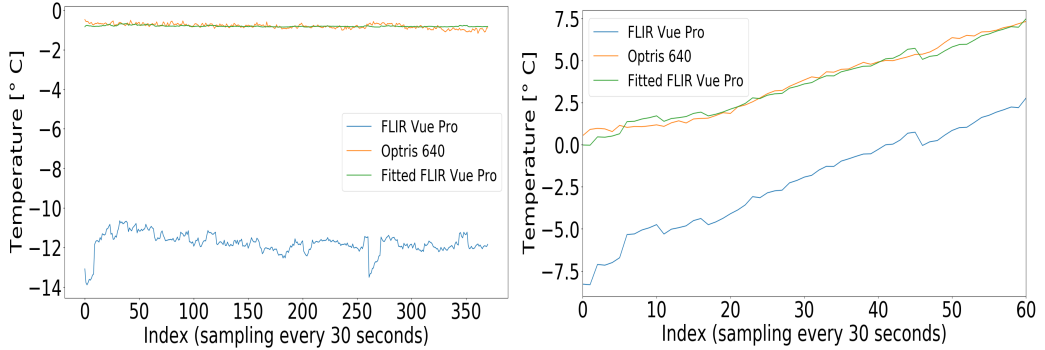


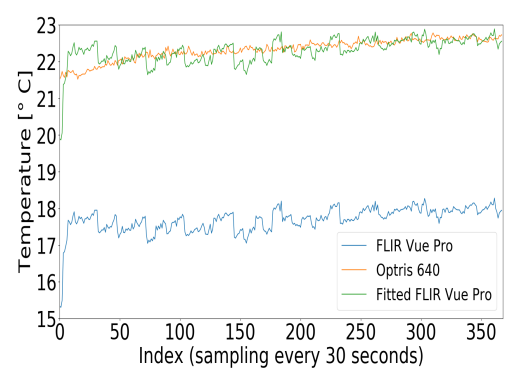
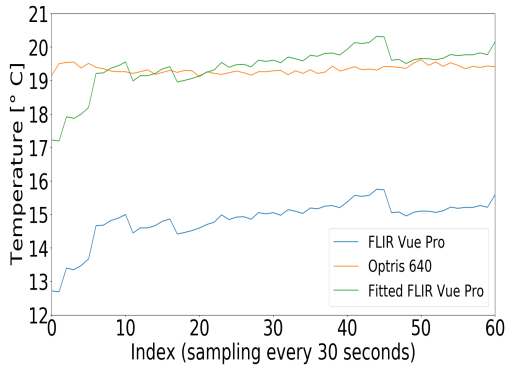
Figure 4.5: Difference between temperature measured by Optris and FLIR after fitting with the fifth degree polynomial.

Fig. 4.6 shows plots of temperature measurements with both cameras of every object from every experiment before and after fitting of *FLIR* measurements. The green line indicates the *FLIR* temperature after it was fitted with the fifth degree polynomial. Otherwise the data in the plots is the same for *Optris* and *FLIR* before fitting as presented in Fig. 4.1a, 4.1b, 4.2a, 4.2b, 4.2c.



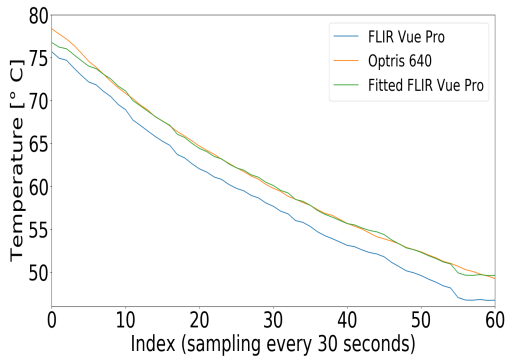
(a) *P (2): Black plate, Experiment 2*

(b) *CC (3): Cold cup, Experiment 3*



(c) *P (3): Black plate, Experiment 3*

(d) *P (1): Black plate, Experiment 1*



(e) *HC (3): Hot cup, Experiment 3*

Figure 4.6: FLIR temperature obtained by the conversion factor $c_f = 0.04$ given by the producer (blue line), Optris temperature (orange line) and FLIR temperature after fitting with the conversion factor c_f given by the fifth degree polynomial (green line).

4.2 Emissivity correction and material classification with NDVI threshold, PCA, k-means and MLC

The result showing the score image of the first principal component performed on the stack of nine IR maps is displayed in Fig. 4.7. Only the first principal component is displayed here because this is where the relevant variation in temperature in different materials is visible. The image is also displayed with the same labels for the different materials shown in Fig. 3.1. Considering the fact that "PCA is often used to bring out strong patterns in dataset" [37], Fig. 4.7 "reveals the dominant patterns of the surface temperature variations during the day" [37]. Different colors indicate that few patterns with surface temperature variations have been detected: vegetation in green, asphalt (1, 2b and 3) in yellow, asphalt (2a) and concrete (5) in light orange and marble (4) in dark orange.

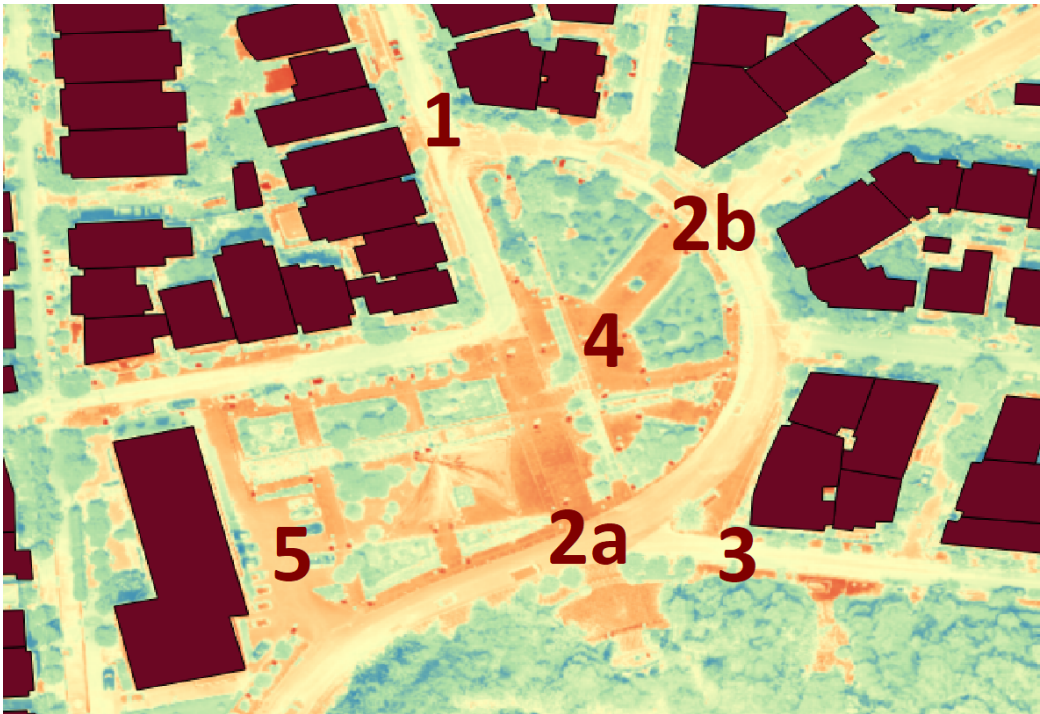


Figure 4.7: Score image of the first principal component of a PCA performed on the stack of nine IR images from June 2017.

The NDVI map used for obtaining the emissivity map is displayed in Fig. 4.8. As it can be observed, the difference between NDVI values for asphalt,

marble and concrete are very small having values between 0.1 and 0.2. The biggest difference on the map is visible for vegetation having values of above 0.4 as opposed to the impervious materials. Due to the fact that it is difficult to differentiate between impervious materials based on the small range of NDVI values from 0.1-0.2, an emissivity map was obtained with two classes as illustrated in Fig. 4.9, one for vegetation and one for impervious materials. The yellow color has the value 0.97 and the purple color the value 0.95. This map was used with Eq. 16 in order to obtain the correct kinetic temperature of the IR images.

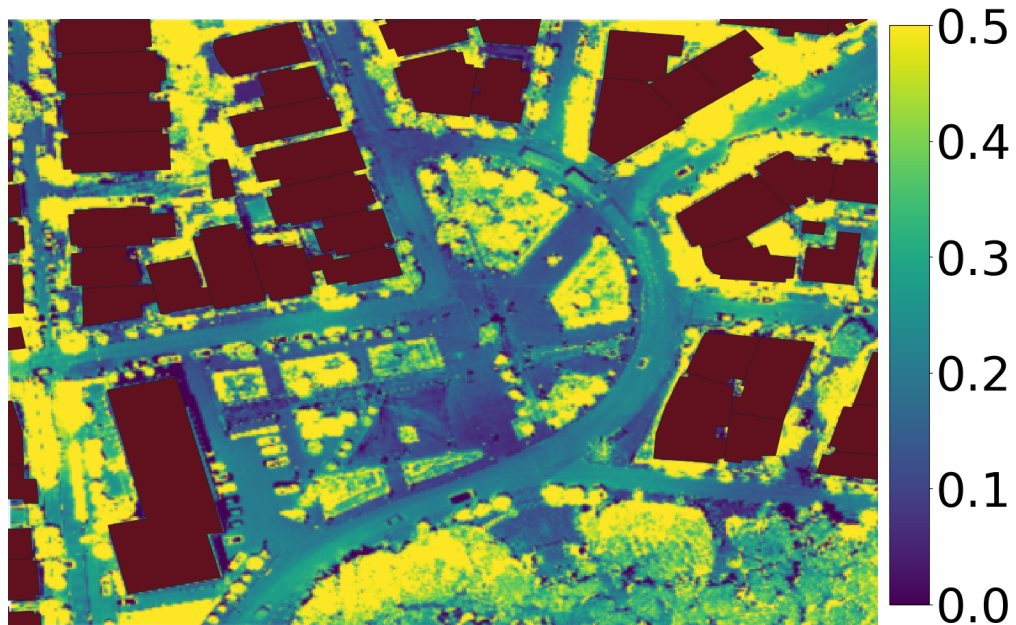


Figure 4.8: Map of the NDVI values.

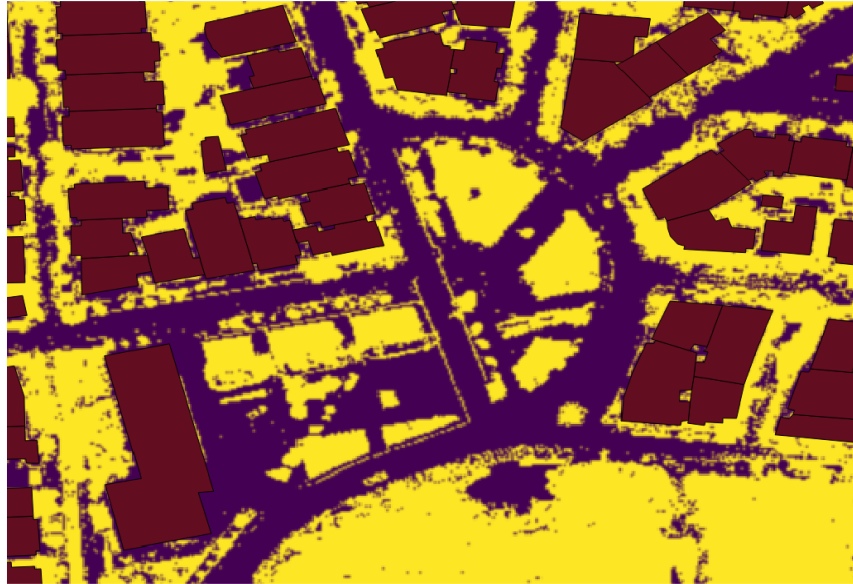
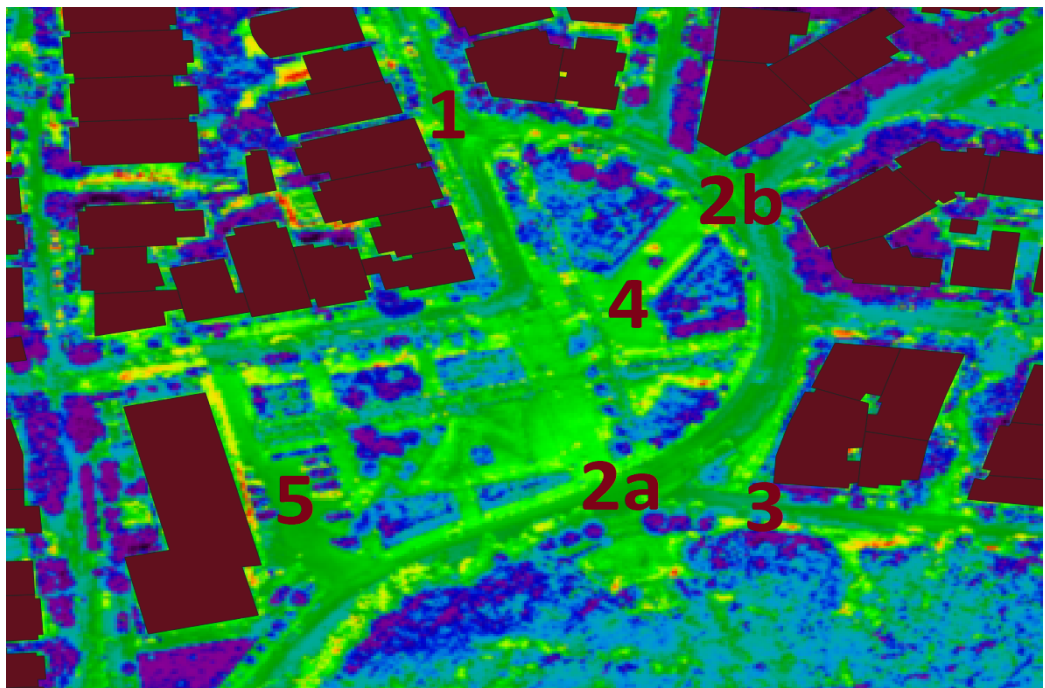
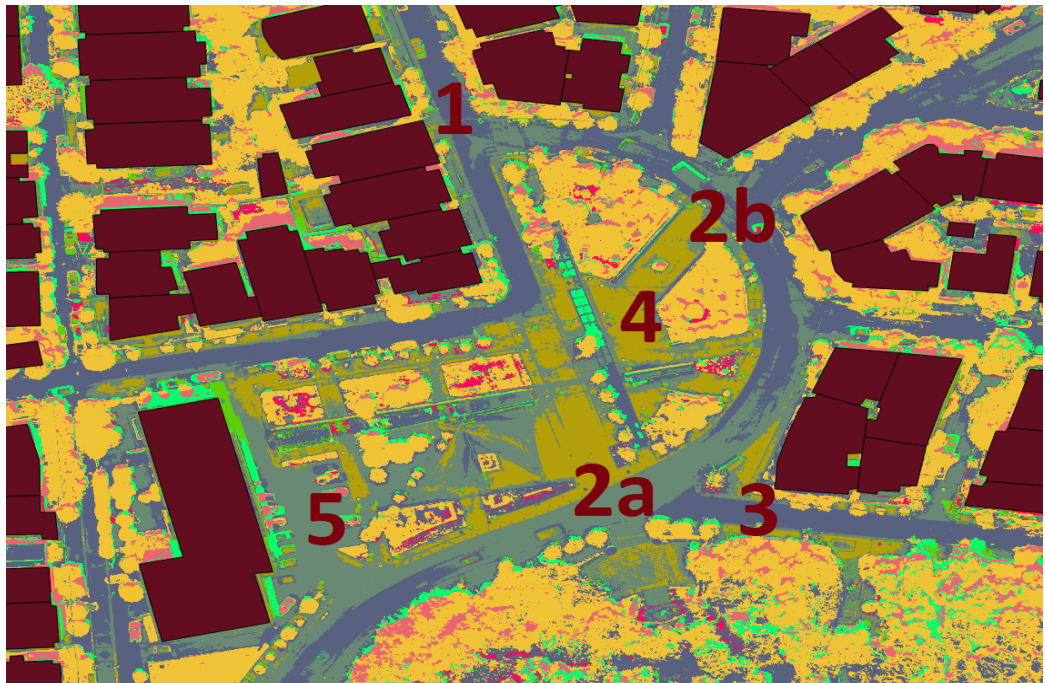


Figure 4.9: Map of two emissivity values: 0.95 (purple) for impervious materials and 0.97 (yellow) for vegetation.

The PCA, k-means and MLC were performed on the reflectance stack containing blue, green, red, NIR and NDVI bands, as flowchart in Fig. 3.5 indicates. These statistical methods generated three maps displayed in Fig. 4.10 and 4.11. The labels indicating the types of materials from Fig. 3.1 are shown on these images as well. Fig. 4.10 shows the results of PCA and k-means. Fig. 4.10a shows the score image of the first principal component, while Fig. 4.10b shows the result of k-means classification in which the data was grouped in eight classes. Color differences on both images make it possible to identify vegetation, marble and asphalt. In Fig. 4.10a there is no difference between the three different types of asphalt and concrete. However, image 4.10b differentiates between two types of asphalt, new conventional and asphalt with cool coating on the one hand, and the old conventional asphalt and concrete on the other hand.



(a) The score image of the first principal component.



(b) K-means clustering with eight clusters.

Figure 4.10: Results of PCA and k-means clustering performed on a stack of five bands: blue, green, red, NIR and NDVI.

Fig. 4.11 shows the result of an attempt of supervised classification with MLC with ten classes. Also here it is possible to identify marble, vegetation, asphalt and some more classes as opposed to the two preceding methods such as soil (black), water (dark blue) and tiles for the blind (turquoise). As opposed to the unsupervised classification, MLC seems to identify three types of asphalt, but not correctly compared to Fig. 3.1.

An overview of the color patterns is shown in Table 4.2 which summarizes the colors indicating asphalt, marble, concrete and vegetation visible in Fig. 4.7, 4.8, 4.10a, 4.10b and 4.11.

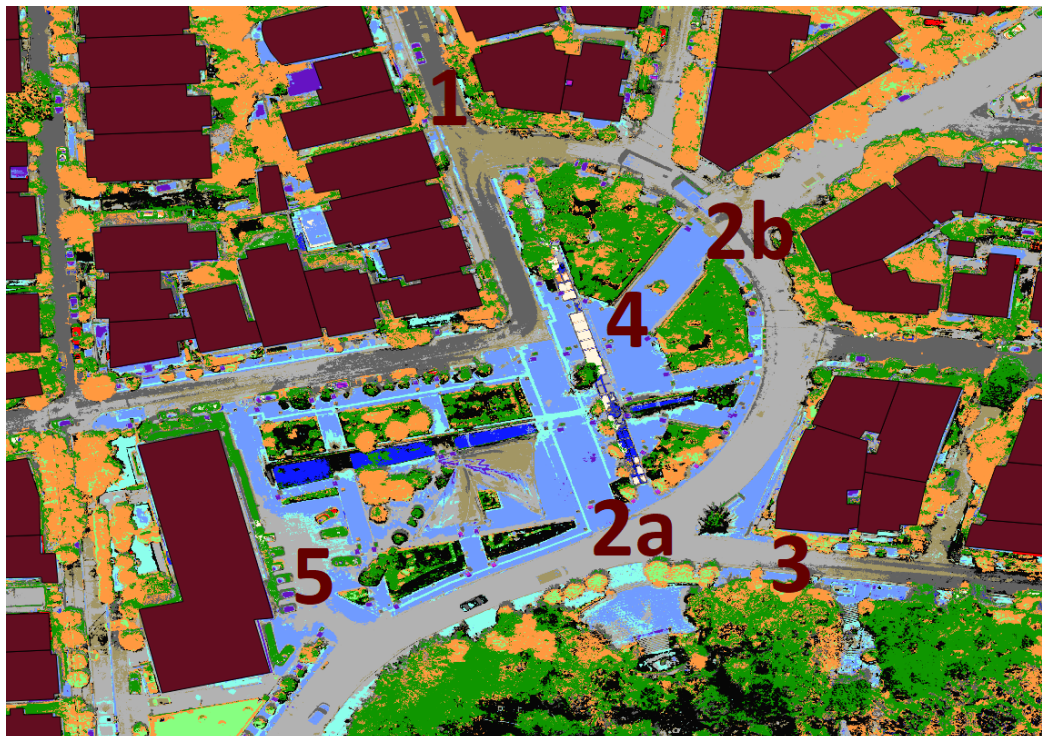


Figure 4.11: MLC with classes old asphalt(grey), asphalt with cool coating (brown), new conventional asphalt (dark grey), marble (blue), tiles for the blind (turquoise), dark blue (water), trees type 1 (green), trees type 2 (orange), grass (light green), soil (black).

Table 4.2: Color patterns for the five groups of materials in the study area: 1) asphalt with cool coating, 2a), 2b) old conventional asphalt, 3) new conventional asphalt, 4) marble, 5) concrete and vegetation

Material	NDVI	PCA IR	PCA reflectance	k-means	MLC
1	[■ ■]	[■]	[■]	[■]	[■ ■ ■]
3	[■ ■]	[■]	[■]	[■]	[■ ■ ■]
2a	[■ ■]	[■]	[■]	[■]	[■]
2b	[■ ■]	[■]	[■]	[■]	[■]
5	[■ ■]	[■]	[■]	[■]	[■ ■ ■]
4	[■]	[■]	[■]	[■]	[■]
Vegetation	[■]	[■]	[■]	[■]	[■ ■ ■]

4.3 The maximum surface temperature T_{smax}

This section presents the results of three different methods for predicting surface temperature T_s . First of all, results based on ATI will be described in Section 4.3.2. Secondly, linear regression based on Eq. 19 is used to predict the maximum surface temperature and to assess it with respect to TI and albedo. This will be presented in Section 4.3.3. Finally, Section 4.3.4 presents the results with respect to parametrization of the maximum surface temperature. Since analyzing these methods is based on weather conditions and irradiation, this section will start with presenting the results of air temperature, relative humidity and irradiation measurements for 12 April 2016 and 19-21 June 2017 in Section 4.3.1.

4.3.1 Weather conditions and solar irradiation

Incoming direct solar irradiation obtained from a weather station in Athens with hourly resolution for all four days is shown in Fig. 4.12. The plot shows clearly that the highest values were measured on 20 June 2017 (green line) and lowest on 12 April 2016 (blue line).

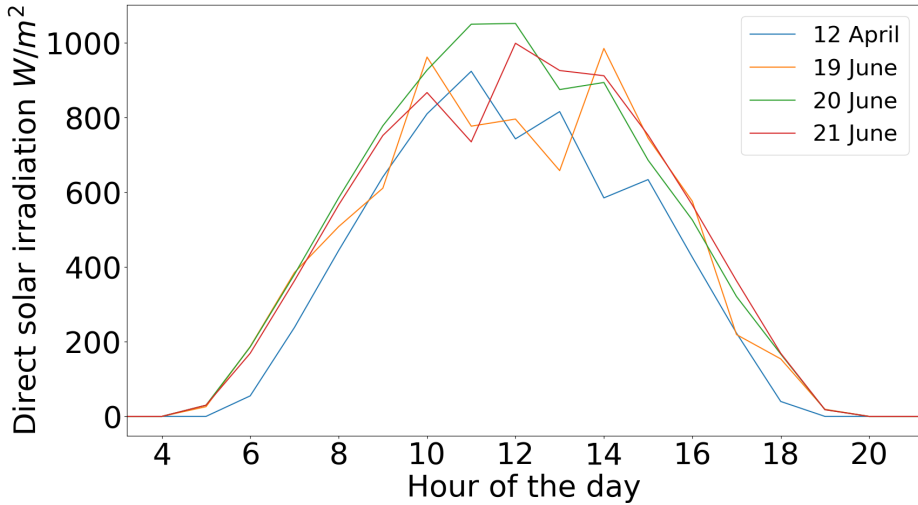


Figure 4.12: Incoming direct solar irradiation on 12 April and 19-20 June.

The procedure of creating irradiation maps based on the values displayed in Fig. 4.12 was described in Section 3.2.2.4. Fig. 4.13 shows the accumulated direct and diffuse irradiation [Wh/m^2] over the study area until 01:00 pm for 12 April and 19-21 June in Fig. 4.13a and Fig. 4.13b-4.13d respectively. The maps reflect the amount of accumulated irradiation for every day. The map for 20 June is the lightest due to highest values of accumulated irradiation and the one for 12 April is the darkest due to lowest values. The error in measurements of direct irradiation from the weather station is not known. The model used to predict diffuse irradiation per hour has an error of 10% [54]. Considering error propagation, this is not a considerable value because the highest values of diffuse irradiation predicated by [54] are approximately $100 W/m^2$. The error in Fig. 4.13 due to diffuse irradiation is thus around 1.0 %.

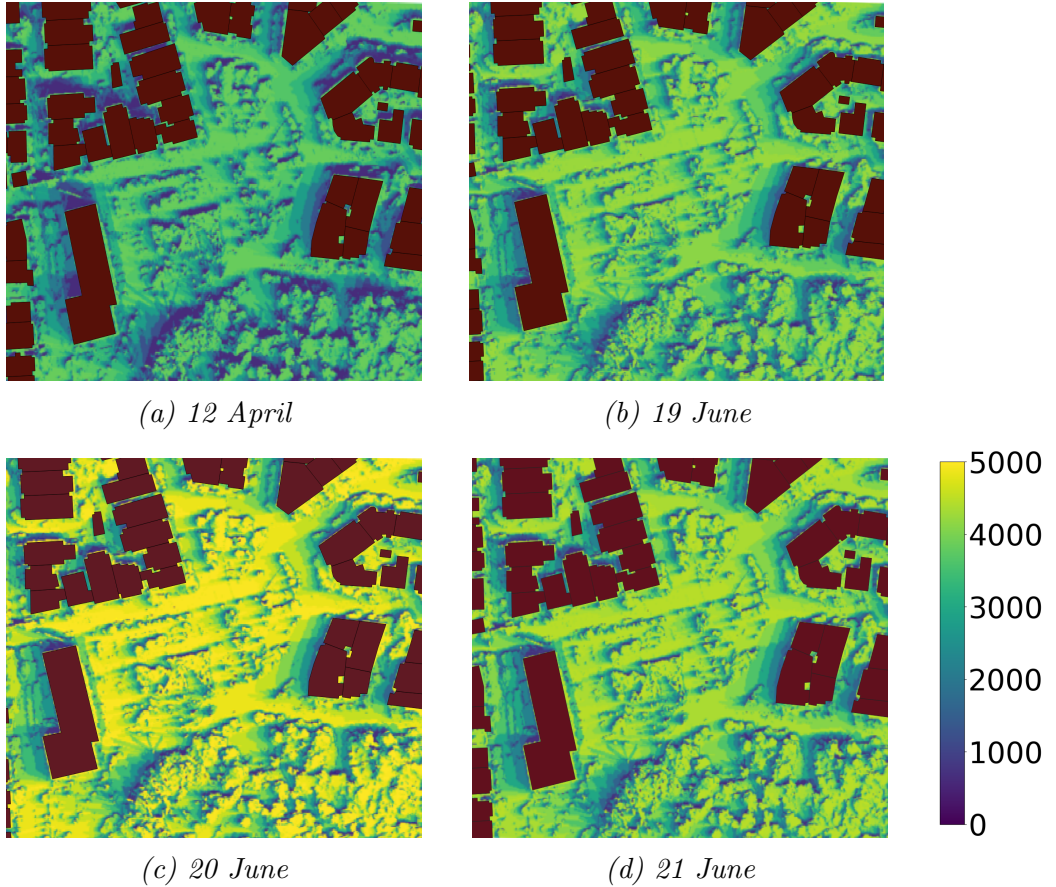


Figure 4.13: Accumulated incoming direct and diffuse irradiation [Wh/m^2] over the study area.

Air temperature [°C] and humidity [%] are shown in Fig. 4.14 for the three days particularly relevant for the later analysis, 12 April, 19 June and 20 June. The plots are made based on the measurements conducted in the study area. The systematic error in the measurements is 3.0% for the humidity and 0.5°C for the air temperature [59] as indicated in the plots. They show that the highest temperature was measured on 20 June and the lowest on 12 April. Humidity was relatively low on all three days.

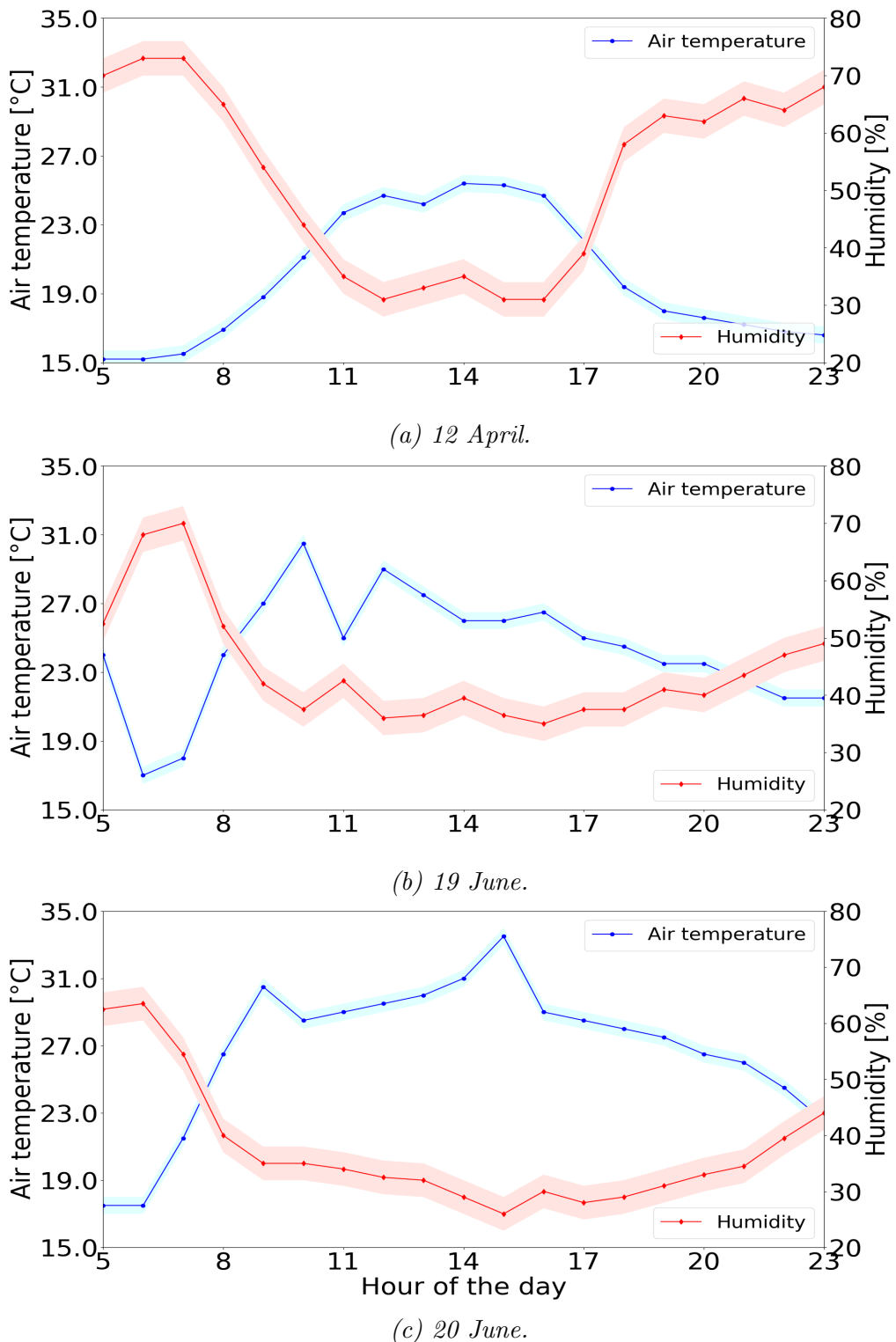
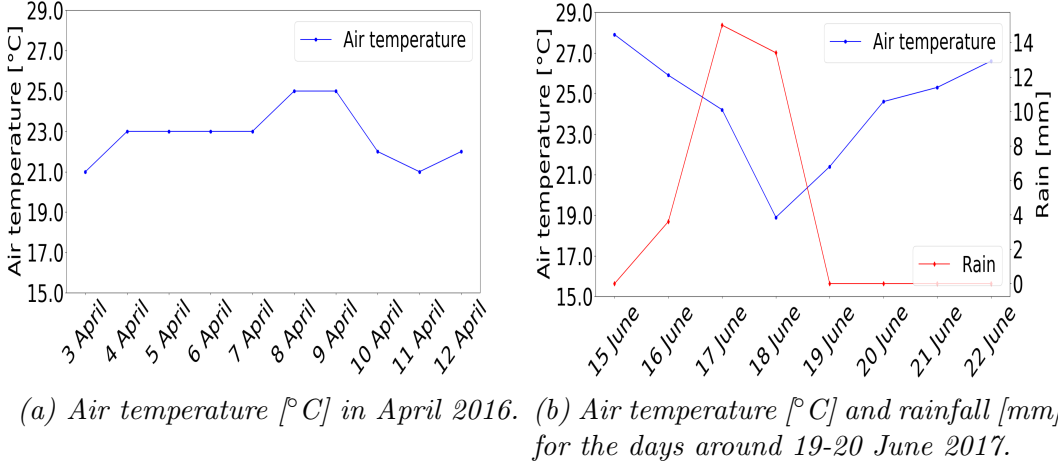


Figure 4.14: Air temperature and relative humidity for 12 April 2016, 19 June 2017 and 20 June 2017.

Furthermore, the maximum air temperature [$^{\circ}\text{C}$] and rainfall [mm] in April 2016 and June 2017 prior to days when data collection was conducted are shown in Fig. 4.15. According to data displayed in Fig. 4.15a [58], the air temperature was above 20°C in Athens for several days prior to 12 April, more precisely as of 3 April 2016. There was no rain in Athens prior to 12 April as the figure indicates. Image 4.15b shows weather conditions, maximum air temperature [$^{\circ}\text{C}$] and rain fall [mm], in the middle of June 2017 for the days around 19-21 June when the measurements were conducted. The data was obtained from a weather station and so the error in the measurements is not known.



(a) Air temperature [$^{\circ}\text{C}$] in April 2016. (b) Air temperature [$^{\circ}\text{C}$] and rainfall [mm] for the days around 19-20 June 2017.

Figure 4.15: Weather data for April 2016 and middle of June 2017 showing air temperature, rainfall and humidity.

4.3.2 Temperature, albedo and ATI maps

Maps of surface temperature from April 2016 are shown in Fig. 4.16 for the temperature range [10, 55] $^{\circ}\text{C}$. Image 4.16a shows a temperature map from the early morning of 12 April, while 4.16b displays temperature around 12:30 pm on the same day. The uncertainty in the two maps is $\pm 2^{\circ}\text{C}$. After the conversion of pixel values with the factor c_f from Section 4.1 and emissivity correction described in Section 4.2, temperature maps from 2017 were obtained as illustrated in Fig. 4.17. Every row in Fig. 4.17 contains maps from one of the three days, 19 June, 20 June and 21 June. Every flying session, morning (05:30 am and 10:30 am), midday (01:30 pm), afternoon (05:00 pm) and evening (09:30 pm and 10:30 pm) are displayed column-wise.

The uncertainty in the maps will be assessed as a result of evaluation of the *Optris* and *FLIR* cameras.

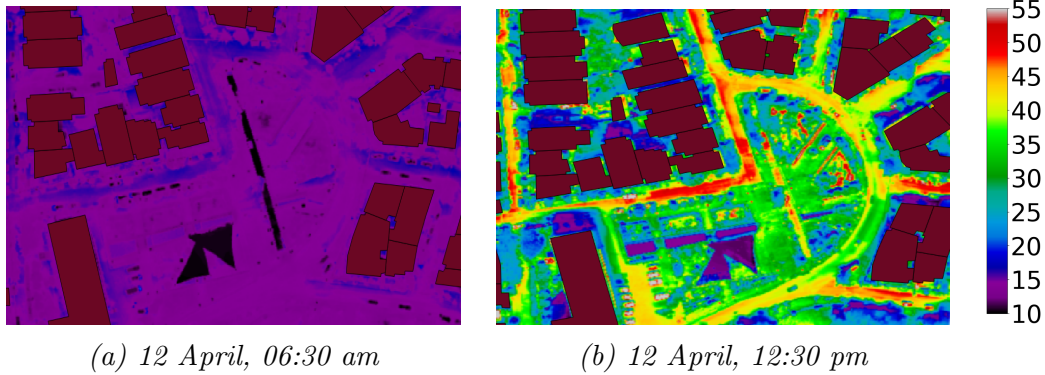


Figure 4.16: Temperature maps [°C] from 12 April 2016.

The maps in Fig. 4.16 and 4.17 from the middle of the day show that the asphalt with cool coating and the new conventional asphalt, labelled 1 and 3 in Fig. 3.1, have the highest temperature. Temperature of old conventional asphalt and concrete, labelled 2a, 2b and 5, appear to be lower, while marble, labelled 4, has the lowest temperature of the impervious materials. In all the images in Fig. 4.16 and 4.17 it is visible that vegetation has considerably lower temperature than the impervious materials. It should also be noted that Fig. 4.17d shows higher temperature than Fig. 4.17c.

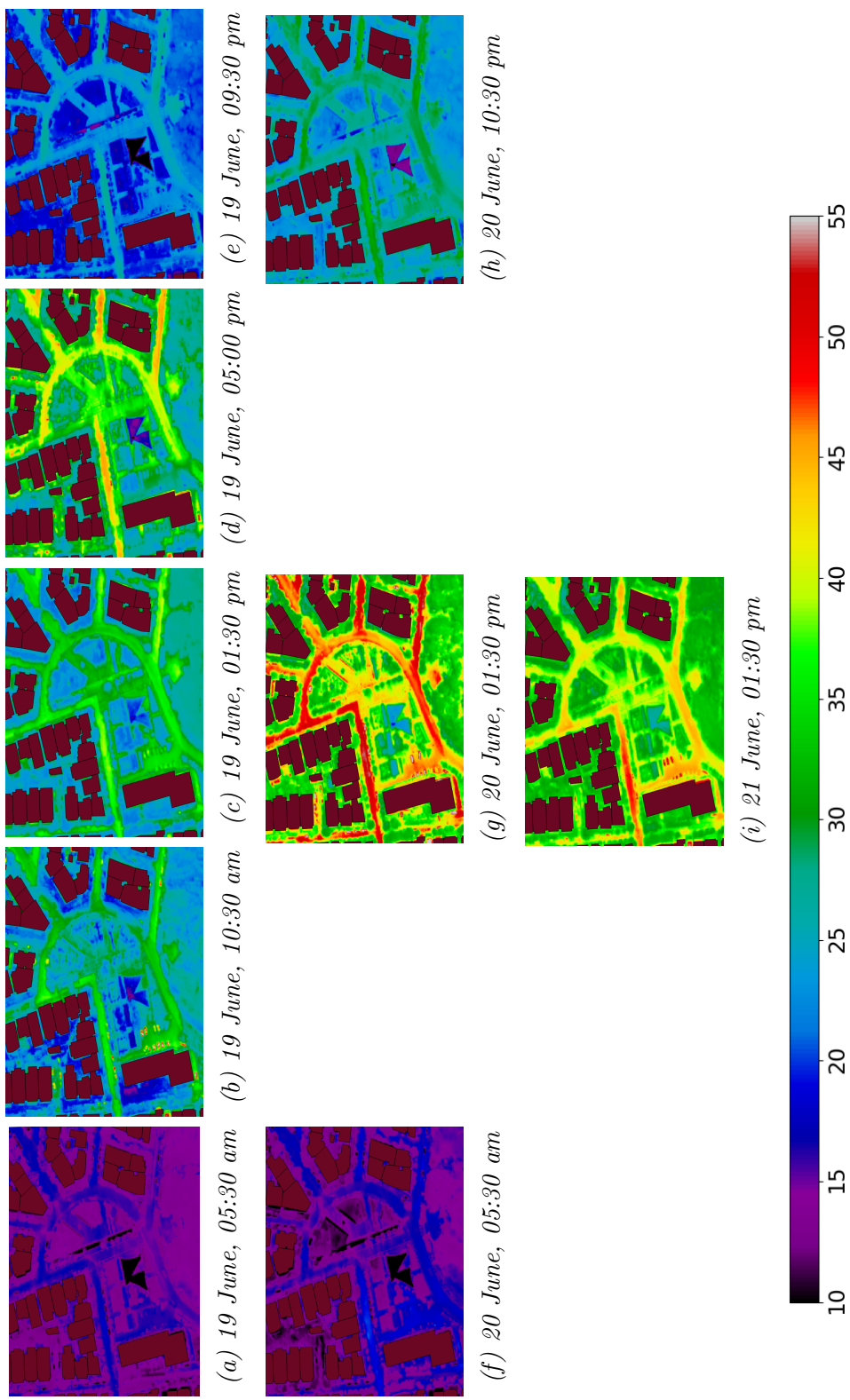


Figure 4.17: Temperature maps ${}^{\circ}\text{C}$ from June 2017.

With the temperature maps for each day as shown above, it was possible to obtain three maps for 12 April, 19 June and 20 June showing the difference between the maximum measured and minimum measured temperature ΔT (Appendix A). These are displayed in Fig. 4.18a, 4.18b and 4.18c respectively for the temperature range [10, 40] °C. The uncertainty in the map 4.18a is +/-4.0°C, while the uncertainty in maps 4.18b and 4.18c will be assessed as a result of evaluation of the *Optris* and *FLIR* cameras. All three maps show similar patterns in the distribution of ΔT according to the material-wise distribution of the surface temperature T_s described with respect to Fig. 4.16 and 4.17.

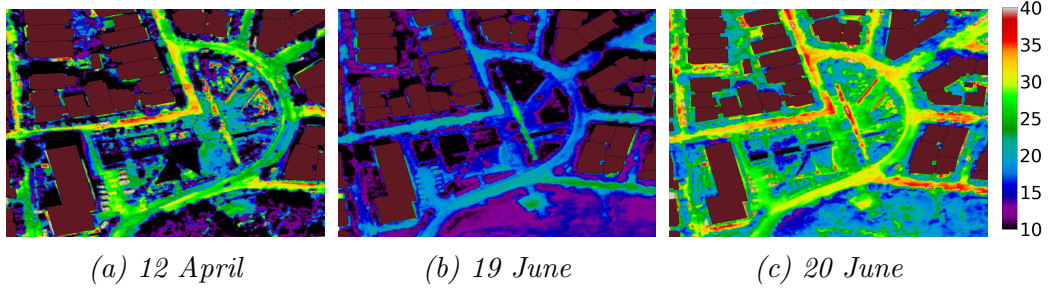


Figure 4.18: Maps illustrating the diurnal temperature difference e.g. the difference in maximum and minimum measured temperature ΔT [°C] on 12 April, 19 June and 20 June.

According to Eq. 20, it is necessary to firstly obtain albedo values α in order to obtain the ATI maps. Fig. 4.19 shows two albedo maps. The map displayed in 4.19a was obtained from RGB and NIR images taken in April 2016 and 4.19b was obtained from images taken in June 2017 (Appendix A). Both of them show a range of albedo values from 0.00 to 0.40. The uncertainty in the albedo values calculated according to Eq. 27 is determined with respect to ground measurements [46]. However, necessary ground data measurements lack from both 2016 and 2017. The error introduced will be dependent on the camera [37].

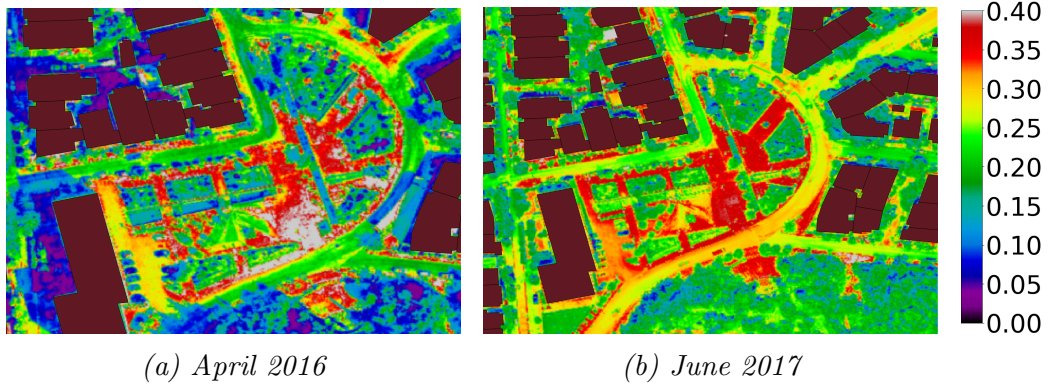


Figure 4.19: Albedo maps obtained with blue, green, red and NIR channels according to Eq. 27.

Based on the images in Fig. 4.18 and 4.19 as well as Eq. 20, ATI maps for the three days, 12 April, 19 June and 20 June, could be obtained (Appendix A). Using the normalized images from Fig. 4.13, the ATI maps [K^{-1}] could be scaled with respect to solar irradiation. Thus they were corrected for irradiation effects and shadows as displayed in Fig. 4.20. In this way the variation between maps in Fig. 4.20 can be interpreted due to other effects than differences in irradiation due to shadows. The uncertainty in the ATI maps and a more detailed analysis will be given in the next chapter.

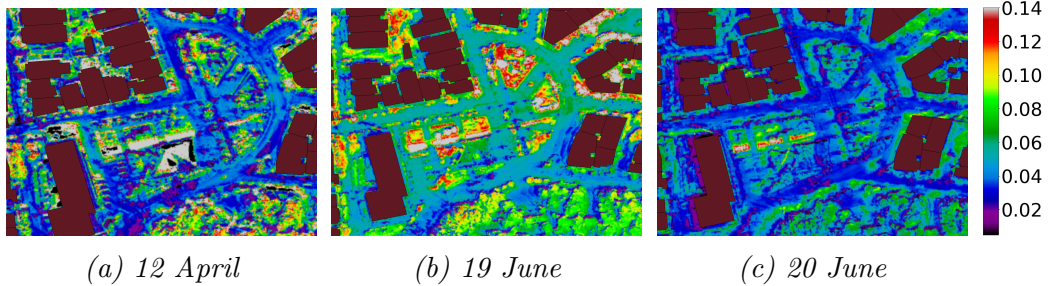


Figure 4.20: Normalised ATI maps [K^{-1}] with respect to solar irradiation.

4.3.3 The model based on thermal inertia (TI)

An attempt has been made in Fig. 4.21 to illustrate the development of surface temperature of asphalt (green line), marble (orange line) and concrete (blue line) over the period of three days in June. Every of the nine points on Fig. 4.21 is the average temperature value for that particular material from a spot where the material received the most irradiation and where there was as little shadow as possible. It is visible that asphalt and concrete have the highest temperature followed by marble. The black line indicates the incoming solar irradiation [W/m^2] as shown also in Fig. 4.12 with one hour resolution during those three days.

There are several interesting aspects about Fig. 4.21. It is visible on the blue line that the attempt of finding concrete without shadow until 05:00 pm on 19 June was not entirely successful as was anticipated during data processing. From the temperature development on 19 June it is also visible that the temperature measured at 01:30 pm is not the maximum daily temperature of the materials. The temperature of sunlit areas probably peaks somewhere between 01:00 pm and 05:00 pm. The figure also shows that the maximum temperature is lagging behind the daily maximum solar irradiation.

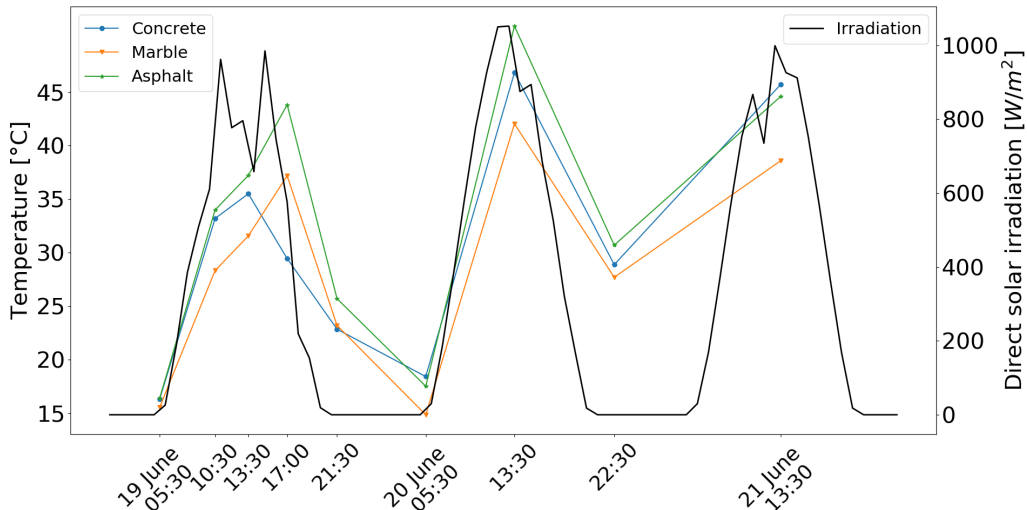


Figure 4.21: Development of surface temperature for asphalt, concrete and marble from 19 June till 21 June.

It is visible from Fig. 4.21 that the highest surface temperature T_{smax} , which is possible to obtain, comes from the measurements from midday. It is dis-

played in Fig. 4.22 as a function of absorptivity according to Eq. 19. Fig. 4.22 illustrates the linear regression curves for the three materials where the maximum surface temperature T_{smax} is shown as the function of the absorbed solar irradiation, $(1 - \alpha)I_0$, for $\gamma = 1$. The slope of the curves thus represents the term $\frac{1}{P\sqrt{\omega}} [K/W/m^2]$. Linear regression for $\gamma = 1$ means that the value of thermal inertia P is given for the case when all the incoming radiation that is absorbed by the material is not conducted through it.

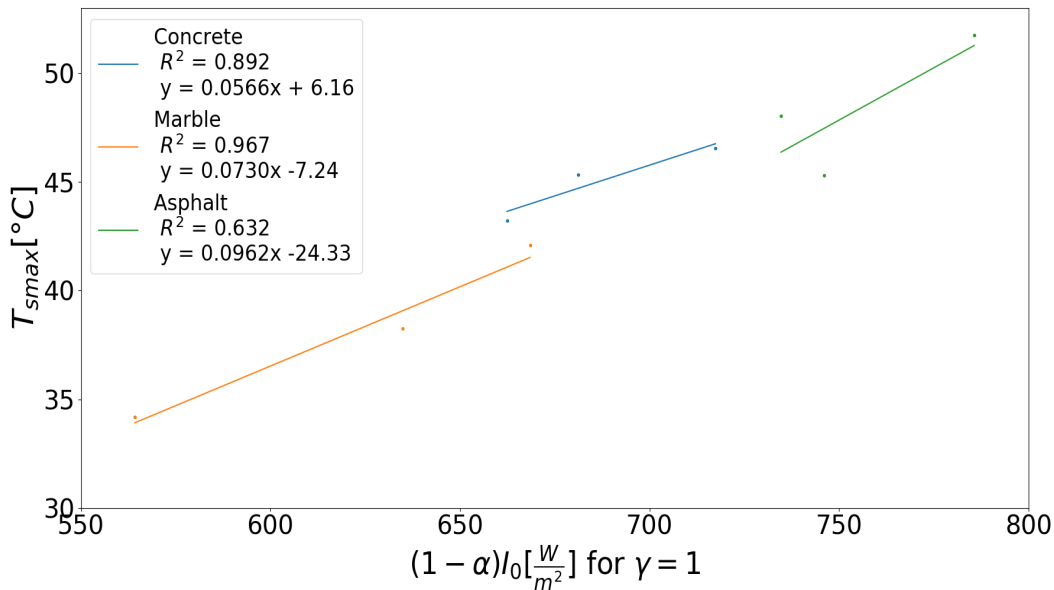


Figure 4.22: Linear regression of T_{smax} as a function of albedo and the peak of incoming solar irradiation for $\gamma = 1$.

Using the slope of the curves, the values of thermal inertia P are calculated and listed in Table 4.3 for asphalt, marble and concrete.

Table 4.3: Overview of the thermal inertia P values obtained from the slope ($\frac{1}{P\sqrt{\omega}}$) of the linear regression curves in Fig. 4.22.

Material	$P [J m^{-2} K^{-1} s^{-1/2}]$
Asphalt	1 219
Marble	1 606
Concrete	2 072

4.3.4 Parametrization of the maximum surface temperature T_{smax}

According to the method described in Section 3.2.2.6, sinusoidal curves could be obtained for asphalt, concrete and marble. They are shown in the following figure, Fig. 4.23. The green curve in Fig. 4.23a is based on parametrization by Lindberg et al [57]. The orange curves are based on the trial and error method described in Section 3.2.2.6. The value of η was varied while b was kept constant until the sinusoidal curves were fitted as well as possible to the three measurement points from 20 June. The values for η and b were then used to obtain the parametrization equation written on every of the three figures in Fig. 4.23. The values of η obtained for asphalt, concrete and marble are 0.37, 0.31 and 0.24 respectively.

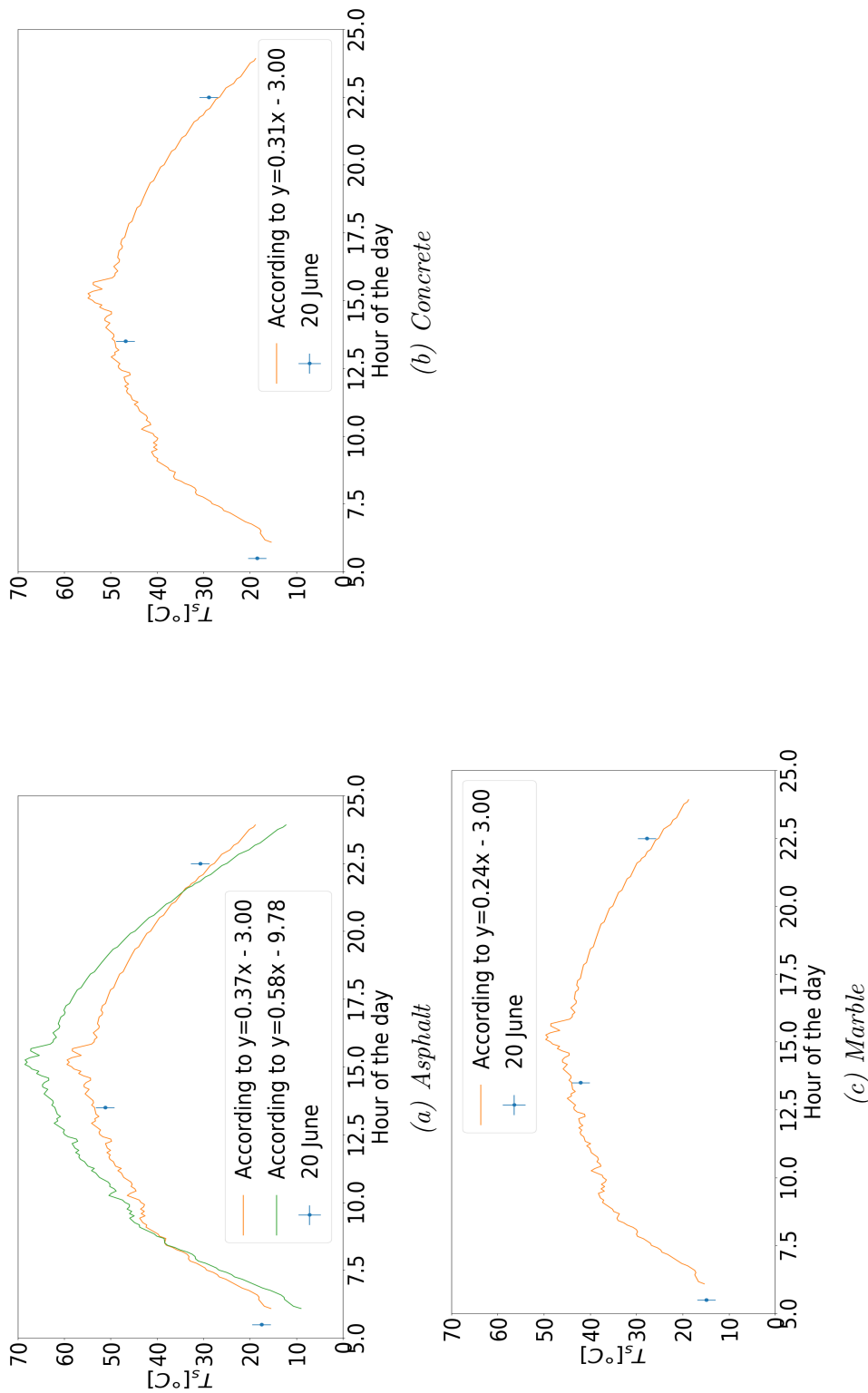


Figure 4.23: Sinusoidal curves obtained according to parametrization as described in Section 3.2.2.6.

5. Discussion

This chapter presents an analysis of the results as displayed in Chapter 4. To begin with, Section 5.1 will focus on the analysis of the laboratory results. Section 5.2 assesses the different classification methods of materials from the study area. The attention is turned towards the subject of surface temperature and more concretely, ATI, linear regression of Eq. 19 and parametrization of the surface temperature in Section 5.3.

5.1 Laboratory experiments on *FLIR Vue Pro* and *Opbris 640*

Current section analysis results presented in Section 4.1. Section 5.1.1 assesses both cameras based on the results from the laboratory experiments. Section 5.1.2 elaborates on the meaning of the new conversion factor c_f for the processing of the images collected in June 2017.

5.1.1 Comparison between *FLIR Vue Pro* and *Opbris 640*

Looking at Fig. 4.1a and 4.1b, it is possible to detect two obvious differences between the *FLIR* and *Opbris* cameras: the difference between their mean measured temperatures T_m and the reference temperature and the difference between the sudden change in temperature measured by each camera (fluctuations). The deviations of the mean temperatures T_m from the reference temperature as well as the fluctuations are also visible in Fig. 4.2b. The fluctuations between the maximum and the minimum temperatures of each cameras are, however, not that pronounced in Fig. 4.2a and 4.2c. An explanation for that could be the rapid change in temperature of the cold and hot objects compensating for the fluctuations in measurements, which are visible when the object has a constant temperature (black plate). This is why only Fig. 4.1a, 4.1b and 4.2b were chosen for this part of the analysis.

It is visible from Table 4.1 that the mean temperature T_m in Fig. 4.1a measured by *Opbris* deviated by 1.0°C from the reference temperature, while the mean temperature of *FLIR* deviated by 3.7°C . In Fig. 4.1b, the deviation in mean temperature is 0.153°C for *Opbris* and 11.1°C for *FLIR*. Lastly, in Fig. 4.2b, the differences between the mean temperature of the two cameras with respect to sensor's temperature are 0.6°C for *Opbris* and 3.7°C for *FLIR*. The deviations for *FLIR* in Fig. 4.1a and 4.2b fall within the uncertainty of $+/- 5^\circ\text{C}$, but the deviation in Fig. 4.1b is more than two times as big as the uncertainty given by the producer.

These findings are in accordance with the findings by Opbris GmbH. They conducted tests on the two cameras by measuring the temperature of solar panels with the cameras attached to a drone. The temperature of the panels was 18.0°C . Several measurement points were registered. *Opbris* camera was more accurate. The deviations between the reference temperature and the temperature measured by *FLIR* was between $1.5\text{-}3.2^\circ\text{C}$. The deviations between *Opbris* and the reference temperature were $0.8\text{-}1.1^\circ\text{C}$. *FLIR* measurements were below the reference temperature (Opbris GmbH, private communication) as is the case with measurements conducted in the laboratory experiments described here.

Looking at the last column in Table 4.1, the differences between the two cameras are again substantial. Temperature measured by *Opbris* fluctuated at the most 0.29°C , while fluctuations recorded by *FLIR* are between 1.00°C and 1.50°C . Considering the FFC elaborated in Section 3.2.1, the temperature-wise fluctuations are higher than the FFC which is 0.5°C according to the settings.

The analysis so far has shown that *FLIR* measurements deviate from the reference temperature. These deviations do not fall within its systematic error e.g. they are greater than $+/- 5^\circ\text{C}$. The deviations are dependent on the temperature of the object. As opposed to *FLIR*, *Opbris* is considerably reliable when compared to sensor's reference temperature. Its deviations from the reference temperature are 1.0°C or less. The fluctuations in the measurements by *Opbris* are also considerably lower. This is why *Opbris* was used as reference temperature in Experiment 3 and in finding the new conversion factor c_f in Fig. 4.3.

5.1.2 Effects of the regressed conversion factor c_f on the data from Athens

It is interesting to see what influence the regressed conversion factor c_f has on the fluctuations and how well it corrects the temperature of each object in the measurement series used here.

Fig. 4.5 illustrates that the temperature difference between the measurements conducted by *Opbris* and fitted *FLIR* values are between -1.00°C and +1.50°C. This is also illustrated in Fig. 4.6. At the same time, Fig. 4.6 captures what has happened with the fluctuations after fitting. It is visible in the figures in the upper row, Fig. 4.6a and 4.6b, that the fluctuations have been straightened up considerably at the same time as the new *FLIR* temperature fits the *Opbris* temperature very well. This is particularly the case for Fig. 4.6a. The fluctuations in the middle row, e.g. in Fig. 4.6c and 4.6d, do not seem to be straightened at all, just moved to the level of the temperature measured by *Opbris*. In the case of the hot object, Fig. 4.6e, there were no fluctuations in the first place and the green line seems to fit nicely with the *Opbris* line displayed in orange.

The reason for these observations can be found in how the points around the line for the fifth degree polynomial are distributed in Fig. 4.3. It is visible in Fig. 4.3 that the points in the upper left corner labelled $P(2)$ are distributed nicely along the line. The line seems to go along the middle value of the points and in that way the curve fitting removes the fluctuations visible in Fig. 4.1b. This is partly the case for the group of dots further down the line marked with $CC(3)$. The cloud of points labelled $P(1&3)$ in the middle of Fig. 4.3 shows, however, that the points are scattered far below and far above the line. The fifth degree polynomial line goes across the cloud of points and gives a constant conversion factor c_f for all the points no matter how far below or above the line they are. With a constant conversion factor, all the *FLIR* measurements are replicated to the same spots with the same fluctuations further up on the y-axis as indicated in Fig. 4.6c and 4.6d. Last but not least, it seems that the line of the fifth degree polynomial is passing through the average of the points labelled $HC(3)$ to the far right.

Another way to see how well the regression fits the data is by looking at the residual plot in Fig. 4.4. The cloud labeled $P(2)$ seems to be randomly scattered around the zero line. The same goes more or less for all the clouds apart from $P(1&3)$. There is a pattern visible in this part of the residual plot which does not capture the variation in the data. The fact that this

is a problematic data cloud for the regression curve coincides well with the observations in Fig. 4.6c and 4.6d, which show that the *FLIR* measurements are poorly fitted.

An evaluation of these observations with respect to the correction of the images collected in Athens in June 2017 is in order. The temperature differences noted by inspection of some of the images of the same objects before they were processed in Pix4D were up to 5.0°C . As mentioned in Section 3.2.2.1, such images were removed before processing in Pix4D since the overlap of the images from June 2017 is 70-80%. However, the method of removing the images by inspection is not very reliable. Based on the analysis of the conversion factor and the possibility that not all images were removed before processing, it is possible that the fluctuations of the *FLIR* measurements have remained in the images covering the same objects. This is the case for the pixel values which give an approximately constant conversion factor c_f , e.g. in the range 7000-7500. It was also noted in Section 3.2.2.1 that Pix4D software weights and averages each pixel value of the original images when creating maps. There is therefore a reason to think that Pix4D straightens these fluctuations to a certain extent. Apart from the fluctuations, *FLIR* temperature seems to have been transformed to the reference temperature with the fifth degree polynomial quite well.

Nevertheless, more measurements in the lab and particularly with the drone, with which the camera would operate under airflow, are necessary. A concrete improvement with the measurements done so far would be to leave the hot object and the cold object to gradually cool down and warm up in order for the measurement points to be more spread out. This would have lead to a better regression and a more accurate conversion factor for *FLIR* pixel values. Also more test data with the known temperature on which the current conversion factor c_f could be tested is necessary.

5.2 Material classification with NDVI threshold, PCA, k-means and MLC

The results in Section 4.2 indicate that NDVI-threshold as well as PCA, k-means and MLC performed on the IR stack and the stack of five channels of reflectance maps show somewhat different potential to identify different materials.

Table 4.2, column 2, shows color distribution from the NDVI image in Fig. 4.8. It is visible that there is no clear difference between the classes of the five impervious materials. They have the same colors or a mixture of two colors. This indicates that the different materials have the same ranges of NDVI-values and that there are different ranges of values mixed in the areas with the same type of material. The only clear difference visible on the NDVI map is between the impervious materials and vegetation.

The color distribution from the score image of the first principal component of the PCA performed on the IR stack, Fig. 4.7, is shown in column 3. Based on temperature variations recorded there, it can be said that the temperature variation of vegetation, marble, asphalt and asphalt/concrete can be identified. The analysis cannot separate the temperature change in concrete from the old conventional asphalt in 2a. The temperature variation in the old conventional asphalt (2a and 2b) is not clearly distinguished since these two spots are marked with two different colors. At the same time, the temperature variation in asphalt with cool coating (1) and new conventional asphalt (3) seem to be the same. Thus, the variation in the asphalt does not entirely correspond to the numbers marked in Fig. 3.1.

The score image of the first principal component of the reflectance stack shown in Fig. 4.10a, summarized in column 4, displays similar results as the NDVI map. Vegetation is clearly visible with blue color and marble with light green. However, there do not seem to be any clear differences between spots marked with numbers 1, 2a, 2b, 3 and 5. Looking at the image 4.10a, one could argue that the color at spots 2a and 5 is somewhat lighter than the color in spots 2b and 3. However, those differences are hard to detect.

On the other hand, color patterns from Fig. 4.10b, summarized in column 5, are similar as in column 3. K-means clustering has managed to differentiate between vegetation, marble, asphalt and asphalt/concrete. K-means has clustered old conventional asphalt (2a) together with concrete (5) as op-

posed to asphalt with cool coating (1), new conventional asphalt (3) and old conventional asphalt (2b). This resembles the tendencies in column 3 where PCA has detected variations in temperature according to the same division.

The attempt of supervised classification on the stack of five bands in Fig. 4.11, summarized in column 6, displays results comparable to the classification results discussed above. Marble and vegetation are clearly distinctive. There are three types of asphalt visible, but again they are not entirely in accordance with the known information about asphalt. It seems that the light grey color is indicative of the old conventional asphalt (2a and 2b), while parts of the streets with the cool coating (1) and new conventional asphalt (3) are both marked with dark grey and brown. Attempts have been made to classify concrete as a separate class, but without success. The difference between this classification method and the unsupervised classification methods mentioned above is that more classes have been identified such as soil (black), water (dark blue), tiles for the blind (turquoise), grass (light green) and two types of trees (orange and dark green). However, the types of trees identified here as two classes cannot be validated.

There are two similarities visible in all five columns: vegetation is clearly identified and concrete is not identified as separate class in any of them. Apart from this, it can be said that the variations detected with PCA on the IR stack, k-means clustering and MLC on the reflectance stack, columns 3, 5, 6 in Table 4.2, give largely similar results as opposed to the NDVI classification and PCA performed on the reflectance stack, columns 2 and 4. The results in columns 2 and 4 do not show differences between impervious materials, which the results in columns 3, 5 and 6 indicate. The achievements and, at the same time, limitations in columns 3, 5 and 6 are that all three classification methods characterized new conventional asphalt, asphalt with cool coating and old conventional asphalt (2b) on the one hand, and old conventional asphalt (2a) and concrete on the other hand. Inspecting Fig. 3.6a and 3.6b, it is visible that old conventional asphalt has lighter color. The asphalt in the area is affected by "weathering effects and degradation of the streets due to the high traffic" [38]. Old conventional asphalt in position 2a and concrete in position 5 seem to have the same color e.g. same reflectance. It can therefore be deduced that the classification is affected by the degradation of the urban surfaces.

The above discussed results imply that the classification methods could be used in constructing more detailed emissivity maps than the one constructed in Fig. 4.9 based only on the NDVI map. As noted in Section 4.2, the NDVI

map in Fig. 4.8 does not show any differences between marble, concrete and the three asphalt types. This limitation is in accordance with the NDVI maps created during an earlier investigation of the study area [37]. It is also confirmed by Oltra-Carro et al stating that "the NDVI threshold method does not appear to be capable to distinguish between different artificial surfaces" [50]. A more detailed identification is possible with k-means clustering and MLC on a reflectance stack of five bands as well as with PCA on IR stack. This could result in more emissivity classes and a more precise emissivity correction.

5.3 The maximum surface temperature T_{smax}

This section analyses the results of Section 4.3. First of all, the potential of ATI will be analyzed in obtaining predictions of surface temperature in Section 5.3.1. Secondly, Eq. 19 is analyzed for its possibilities in predicting maximum surface temperature with respect to TI and albedo in Section 5.3.2. Finally, parametrization of the maximum surface temperature T_{smax} will be discussed in Section 5.3.3.

5.3.1 The model of apparent thermal inertia (ATI)

The following section analyses the ATI maps in Fig. 4.20. The first part of the analysis focuses on the ATI maps with respect to the weather conditions. The second part assess the maps with respect to the five material types and the third part draws the conclusion on this model.

5.3.1.1 Comparison of the temperature and ATI maps based on the weather conditions

As mentioned in Section 4.3.1, both Fig. 4.12 and 4.13 show that the study area experienced the highest irradiation on 20 June, lower on 19 June and the lowest on 12 April. The air temperatures measured on 12 April and 20 June in Fig. 4.14 and 4.15 reflect the amount of incoming irradiation on these two days. The measured air temperature is the lowest 12 April and the highest 20 June. From Fig. 4.15 it is visible that there was no rain in April prior to 12 April and that there were considerable rainfalls in the middle of June 2017 as late as one day before the data collection started. It is thus expected that the ground in the study area was still wet on 19 June.

Contrasting Fig. 4.14 and Fig. 4.15, there seems to be discrepancy in them with respect to the measured maximum air temperature on 12 April, 19 June and 20 June. The temperatures shown in Fig. 4.15 are considerably lower than the maximum air temperature shown in Fig. 4.14. The reason for that could be in the sources of the air temperature data. The values displayed in Fig. 4.14 were collected in the study area. The values shown in Fig. 4.15 show average values obtained from a weather station and from an online weather service [58]. In that sense Fig. 4.14 might show a more realistic picture of the study area.

Surface temperature T_s , diurnal temperature difference ΔT and ATI maps reflect the observed tendencies in irradiation and air temperature. Even though the irradiation on 12 April was the lowest out of four days, the surface temperature T_s in the middle of the day on 12 April, Fig. 4.16b, reached 50°C the same way as on 20 June, Fig. 4.17g. Because of high surface temperatures during these two days, Fig. 4.18a and 4.18c show high temperature difference ΔT . The explanation for these observations for 12 April might thus not be in the irradiation for that particular day but in the sunny weather conditions with air temperature above 20°C since 3 April. It is plausible to think that the impervious surfaces experienced constant warming under continuous solar irradiation for days prior to 12 April. The weather tendencies prior to 19 June are also reflected in Fig. 4.17a-4.17e and 4.18b. Even though Fig. 4.13 shows that irradiation on 19 June was higher than on 12 April, several days with rainfall prior to 19 June are reflected in relatively low temperature differences on that day. Correspondingly, due to relationship of inverse proportionality, ATI maps as a whole in Fig. 4.20a and 4.20c have lower values compared to the values in Fig. 4.20b.

The accuracy of these maps has to be assessed in the light of the results discussed in Section 5.1. Figure 4.6 indicates that *FLIR* temperature in the maps is corrected to the reference level measured by *Optris* camera, but at the same time it seems that the fluctuations remain to a certain extent. At the same time, as discussed in reference to Fig. 4.5, it does not seem that the fluctuations go beyond 1.5°C, which is within the uncertainty of the *Optris* camera. That is why the uncertainty of +/- 2°C will be considered valid for the images of surface temperature T_s from 2017 in the same way as for those taken in 2016. The uncertainty in the diurnal temperature difference ΔT maps is +/- 4°C. The quantitative values of error in ATI maps will be addressed in Section 5.3.1.2.

Similarity between all three ATI maps in Fig. 4.20 is manifested in the ATI-values of vegetation being higher than the values of impervious materials. This is to be expected since the variation in daily temperature difference is considerably smaller for vegetation compared to impervious materials. ATI is, however, sensitive to measurements in regions with lower diurnal temperature difference [28] because of propagation of errors through

$$\frac{\delta ATI}{|ATI|} = \frac{\delta \alpha}{|\alpha|} + \frac{\delta \Delta T}{|\Delta T|} \quad (32)$$

where δATI is the uncertainty on apparent thermal inertia, $\delta \alpha$ is uncertainty on albedo and $\delta \Delta T$ is uncertainty on diurnal temperature difference. It is visible from Eq. 32 that a higher uncertainty in ATI is given by smaller diurnal temperature differences ΔT [28] as well as smaller albedo. Based on this, it can be argued that the ATI map from 19 June also has higher uncertainty than the maps from 12 April and 20 June.

According to Price, "apparent thermal inertia should not be used in regions having variability in surface moisture" [60]. However, as it was mentioned in Chapter 2, ATI has been widely used in the recent years analyzing surfaces with variable moisture with the aim of determining water content in soil. The reason is that "ATI represents the temporal and spatial variability of soil and canopy moisture" [20], [29]. ATI values reflect the moisture content because they exhibit lower diurnal temperature fluctuation. An increasing soil moisture content of the surface leads to a proportional increase in TI and reduction in fluctuations of the daily surface temperature [29].

Moisture, however, is not a scope of present study. It is also not a parameter of weather conditions of a particular day which could help in assessing the surface temperature in the long term. It reflects the effects of weather conditions from the days prior to 19 June which remained in the study area. Thus, the map from 19 June will not be taken in the further analysis when assessing the values of ATI for the different materials under dry conditions.

5.3.1.2 Material-wise comparison of the ATI maps of dry surfaces

It is considered here as plausible to assume that the materials dried until 20 June with the whole day of dry weather on 19 June. It was also discussed

earlier that the weather prior to 12 April was stable, dry and sunny. Thus, it is assumed that ATI maps from 12 April and 20 June are showing dry surfaces. Together with the maps of diurnal temperature difference ΔT and the albedo maps, they will be analyzed with respect to the different materials as labelled in Fig. 3.1.

Inspecting the maps material-wise, Fig. 4.18a and 4.18c show that the new conventional asphalt and asphalt with cool coating have the highest temperature differences, followed by old conventional asphalt and concrete and finally marble. This material-wise variation in temperature was also captured in the score image of the first principal component in Fig. 4.7. Thus it can be said that the variations in temperature of the impervious materials can be broadly divided into these three groups. The overview of the diurnal temperature differences ΔT and its relative error is listed in Table 5.1. The temperature is decreasing from the top to the bottom of the table and increasing from left to right.

Table 5.1: Overview of the ΔT values for different materials as shown in Fig. 4.18.

Material	12 April	12 April	20 June	20 June
	ΔT [°C]	$\frac{\delta \Delta T}{ \Delta T }$ [%]	ΔT [°C]	$\frac{\delta \Delta T}{ \Delta T }$ [%]
Asphalt with cool coating (1)	25-33	12-16	33-35	11-12
New conventional asphalt (3)	29-33	12-14	33-35	11-12
Old conventional asphalt (2a, 2b)	25-30	13-16	27-32	12-15
Concrete (5)	27-30	13-15	27-28	14-15
Marble (4)	18-22	18-22	24-28	14-17

The same type of overview has been made for albedo values in Table 5.2 based on the observations made in Fig. 4.19. As mentioned earlier, the error in the albedo maps is not possible to assess so Table 5.2 does not contain that information. Values from the two albedo images show that the albedo from 2016 is generally somewhat lower than the albedo recorded in 2017 for all three types of asphalt and concrete. The values for marble are somewhat larger. It is difficult to assess what the reason for that is partly because there is no available information about the error in the albedo maps.

However, this difference between albedo values between 4.19a and 4.19b is plausible for conventional asphalt whose albedo is very low in the beginning, but increases with time due to weathering, ageing and exposure [35], [36], [37], [38], [61]. Figure 4.19b is created based on images taken one year after

the images taken for Fig. 4.19a. It is thus possible that these effects are visible in position 2a, 2b and 3. On the contrary, the albedo of concrete and asphalt with cool coating is high in the beginning and decreases with time due to same reasons [37], [38], [62], [63]. It is therefore not plausible that the albedo in the map from 2017 should be higher in positions 1 and 5.

Assessing the albedo values from top to bottom, e.g. from lowest to highest values, and comparing them with values in Table 5.1, it is visible that the biggest differences in diurnal temperature occur in the places where the albedo values are the lowest. Thus, the biggest absorption of solar irradiation happens in asphalt with cool coating and new conventional asphalt followed by the old conventional asphalt, concrete and marble. This is in accordance with studies showing that maximum surface temperature T_{smax} increases with absorptivity $(1 - \alpha)$ [26], [64], [65].

Table 5.2: Overview of the albedo α values for different materials as shown in Fig. 4.19.

Material	12 April	20 June
	α	α
Asphalt with cool coating (1)	0.16-0.19	0.22-0.26
New conventional asphalt (3)	0.17-0.21	0.24-0.27
Old conventional asphalt (2a, 2b)	0.21-0.25	0.27-0.31
Concrete (5)	0.28-0.31	0.31-0.32
Marble (4)	0.35-0.43	0.35-0.19

Figure 5.1 shows the same ATI maps from 12 April and 20 June from Fig. 4.20 with increased contrast $[0.03, 0.06] [K^{-1}]$ so that the variations in the study area are more pronounced. The ATI values for vegetation are beyond $0.06 [K^{-1}]$ and this is the reason why the color shows saturation on the images. An overview of the values from these two maps is displayed in Table 5.3. Since the information about error in the albedo maps is lacking, the relative error listed in Table 5.1 applies also to ATI. Even though it does not provide the complete picture about how large the error is, it gives an impression of the order of magnitude of the error which can be expected in the ATI maps.

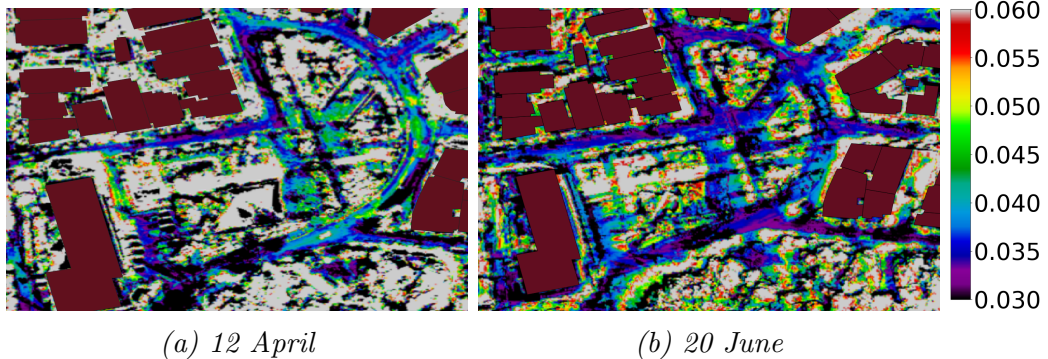


Figure 5.1: Increased contrast on the normalised ATI maps [K^{-1}] with respect to solar irradiation for 12 April and 20 June.

Table 5.3: Overview of the ATI values for different materials as shown in Fig. 5.1.

Material	12 April	20 June
	ATI [K^{-1}]	ATI [K^{-1}]
Asphalt with cool coating (1)	0.030-0.035	0.027-0.033
New conventional asphalt (3)	0.036-0.038	0.031-0.033
Old conventional asphalt (2a, 2b)	0.037-0.042	0.030-0.038
Concrete (5)	0.034-0.036	0.036-0.038
Marble (4)	0.039-0.045	0.033-0.037

Due to the inverse proportional relationship between diurnal temperature difference ΔT and ATI one might, by looking at Eq. 20, expect that the values in the ATI-maps in Fig. 4.20 would be exactly the inverse from the values in the ΔT -maps [66]. However, this "is a rather simplistic observation because there are some subtle deviations for specific features due to albedo variations" [66]. Thus, the albedo variations shown in Fig. 4.19 can give an explanation why the ATI values of all the impervious materials do not reflect the same material-wise patterns in the diurnal temperature difference ΔT maps. The only visible difference on the material level in Fig. 5.1a and 5.1b is marble's higher ATI values compared to asphalt's. Marble is colored green and blue compared to asphalt which is at certain places colored purple. Marble has the highest albedo and the lowest ΔT , while it is exactly the opposite for asphalt. It is also important to mention that marble has higher thermal conductivity than asphalt. The difference in temperature between them can be an effect of conductivity as well [37], [67].

Nevertheless, even though the inverse proportionality is not entirely reflected in each material on the ATI maps due to albedo values, the two ATI maps and Table 5.3 show that the values on 20 June are somewhat lower than on 12 April across all the materials. The colors dominating the ATI map from 12 June are green and blue. The ATI map from 20 June is predominantly blue and purple. The same tendency is recorded in Table 5.1 showing somewhat higher values of ΔT on 20 June as opposed to 12 April.

5.3.1.3 The ATI model

The analysis so far has confirmed prior studies according to which the ATI model captures temperature differences between dry and moist surfaces. When modelling surface temperature, it is necessary to bear in mind this parameter. The relation between the maps is in this case different as opposed to relation between the maps of dry surfaces (Appendix A).

ATI maps also seem to capture the difference in the diurnal temperature variations between dry surfaces. However, no clear indications about material-wise differences have been noted. There could be two reasons for that. One reason is the relatively high error in ATI maps due to error propagation. It was listed in Table 5.1 that the error in ΔT maps varies between 11-22%. The error in the ATI maps is at least that high. Another reason could be the differences observed in the two albedo maps in Fig. 4.19a and 4.19b. A more detailed analysis of the background for the differences of the albedo maps would be necessary. Keeping albedo values constant in combination with a bigger number of ATI maps, meaning data collection performed over several days, might give a possibility to understand the surface temperature development of a particular material from day to day based on the ATI model.

5.3.2 The model based on thermal inertia (TI)

Fig. 4.21 shows that it is neither possible to conclude when the phase shift of the temperature curves compared to the incoming irradiation takes place, nor when the maximum surface temperature occurs for the different materials. Nevertheless, an attempt has been made using the approximation to the maximum surface temperature from midday measurements to obtain a linear regression model based on Eq. 19. Fig. 4.22 shows successfully that

the maximum surface temperature T_{smax} is a linear function of materials' absorptivity $(1 - \alpha)I_0$. This is confirmed by earlier studies [26], [64], [65], as mentioned in the last section. The measurement points of the material which has the highest temperature (asphalt) is placed furthest to the right indicating that the absorption is the greatest. The temperature of the material which has the lowest temperature (marble) also has the lowest absorption.

The slopes of the functions show that the relationship between the maximum surface temperature T_{smax} and the reciprocal thermal inertia P is linear [26]. The slopes contain the information about the thermal inertia P and thus about the thermal resistance of the material as shown in Table 4.3. A steeper slope indicates a higher increase in the maximum daily surface temperature of a material per watt per square meter of absorbed power which again indicates a lower resistance to heating. The material with the steepest slope and lowest TI is asphalt, followed by marble and lastly concrete. This indicates that concrete's maximum diurnal temperature increases less than marble's per amount absorbed energy. Even though it is difficult to validate the values for TI obtained here because urban materials have a wide range of different values (Niki Gaitani, private communication), it appears at least that values for asphalt and concrete might be in the correct order of magnitude. The value for TI of asphalt found in the literature is $1\ 205\ J\ m^{-2}\ K^{-1}\ s^{-1/2}$ which is in very good accordance with the value obtained here. The value for concrete is $1\ 785\ J\ m^{-2}\ K^{-1}\ s^{-1/2}$ [24].

In addition to the absorptivity and the slope, the maximum surface temperature of a material seems to be highly influenced by the regression constant crossing the y-axis. The regression constants in all three cases have considerable values: -24.3 K for asphalt, -7.24 K for marble and +6.16 K for concrete. The regression constant can be interpreted as the temperature of the material when there is no absorptivity. Looking at the variables on the x-axis this could be the case either when the material has perfect reflection or when there is no solar irradiation. For the data here it could be interpreted as the predicted starting temperature of a particular material before the sunrise. Even though the numbers are not realistic particularly for the time of the year when the measurements were conducted, the relative differences between the numbers could be indicative of the starting temperature of the materials. There are indications in the data from April and June that marble's temperature in the morning is lower than concrete's temperature.

As mentioned above, Fig. 4.22 is indicative of albedo's important role in the tendencies observed among the three materials as far as maximum sur-

face temperature is concerned. It is understood that due to low albedo, e.g. high absorptivity, a material will always absorb more than a material with high albedo, also when solar radiation is lower. Looking at Fig. 4.22, the decline in irradiation has to be considerable in order for the maximum surface temperature of asphalt to fall considerably. This observation is supported by Taha who claims that "[t]he contribution of lower albedos to heat islands can be significant" [36]. At the same time, Qin argues that "increasing the thermal inertia is less effective to develop cool pavements than increasing the albedo" [26]. Figure 4.22 seems to confirm this particularly with respect to concrete and marble. The slopes of the described curves indicate how much the temperature will rise given an amount of absorbed energy. However, it is the albedo which governs how much energy will be absorbed at all. In the words of Tramutoli et al "[t]he quantity of heat absorbed by the surface [...] determines an increase of the surface temperature and the amount of such increase (ΔT), depends on thermal inertia" [20].

In order to use the presented curves as predictors of the maximum surface temperature, validation studies are necessary to further confirm or contradict the dynamics described here. The observations here indicate that marble has a higher TI than concrete and that its temperature thus might increase more given the same irradiation. On the other hand, marble is the material which has the highest conductivity of the three materials examined [37], [67]. Further investigation could also bring this variable into the scope of analysis. More investigation is also necessary because the maximum temperature used here approximates the highest daily temperature. Measurements carried out with higher time resolution are therefore necessary to find as accurately as possible when the maximum daily temperature occurs. Measurements over several days should also be conducted in order to obtain more points for a more accurate regression. Furthermore, a bigger insight into the error propagation in the method calculating the albedo is also necessary.

5.3.3 Parametrization of the maximum surface temperature T_{smax}

Parametrizing surface temperature with maximum solar elevation and temperature difference between the surface T_s and air temperature T_a seems to

give plausible sinusoidal curves with respect to the measurement points from 20 June.

The author is not familiar with any parametrization attempts of concrete and marble and therefore it is not possible to compare the parametrization formulas obtained in Fig. 4.23b and 4.23c. Comparing the values for η obtained for concrete and marble is indicative of their maximum temperatures. Value of η for concrete is higher than for marble confirming the fact that concrete's maximum daily temperature was higher than marble's.

However, parametrization expression derived by Lindberg et al [57] can be compared with the result of the trial and error method performed here. The two parametrization expressions deviate from one another in two respects. The first difference is the amplitude which is given by the variable η . The value 0.58 seems to give a too high amplitude for the sinus curve with respect to the measurement points. Secondly, the green curve seems to have a smaller period compared to the orange one. The reason for this is the value b . It seems therefore that the points are better fitted with a curve which has a larger period, a larger variable for b , and smaller amplitude, e.g. smaller η .

The reasons why the parametrization suggested by Lindberg et al [57] does not seem to fit the measurement points so well could be simply because the asphalt used to pave the streets in Athens is not the same as the one which temperature measurements were carried out on in [57]. There is no information about the composition of the two types of asphalt. Furthermore, the parametrization model does not take into account neither the TI nor the albedo. It would be interesting to know these material characteristics with respect to the two asphalt types. This knowledge might affect or give explanation about values η and b . Another limitation with the presented analysis is that the time of the day when the maximum surface temperature occurs on the materials is not known from the data gathered in June 2017. This goes for both asphalt, concrete and marble. Apart from the necessity to collect more information about the materials parametrized, the method of predicting surface temperature using the maximum solar elevation and the air temperature seems to show potential. In addition, validation and further investigation is necessary to confirm or contradict the discussed results. Measurements of the surface temperature and air temperature should be conducted over a longer period of time in order to validate the parametrization expressions for the three materials.

5.4 Overview

Analysis concerning *FLIR* and *Opbris* cameras showed that the conversion factor c_f calculated was successful in eliminating the deviation of the measurements by the *FLIR* camera with respect to the reference temperature. However, test data is needed to confirm that this is the case for data not used in the model. The conversion factor c_f was also successful in eliminating fluctuations to a certain extent depending on the temperature of the object. The fluctuations when measuring temperature of objects similar to the one of the black plate, around 20°C, will most likely not be removed. The pixel values in the maps produced in Pix4D are already averaged by the software, so in that way fluctuations from one image to another of the same object might have been eliminated to a certain extent. More measurements are necessary both in the laboratory and with the cameras connected to the drone in order to have data from a wider range of situations and conditions which would give a more accurate conversion factor c_f .

Section 5.2 dealt with the analysis of the classification methods by PCA, k-means and MLC of the materials in the study area based on the stack of thermal maps and a stack of reflectance maps. Even though the classification methods did not manage to separate all five material groups from each other, they showed greater potential in recognizing classes than the threshold method based on the NDVI map. Thus, the achievement of these methods is that they could be used to obtain a more detailed and accurate emissivity maps with more classes for a more accurate temperature correction of IR maps.

In Section 5.3.1.1 it was confirmed that ATI maps can be used as an indication of surface moisture. Moisture as additional parameter would then have to be taken into consideration when predicting surface temperature. ATI maps also seem to capture the overall differences in the diurnal temperature on dry surfaces. However, it is difficult to get clear indications about differences on material level. It is important to bear in mind that the error in the ATI maps is relatively high, also without taking into consideration the error from the albedo maps as was the case in this thesis. More ATI maps based on data collection performed over several days might give better indications of the relationships between them.

Section 5.3.2 identifies linear regression based on Eq. 19 as method that shows potential for predicting maximum surface temperature given the albedo

and the daily maximum solar irradiation. The linearly regressed curves for asphalt, concrete and marble show the important role of albedo for the surface temperature which is also confirmed in the literature. Albedo seems to govern how much heat will be absorbed and thus the increase in temperature. The slope of the regressed curves, e.g. TI, gives an indication of the amount of such increase. A validation of the dynamics observed in Fig. 4.22 should be conducted. This is also necessary because the maximum surface temperature of the materials is not known.

Section 5.3.3 concludes that parametrization of asphalt, concrete and marble shows potential. However, measurements of the surface temperature and air temperature should be conducted over a longer period of time in order to validate the parametrization expressions found by trial and error method. Comparison of the parametrization obtained for asphalt with the expression found by Lindberg et al [57], indicates deviations both in the amplitude and the period of the sinusoidal curve. The cause of this could simply be the differences in asphalt in Athens and the one which the measurements were conducted on in [57]. Ideally, detailed material characteristics should be known.

6. Conclusion

The present study sought to analyze and evaluate methods which could be suitable in predicting developments of the maximum surface temperature of different materials in Municipality of Ymittos, Athens. The ultimate goal was to provide a bigger insight into how surface temperature develops. The reason is that it is the surface temperature in urban materials which greatly contributes to additional warming of cities, UHI.

The study used remote sensing methods, more concretely high resolution images in VIS, NIR and IR bands collected with a UAV during two study trips in April 2016 and June 2017. Since two different IR cameras were used, it was first necessary to assess their performance. It has been found that the *FLIR* camera used in June 2017 is not as reliable as *Optris* used in April 2016 due to large measurement offset and considerable fluctuations in measurement. A conversion factor was found for this offset which partly also corrects the fluctuations. More test data is needed with known surface temperature. Further investigation is necessary with data collected in different settings as well as from drones with both cameras for a more accurate conversion factor.

Data analysis based on remote sensing methods requires that the user is able to manipulate the images in order to, for example, perform corrections. Classifying different groups of pixels is an important segment of analysis. PCA and statistical methods for (un)supervised classification k-means clustering and MLC, were tested on the study area. Their performance showed potential. They were able to provide better results compared to classification based on NDVI threshold.

Based on the findings from these two parts of data analysis, it was possible to obtain maps of apparent thermal inertia from corrected temperature and albedo maps. Temperature maps were also used for parametrization of surface temperature as well as for linear regression of surface temperature

based on materials' absorptivity. Assessments have been made on these three methods as to how they can be used in order to predict surface temperature of different materials. ATI model captures temperature differences based on moisture very well. At the same time, it gives indications about temperature differences on dry surfaces. A more detailed analysis with bigger temporal resolution would be necessary in order to assess the full potential of the ATI maps in predicting surface temperature. Knowledge of error propagation is also vital in this respect.

The linear regression model using the albedo and TI is a promising model which gives interesting insights into surface temperature. Literature confirms that lower albedo is decisive in decreasing surface temperature of urban materials. The interplay of albedo and TI here is an interesting subject to study. This is due to the fact that TI indicates how much the surface temperature will rise given a particular amount of absorbed irradiation.

Last but not least, parametrization of surface temperature knowing the maximum solar elevation and the air temperature shows potential in predicting maximum surface temperature. Validation studies of the parametrization expressions found in this study are necessary. In addition, it would be interesting to evaluate and combine the role of albedo and TI with respect to this methodology.

Bibliography

- [1] Abbas Mohajerani, Brkic Jason, and Jeffrey-Bailey Tristan. “The urban heat island effect, its causes, and mitigation, with reference to the thermal properties of asphalt concrete”. In: *Journal of Environmental Management 197* (2017).
- [2] URBANFLUXES. *Welcome to the URBANFLUXES Project*. 2015. URL: <http://urbanfluxes.eu/>.
- [3] Voogt J.A. and Oke T.R. “Thermal remote sensing of urban climates”. In: *Remote Sensing of Environment, Volume 83* (2003).
- [4] Mills Gerald. “Urban Climatology: History, status and prospects”. In: *Urban Climate (10)* (2014).
- [5] Burud Ingunn, Thiis Thomas Kringlebotn, and Gaitani Niki. “Reflectance and thermal properties of the urban fabric studied with aerial spectral imaging”. In: *Proceedings Volume 10444, Fifth International Conference on Remote Sensing and Geoinformation of the Environment (RSCy2017)* (2017).
- [6] Cengel Yunus A. and Ghajar Afshin J. *Heat and Mass Transfer: Fundamentals and Applications*. McGraw-Hill Education, 2015.
- [7] Campbell James B. and Randolph H. Wynne. *Introduction to Remote Sensing*. The Guilford Press, 2011.
- [8] Thenkabail Prasad S., ed. *Remote Sensing Handbook, Volume I*. CRC Press, 2016.
- [9] Thenkabail Prasad S., ed. *Remote Sensing Handbook, Volume III*. CRC Press, 2016.
- [10] Kuenzer Claudia and Dech Stefan. “Theoretical Background of Thermal Infrared Remote Sensing”. In: Claudia Kuenzer and Stefan Dech. *Thermal Infrared Remote Sensing: Sensors, Methods, Applications*. Springer, 2013.

- [11] Vollmer M. and Möllmann K.-P. *Infrared Thermal Imaging: Fundamentals, Research and Applications*. WILEY-VCH Verlag GmbH and Co., 2010.
- [12] Usamentiaga Ruben et al. “Infrared Thermography for Temperature Measurement and Non-Destructive Testing”. In: *Sensors* (2014).
- [13] Quang Hui Tran et al. “Effects of Ambient Temperature and Relative Humidity on Subsurface Defect Detection in Concrete Structures by Active Thermal Imaging”. In: *Sensors* (2017).
- [14] Vasterling Margarete and Meyer Uwe. “Challenges and Opportunities for UAV-Borne Thermal Imaging”. In: *Thermal Infrared Remote Sensing: Sensors, Methods, Applications*. Springer, 2013.
- [15] Wenfeng Zhan et al. “Assessment of thermal anisotropy on remote estimation of urban thermal inertia”. In: *Remote Sensing of Environment* 123 (2012).
- [16] Sabins Floyd F. *Remote Sensing: Principles and Applications*. Wave-land Press, 1997.
- [17] Sabol Donald D. et al. *Differential Thermal Inertia of Geological Surfaces*. URL: http://gis.ess.washington.edu/keck/raqrs_files/RAQRS_II_Sabol.pdf.
- [18] Sohrabinia Mammattand, Rack Wolfgang, and Zawar-Reza Peyman. “Soil moisture derived using two apparent thermal inertia functions over Canterbury, New Zealand”. In: *Journal of Applied Remote Sensing* (2014).
- [19] Kuenzer Claudia, Gessner Ursula, and Wagner Wolfgang. “Soil Moisture from Thermal Infrared Satellite Data: Synergies with Microwave Data”. In: *Thermal Infrared Remote Sensing: Sensors, Methods, Applications*. Springer, 2013.
- [20] Tramutoli Valerio et al. *Feasibility of hydrological application of thermal inertia from remote sensing*. 2000. URL: http://www.idrologia.polito.it/~claps/Papers/Plinius_Siena.PDF.
- [21] Schieldge John P. et al. “Use of thermal-inertia properties for material identification”. In: *SPIE*, Vol. 238 (1980).
- [22] Swiss Federal Institute of Technology ETH. *Radiation, Sensible Heat Flux and Evapotranspiration*. n.d. URL: <http://profile.nus.edu.sg/fass/geomr/roth%20uhi%20hefd13.pdf>.
- [23] Roth M. *Chapter 11: Urban Heat Islands*. 2013. URL: <http://profile.nus.edu.sg/fass/geomr/roth%20uhi%20hefd13.pdf>.

- [24] International Association for Urban Climate. *The Urban Canopy Layer Heat Island*. 2014. URL: <https://www.epa.gov/sites/production/files/2014-06/documents/heatislandteachingresource.pdf>.
- [25] Young-Hee Ryu and Jong-Jin Baik. “Quantitative Analysis of Factors Contributing to Urban Heat Island Intensity”. In: *Journal of Applied Meteorology and Climatology* 51 (2011).
- [26] Yinghong Qin. “Pavement surface maximum temperature increases linearly with solar absorption and reciprocal thermal inertia”. In: *International Journal of Heat and Mass Transfer* 97 (2016).
- [27] Xue Y. and Cracknell A.P. “Advanced thermal inertia modelling”. In: *International Journal of Remote Sensing* (1995).
- [28] van doninck Jasper et al. “The potential of multitemporal Aqua and Terra MODIS apparent thermal inertia as a soil moisture indicator”. In: *International Journal of Applied Earth Observation and Geoinformation* (2011).
- [29] Verstraeten Willem W. et al. “Soil moisture retrieval using thermal inertia, determined with visible and thermal spaceborne data, validated for European forests”. In: *Remote Sensing of Environment* 101 (2006).
- [30] Yinghong Qin. “A review on the development of cool pavements to mitigate urban heat island effect”. In: *Renewable and Sustainable Energy Reviews* 52 (2015).
- [31] Qin Yinghong et al. “The amplitude and maximum of daily pavement surface temperature increases linearly with solar absorption”. In: *Road Materials and Pavement Design* 18:2 (2017).
- [32] Anne B. Kahle. “Surface emittance, temperature, and thermal inertia derived from Thermal Infrared Multispectral Scanner (TIMS) data for Death Valley, California”. In: *Geophysics*, Vol. 52 (1987).
- [33] Minacapilli M., Iovino M., and Blanda F. “High resolution remote estimation of soil surface water content by a thermal inertia approach”. In: *Journal of Hydrology* 379 (2009).
- [34] J.C. Price. “Thermal inertia mapping: A new view of the Earth”. In: *Journal of Geophysical Research*, Vol. 82 (1977).
- [35] Li H., Harvey J., and Kendall A. “Field measurement of albedo for different land cover materials and effects of thermal performance”. In: *Building and Environmental* Vol. 59 (2012).

- [36] Taha Haider, Sailor David, and Hashem Akbari. *Field measurement of albedo for different land cover materials and effects of thermal performance*. Report. University of California, 1992.
- [37] Gaitani Niki et al. “High-resolution spectral mapping of urban thermal properties with Unmanned Aerial Vehicles”. In: *Building and Environment*, Volume 121 (2017).
- [38] Gaitani Niki et al. “Aerial survey and in-situ measurements of materials and vegetation in the urban fabric”. In: *Procedia Engineering*, 180 (2017).
- [39] FLIR Commercial Systems. *FLIR Camera Controller GUI*. 2014. URL: https://www.flir.com/globalassets/imported-assets/document/flir_gui_user_guide.pdf.
- [40] Pix4D. *Pix4D*. 2018. URL: <https://pix4d.com/>.
- [41] Pix4D. *Photo Stitching vs Orthomosaic Generation*. 2018. URL: <https://support.pix4d.com/hc/en-us/articles/202558869-Photo-Stitching-vs-Orthomosaic-Generation>.
- [42] Pix4D. *How to verify that there is Enough Overlap between the Images*. 2018. URL: <https://support.pix4d.com/hc/en-us/articles/203756125-How-to-verify-that-there-is-Enough-Overlap-between-the-Images>.
- [43] Pix4D. *How to visualize the GeoTIFF DSM File*. 2018. URL: <https://support.pix4d.com/hc/en-us/articles/205084685-How-to-visualize-the-DSM-GeoTIFF-file#gsc.tab=0>.
- [44] Pix4D. *Difference between the Reflectance Map and the Orthomosaic*. 2018. URL: <https://support.pix4d.com/hc/en-us/articles/202739409-Difference-between-the-Reflectance-Map-and-the-Orthomosaic>.
- [45] Pix4D. *Reflectance Map*. 2018. URL: <https://support.pix4d.com/hc/en-us/articles/206455126-Reflectance-Map>.
- [46] Ban-Weiss George A., Woods Jordan, and Levinson Ronnen. “Using remote sensing to quantify albedo of roofs in seven California cities, Part 1: Methods”. In: *Solar Energy* 115 (2015).
- [47] Jon Shlens. *A Tutorial on Principal Component Analysis: Derivation, Discussion and Singular Value Decomposition*. 2003. URL: https://pdfs.semanticscholar.org/a99e/0f8f58af7a91e26c1eda54e0cca3e3e03df3.pdf?_ga=2.37575136.1956829095.1524691465-1062886422.1524691465.

- [48] Thomas Boggs. *Spectral Algorithms*. 2014. URL: <http://www.spectralpython.net/algorithms.html>.
- [49] Environmental Systems Research Institute. *NDVI function*. 2016. URL: <http://desktop.arcgis.com/en/arcmap/10.3/manage-data/raster-and-images/ndvi-function.htm>.
- [50] R. Oltra-Carrio et al. “Land surface emissivity retrieval from airborne sensor over urban areas”. In: *Remote Sensing of Environment Vol. 123* (2012).
- [51] Raschka Sebastian and Mirjalili Vahid. *Python Machine Learning*. Packt Publishing Ltd., 2017.
- [52] Luca Congedo. *Basic tutorial 1: Land Cover Classification of Landsat Images*. 2018. URL: <https://fromgistsors.blogspot.com/2018/02/basic-tutorial-1.html>.
- [53] Lindberg Fredrik et al. “Urban Multi-scale Environmental Predictor (UMEP) - An integrated tool for city-based climate services”. In: *Environmental Modelling & Software Vol. 99* (2017).
- [54] National Renewable Energy Laboratory. *Bird Clear Sky Model*. 2016. URL: <http://rredc.nrel.gov/solar/models/clearsky/>.
- [55] Bogren J. et al. “The impact of screening on road surface temperature”. In: *Meteorological Applications* (2000).
- [56] Lindberg Fredrik, Thorsson Sofia, and Holmer Björn. “SOLWEIG 1.0 - Modelling spatial variations of 3D radiant fluxes and mean radiant temperatur in complex urban settings”. In: *International Journal of Biometeorology* (2008).
- [57] Lindberg Fredrik, Onomura Shiho, and Grimmond C.S.B. “Influence of ground surface characteristics on the man radiant temperature in ruban areas”. In: *International Journal of Biometeorology* (2016).
- [58] Time and Date AS. *Past Weather in Athens, Greece — April 2016l*. 2018. URL: <https://www.timeanddate.com/weather/greece/athens/historic?month=4&year=2016>.
- [59] Tinytag. *Data sheet*. 2018.
- [60] J.C. Price. “On the Analysis of Thermal Infrared Imagery: The Limited Utility of Apparent Thermal Inertia”. In: *Remote Sensing of Environment* (1985).
- [61] Sen Sushobhan and Roesler Jeffrey. “Ageing albedo model for asphalt pavement surfaces”. In: *Journal of Cleaner Production 117* (2016).

- [62] Levinson Ronnen and Akbari Hashem. “Effects of composition and exposure on the solar reflectance of portland cement concrete”. In: *Cement and Concrete Research* 32 (2012).
- [63] Dornelles Kelen, Caram Rosana, and Sichieri Eduvaldo. “Ageing albedo model for asphalt pavement surfaces”. In: *Journal of Cleaner Production* 117 (2016).
- [64] Synnefa A., Santamouris M., and K. Apostolakis. “On the development, optical properties and thermal performance of cool colored coatings for the urban environment”. In: *Solar Energy* 81 (2007).
- [65] Pomerantz M. et al. *The effect of pavements' temperatures on air temperatures in large cities*. Report. Ernest Orlando Lawrence Berkeley National Laboratory, 2000.
- [66] Short Nicholas M. and Stuart Locke M. *The Heat Capacity Mapping Mission (HCMM) Anthology*. 1982.
- [67] Engineering ToolBox. *Thermal Conductivity of common Materials and Gases*. 2001. URL: https://www.engineeringtoolbox.com/thermal-conductivity-d_429.html.
- [68] Chen Yurong, Du Mingyi, and Dong Rentao. “Correlation between urban heat island effect and the thermal inertia using aster data in Beijing, China”. In: *The International Archives of the Photogrammetry, Remote Sensing and Spatial Information Science*, Vol. XXXVII (2008).
- [69] J. Wang et al. “A simple method for the estimation of thermal inertia”. In: *Geophysical Research Letters*, Vol. 37 (2010).
- [70] Wieke Heldens et al. “Analysis of Surface Thermal Patterns in Relation to Urban Structure Types: A Case Study for the City of Munich”. In: *Thermal Infrared Remote Sensing: Sensors, Methods, Applications*. Springer, 2013.

A. Appendix

Urban surfaces studied by VIS/NIR imaging from UAV – possibilities and limitations

I. Burud^{*a}, M. Vukovic^a, T. Thiis^a and N. Gaitani^b

^a Norwegian University of Life Sciences, Faculty of Sciences and Technology, P.O Box 2003, 1433 As, Norway;

^b Norwegian University of Science and Technology, Department of Architecture and Technology, Gløshaugen, Alfred Getz vei 3, NO-7491 Trondheim, Norway,

ABSTRACT

The present research approach aims at analyzing the relation between material properties and their thermal behavior using airborne multispectral imaging in VIS/NIR and IR with sensors mounted on Unmanned Aerial Vehicle (UAV). As a follow up to a pilot study from spring 2016, a survey including several flights spanned over three days, from early morning before sunrise until late evening after sunset, was carried out in Athens in June 2017. The camera specifications for the survey in 2017 were different than the ones used in 2016. The performance of the cameras was evaluated, taking into account atmospheric correction. The images have been combined to form maps of surface temperature distribution and material physical properties. The VIS/NIR images were used to classify the different surface materials, to compute a map of estimated albedo, and to construct a 3D-model of the area. By combining thermal maps with material classification, albedo information and local weather data, thermal material properties could be characterized for the various materials. The derived properties from this dataset yield valuable information for improved simulation models of urban climate.

Keywords: UAV, Thermal imaging, Multispectral imaging, Material properties, Thermal inertia

1. INTRODUCTION

In the field of urban climatology, special emphasis is given to the surface temperature of urban materials. The surface temperature modulates the temperature of the lowest atmospheric layers and is central to the surface energy balance and the human thermal comfort. Furthermore, this has a significant contribution to the phenomenon of the urban heat island (UHI) e.g. "modified thermal climate that is warmer than the surrounding non-urbanized areas, particularly at night" [1, 2]. The thermal inertia (TI) ($J \text{ m}^{-2}\text{K}^{-1} \text{ s}^{-1/2}$) of a material is a measure of its responsiveness to variations in temperature. It is one of the typical parameters for describing the thermal characteristics of subsurface materials and is defined as

$$TI = \sqrt{\rho c k} \quad (1)$$

where k is the thermal conductivity ($\text{W m}^{-1}\text{K}^{-1}$), ρ the bulk density (kg m^{-3}), and c the specific heat ($\text{J kg}^{-1}\text{K}^{-1}$) of the bulk soil material. Materials with a high heat capacity display high thermal inertia. Consequently such materials will show small changes in temperature through the diurnal cycle [3].

According to studies [4], higher thermal inertia is observed in urban areas than that of rural areas. However, remote estimates of urban thermal inertia show anisotropy effects due to thermal anisotropy [5].

In remote sensing TI is measured by diurnal changes in temperature. Apparent thermal inertia (ATI) gives a quantification of the effect of thermal inertia on surface temperature based on remotely sensed observations [6]. ATI have been computed from remote sensing measurements of the diurnal temperature amplitude (DTA), the albedo (a), and the incoming solar radiation [7]. This approach was also applied in a similar UAV survey in 2016 [8,9].

In traditional satellite imagery the spatial resolution and the time sampling rate are usually limited. Aerial survey using UAV's makes it possible to obtain high resolution geo-referenced thermal and visible/NIR maps of an area at flexible time intervals. A survey using UAV in Athens, Greece, is presented here in order to study thermal properties for urban surfaces in a particular suburb of Athens where measures have been taken in order to reduce the urban heat island effect.

In order to understand and mitigate UHI, it is a goal to accurately predict and simulate the urban microclimate. There are numerous simulation models developed for this purpose [10, 11, 12]. One particularly promising model is the SOLWEIG model [11] which utilizes a geographical information system (GIS) and is particularly computationally inexpensive due to efficient parameterization of the surface temperature of several urban materials. A linear relationship between maximum solar elevation and maximum difference between surface temperature, T_s , and air temperature, T_a , under clear sky conditions was used to estimate surface temperature, as

$$T_s - T_a = a * (\text{maximum solar elevation}) - b \quad (2)$$

where a and b are constants specific for each material. The following analysis is inspired by the SOLWEIG model and aims at improving future model simulations by improving the material parameters related to their thermal properties.

2. MATERIALS AND METHODS

2.1 Data acquisition

UAV measurements were carried out on June 2017 at the Municipality of Ymittos which is a suburb, situated 2.5 km southeast from the center of Athens, Greece, as a follow up to the survey carried out in 2016 [8,9]. An aerial RGB image from the survey is shown in Fig. 2. The study area is subject to the urban heat island effect, and several measures have been taken by the municipality to diminish the local temperature, such as using cool materials (cool coating on asphalt, marble) and by incorporating water, vegetation and solar shading devices.

Images from the UAV were obtained in the visible, NIR and IR part of the electromagnetic spectrum. The UAV used in the survey was a DJI Phantom 4 with a factory installed RGB camera with a GPS included. In addition to the RGB camera a rebuilt RGB camera where the blue channel is replaced by a NIR channel (Canon SX280 rebuild by Maxmax.com) was mounted on the UAV in order to obtain NIR images of the area. This camera also has an included GPS logger. Thermal (IR) images were obtained by mounting a radiometric IR camera (FLIR Vue Pro) with a 9mm lens on the UAV.

The pixel size of the pictures varied from 8-80 mm depending on the type of sensor. The flights were programmed to follow a predetermined route at an altitude of 100 meters and the cameras were set up to record every other second. A standardized grey calibration plate reflecting 60% of the solar radiation was recorded before and after each set of VIS/NIR images in order to calibrate for varying light conditions between the flights. In situ images of the different materials were also recorded with an RGB camera, an IR camera and the VIS/NIR camera.

In order to check for the influence of the atmosphere from the ground up to 100 m, measurements were carried out with the UAV centered on one geographical spot, lifting from 0 to 100 m and pausing approximately every 5 m, recording measurements. In addition, the radiometric accuracy of the thermal camera (FLIR vue pro R) was compared to the one used in the 2016 survey (Optis PI 640) by simultaneously recording the signal from materials with different temperatures in a laboratory environment. Weather data were obtained from a local weather station. In addition, in-situ measurements were conducted of air temperature and relative humidity (with shielded sensors) and of solar radiation (pyranometer).

The weather on June 18th, the day before the survey start had heavy rain, rather unusual for the season, as can be seen in Fig. 1 where precipitation and temperature are displayed from June 15th to June 22th. The soil and vegetation and some of the asphalt were therefore still moist at the start of the survey. On June 19th there was no precipitation but there were some clouds around noon. June 20th was a clear and sunny day, and June 21th was warm with a thin layer of clouds.

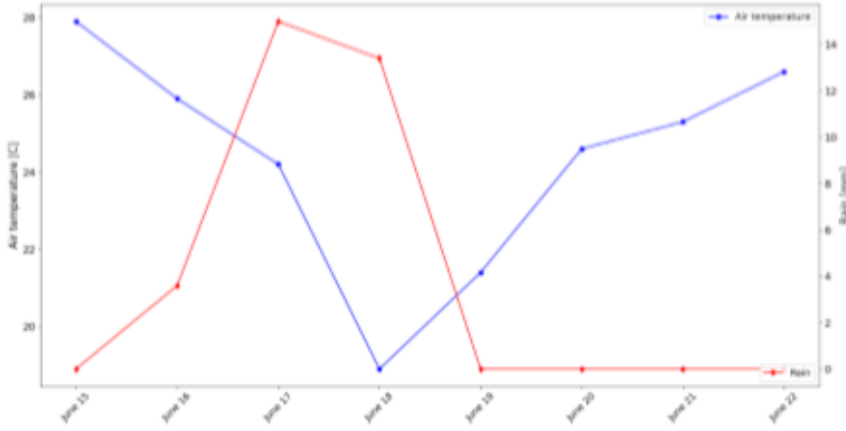


Fig 1. Daily mean values of temperature and precipitation in Athens from June 15th to June 22th 2017.

2.2 Data analysis and methodology

The RGB, VIS/NIR and IR images obtained with the UAV were combined and corrected for geometric distortions (orthorectification process) [13] using the software Pix4d [14]. From the RGB images a digital surface model (DSM) of the area was computed. GPS coordinates from the RGB camera were used to georeference the IR images. This was done by synchronizing time stamps from the two data sets using Exiftool [15]). The RGB, NIR and thermal maps were finally aligned to the detailed map of the buildings in the area provided by OpenStreetMap (openstreetmap.org) by manually selecting corresponding reference points using QGIS. This resulted in a stack of aligned images of all the observed wavelengths.

The stack of RGB, NIR and Normalized Differential Vegetation Index (NDVI) images was used to classify the various surface materials in the area. The algorithm for the computation of NDVI is given by equation (3):

$$NDVI = \frac{NIR - R}{NIR + R} \quad (3)$$

where NIR and R are reflectance values in the near infrared and red parts of the electromagnetic spectrum respectively. A supervised Maximum Likelihood classification was applied using Semi-Automatic Classification Plugin (SCP) from the open-source system QGIS. The classification was carried out based on region growing algorithm as an image segmentation method. This implies that pixels with spectral distance below a certain threshold value were selected as a region of interest [16].

The IR measurements as a function of height at the same spot indicated that the atmosphere had an influence of approximately 10% of the temperature value at 100 m. This complies well with theory [17] that has been implemented into the python function raw2temp that computes temperature from raw IR frames for various heights and weather conditions (humidity, air temperature) [18]. This effect should therefore be taken into account when studying absolute temperatures with a high accuracy camera. The analysis of the laboratory study of the two IR cameras (Optris and FLIR) showed that the Optris camera had a systematic error of 0.5 degrees and a fluctuation of 0.1 degrees whereas the FLIR camera had an offset error of 3 degrees and fluctuations of 0.5 degrees. These offsets and fluctuations are within the

stated errors from the camera producers. Given the high uncertainty of the FLIR camera it was concluded that the atmospheric effect was negligible compared to the overall accuracy of the FLIR camera in the 2017 survey.

The IR radiation emitted by a material depends not only on its temperature but also on the emissivity of the measured object. In order to obtain calibrated temperature values from the IR images, the emissivity of each surface material across the imaged area must therefore be taken into account. The classification of the RGB and NIR images was used to assign emissivity values to the thermal maps. Four classes of emissivity materials were selected from the literature [19]: water, asphalt, soil and vegetation and assigned to the surface materials classified with the Maximum Likelihood Classification algorithm.

In total nine surface temperature maps were obtained from early morning before sunrise on June 19th to noon on June 21th. The difference between the temperature obtained at 13:30 (maximum temperature) and the one from 05:30 (minimum temperature) was computed as the DTA on June 19th and 20th, and these were used to compute the ATI for these days.

The ATI was calculated using the equation [17]:

$$ATI = S * \frac{(1-\alpha)}{DTA} \quad (4)$$

where S is the solar fraction involving geographical location, local shading and α is the albedo. The albedo image was computed as described in [9] and ATI was computed with S representing the fraction of solar radiation relative to an area with no shadow.

The times series of temperature maps were also used to explore the thermal properties of the materials in the area. By combining the temporal distribution of the surface temperature of the different materials with the measured solar radiation revealed how fast the materials heat up and cool down relative to the daily solar elevation cycle. This is an indicator on the responsiveness of the materials to adapt to the surrounding temperature, i.e., their thermal inertia. However, this methodological approach requires the study of the non-shaded areas (i.e. the ones that have been exposed to solar radiation during the whole day). The digital surface model (DSM) combined with solar declination and geographical location were used to map the shadows in the area throughout the day, using the UMEP plugin as a part of QGIS [20]. This shadow map was then used to select unshaded regions to compute the temperature time series for the following materials: asphalt, concrete, marble, vegetation, water and soil. The classification of the materials described above was used to select the regions for each material. The maps of shadows with a sampling of once per hour through the day were also used to compute the cumulative daily solar radiation map for the area. In the shaded areas, only the diffuse solar radiation was included in the daily radiation map. Since the measured solar radiation was limited to the global horizontal radiation, the diffuse radiation was estimated by [21]

3. RESULTS AND DISCUSSION

3.1 Classification of materials

A section of the RGB image and the classification of the materials performed on the stack of RGB, NIR and NDVI are shown in Fig. 2. A total of 10 different classes were selected for a Maximum Likelihood Classification. Classes of asphalt, marble, soil, grass, trees, water, solar cells and roofs were chosen. Note that two different classes could be distinguished for the asphalt, which corresponds to color differences and different coatings of the asphalt. The asphalt marked as dark grey in Fig. 2b) has been covered with "cool coating", and the coating seems to be worn due to cars and weathering. There are therefore streets with an apparent mix of the two types of asphalt.

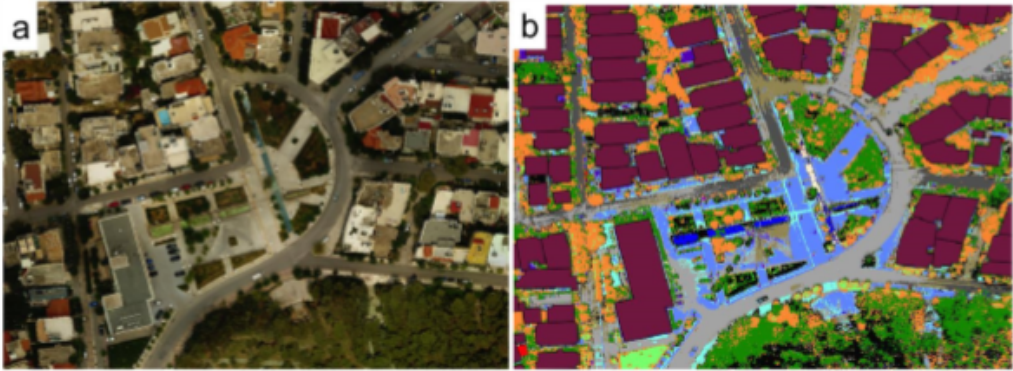


Fig 2. a) RGB image of the survey area in Athens, b) Classification of the surface materials of the area: green and orange = trees and bushes, black = soil, light green = grass, light blue = marble, dark blue =water, grey (dark and light)=asphalt, turquoise = tiles for blind, dark red = roofs.

A map of the solar radiation in each pixel from sunrise until 17:00 is shown in Fig. 3a), using the model based on the sun elevation and the 3D-model described above, the in-situ measurements of global horizontal radiation and the estimation of diffuse radiation by [21]. The derived albedo map from the calibrated RGB and NIR reflectance bands is shown in Fig. 3b).

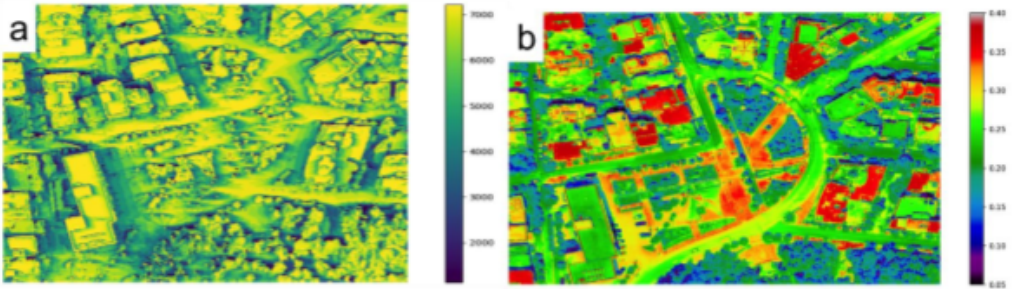


Fig 3. a) Map of cumulative daily solar radiation in (W h m^{-2}) on June 20th 2017; b) Albedo map derived from calibrated RGB and NIR reflectance maps.

3.2 Temperature maps

From the derived temperature maps the diurnal temperature amplitude (DTA) was computed from the maximum and minimum surface temperature observations. The DTA maps obtained from June 19th and 20th 2017 are shown together with the one from April 12th 2016 [8,9] in Fig. 4. The DTA distribution on June 20th presents the highest values and the one from June 19th has considerably lower values, e.g. the DTA values of the asphalt ranges between approximately 15 to 20 degrees on the 19th, whereas the values on June 20th vary between 25 and 35°C. For the April 12th 2016 the DTA values vary from 25 to 35°C, hence very similar to the ones from June 20th 2017. This corresponds well with the weather data from the three days, i.e. some clouds in the middle of the day on June 19th, whereas a clear and sunny day on the 20th and April 12th. All three maps also indicate that the asphalt has the highest temperature difference of all the materials, between 30 and 40 degrees as indicated on the map from June 20th 2017. The variation of DTA of marble is smaller than asphalt as shown consistently on all three maps. Again on June 20th 2017 the difference in marble's temperature was the

highest, around 28 degrees. Also all three maps suggest that the temperature difference in the park (lower part of the images) is among the lowest in the area with a temperature difference in the park of approximately 15 degrees in Fig. 4 a) and b) while the maximum temperature difference for vegetation seems to be around 20 degrees in Fig. 4 c). This indicates that the diurnal variation in temperature in the areas with vegetation is considerably smaller than the variation in the temperature of asphalt and marble.

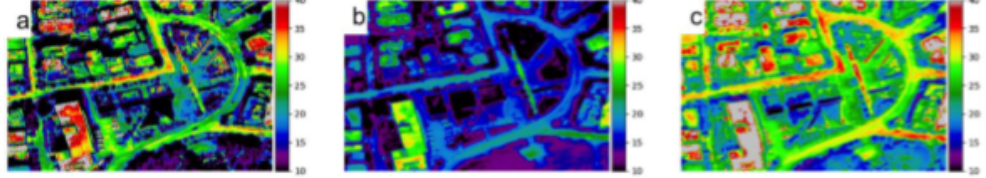


Fig 4. Diurnal temperature amplitude maps, difference between maximum and minimum temperature (in $^{\circ}\text{C}$) of the day from a) April 12th 2016, b) June 19th 2017 and c) June 20th 2017.

The DTA observations coincide well with maps of ATI weighted with solar radiation, as shown in Fig. 5. The ATI values seem to be higher for the map from June 19th 2017 compared to the map from June 20th 2017 and April 12th 2016. The reason for that can be found in the DTA-maps in Fig. 4 in connection with equation (3). The temperature difference on these two days was higher and thus the ATI-maps have lower values. Looking at each map separately it can be observed that the highest values of ATI, 0.08 K^{-1} and above, are displayed in the areas with the lowest temperature differences such as vegetation and water. ATI values for asphalt and marble, however, appear to be the same on both maps even though there is visible difference in their variation in temperature as mentioned above. A reason for that could be that marble has higher albedo values, above 0.30, while asphalt has lower albedo values, slightly above 0.20, also reported in [9]. Marble also has the highest thermal conductivity compared to the other examined materials (asphalt, concrete, and vegetation). It should also be noted that there was heavy precipitation on June 18th and the soil was still moist at the beginning of the survey on June 19th. This can be seen in the areas with bare soil (see Fig. 1) on the ATI images, since these areas have very different values between June 19th, where the soil was still moist, and June 20th where it had dried. This difference is not as apparent in the park in the lower part of the image since the temperatures recorded here is mainly the temperatures of the three tops

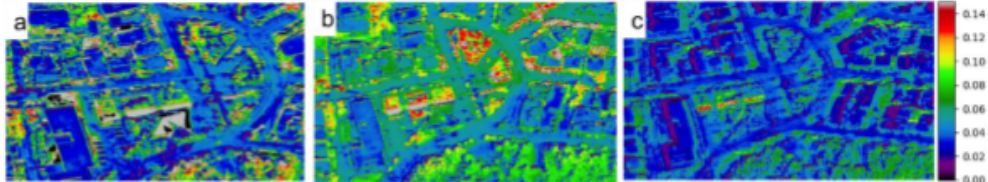


Fig 5. Apparent thermal inertia (ATT) weighted with the solar radiation for each pixel, from a) April 12th 2016, b) June 19th 2017 and c) June 20th 2017.

3.3 Temperature time series

As an alternative to maps of ATI, the thermal properties of the materials can be derived from the time series of the temperature maps. The average temperature for different materials in regions with areas with little or no shade during the day over is plotted with time in Fig. 6. Note however that at 17:00 some of the areas of soil, tiles and concrete had been in shade for a few hours, hence introducing larger uncertainties for these points. The solar radiation measured at the site is also plotted with a time sampling of one hour. It can be seen that the materials with low thermal inertia, or ATI (see Fig. 5) have steeper curves and higher amplitude than the materials with high ATI.

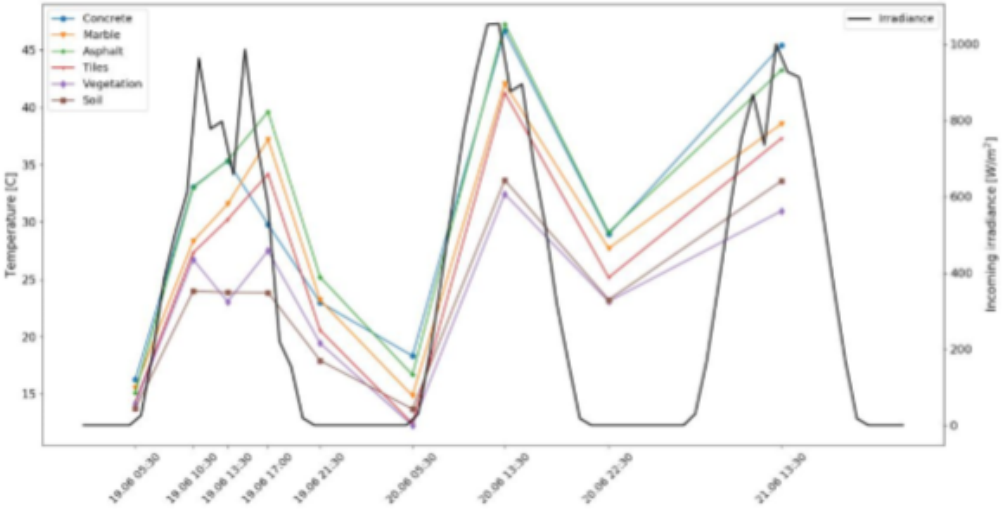


Fig 6. Temperature curves of different materials from early morning on June 19th until noon June 21th. Also plotted in solid black is the solar radiation.

Based on the measured temperatures and the solar angle in Athens derived from [21] the simple parameterization approach proposed in [11] could be adopted. Fig. 7 shows the simple parameterization of asphalt, marble and vegetation. The curves display a sinusoidal curve where the phase and amplitude are determined from the measurements and the measurement points overlaid. Each of the three curves then represents a linear relation between the maximum solar elevation during the day and the maximum difference $T_s - T_{air}$, as described in Eq. 1. It can be seen that the measurement points are lower than the modeled ones for all three materials, and the difference is higher than the error uncertainties on the measurements. There are several reasons for these differences. Firstly, the maximum temperature of the day was not really measured since flights were only performed at 13:30 and 17:00. Secondly, the weather was cloudy on June 19th and followed a heavy rainfall and the measurements are therefore not really suited for this model, since it is required that the measurements must be undertaken in a clear and dry day [11]. Thirdly, there are big variations within each material. There are for examples at least two types of asphalt in the area. And finally, the materials are subject to weathering, which might change the albedo. The albedo of the material is not taken into account in this simple parameterization model.

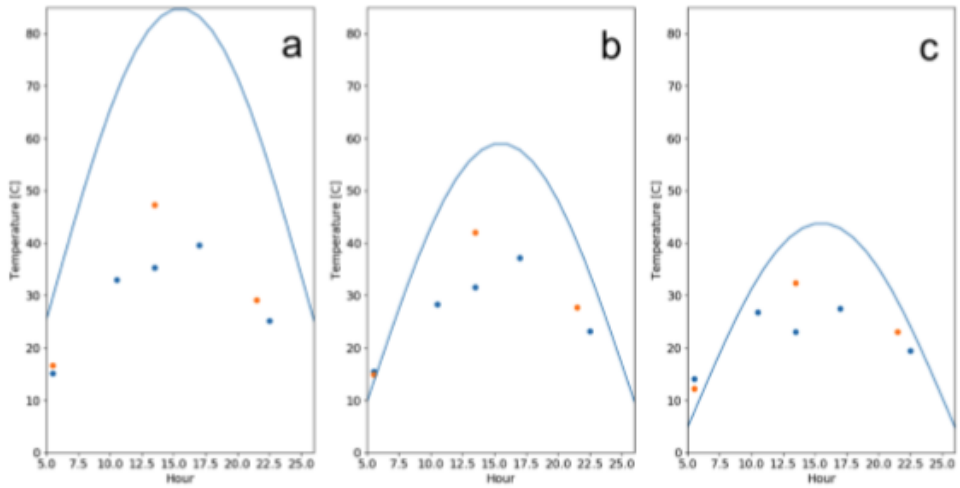


Fig 7. Sinusoidal modeling of temperature using the simple parameterization model from [9] with measurements from June 19th (blue) and June 20th (orange).

4 CONCLUSION

Due to the strong heterogeneity of surface characteristics, the surface temperature varies in space as well as in time and an adequate characterization requires measurements with detailed spatial and temporal sampling. UAV survey provides potential for very high resolution mapping at a user-defined frequency. The results confirm that aerial survey of urban materials is well suited approach for classifying materials at the urban fabric and providing information about their physical properties.

The thermal properties seem to be well modeled with the ATI derived from the measurements. The ATI weighted with incoming solar radiation is a good indicator of the surface temperature during the daily cycle for dry materials. For moist materials such as soil and vegetation the relation is different which need to be taken into account when modeling the surface temperature.

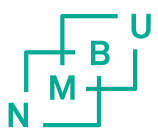
For the simple parameterization of the thermal properties based on solar angle and maximum temperature difference, there appeared to be four main limitations: 1) the radiometric accuracy of the thermal camera and 2) the variations in the local weather conditions, 3) the variations within the materials and 4) influence of albedo.

Future studies are planned where the parameterization model from [11] is applied on the measurements used as input for numerical simulations of the surface temperature of the materials.

REFERENCES

- [1] Landsberg H.E. (1981) *The Urban Heat Island*, Academic Press NY
- [2] Voogt, J.A., Oke, T.R., "Thermal remote sensing of urban climates," *Remote Sensing of Environment* 83, 370-384 (2003)
- [3] M. Sohrabinia et al, "Soil moisture derived using two apparent thermal inertia functions over Canterbury, New Zealand", *J. Appl. Remote Sens.* 8(1), 083624 (doi:10.1117/1.JRS.8.083624) (2014)

- [4] Berwal, S., Kumar, D., Singh, V.P., Pandey, A.K., Kumar, K., "Dynamics of thermal inertia over highly urban city: A case study of Dehli", Proceedings of SPIE, 1008, pp7 (2016)
- [5] Zhan, W., Chen, Y., Voogt, J. A., Zhou, J., Wang, J., Ma, W., Liu W. "Assessment of thermal anisotropy on remote estimation of urban thermal inertia", Remote Sensing of Environment 123, 12-24 (2012).
- [6] Y.Qin, "Pavement surface maximum temperature increases linearly with solar absorption and reciprocal thermal inertia", International Journal of Heat and Mass Transfer 97, 391-399, (2016)
- [7] Van doninck, J. et al, "The potential of multitemporal Aqua and Terra MODIS apparent thermal inertia as a soil moisture indicator," International Journal of Applied Earth Observation and Geoinformation 13, 934-941 (2011).
- [8] Burud, I., This, T., Gaitani, N., "Reflectance and thermal properties of the urban fabric studied with aerial spectral imaging" SPIE Proceedings Vol. 10444, Fifth International Conference on Remote Sensing and GeoInformation of the Environment (2017)
- [9] Gaitani, N., Burud, I., This T., Santamouris, M., "High-resolution spectral mapping of urban thermal properties with Unmanned Aerial Vehicles." BUILDING & ENVIRONMENT (available online: <https://doi.org/10.1016/j.buildenv.2017.05.027> (2017)
- [10] Bogren, J., Gustavsson, T., Karlsson, M., Postgård, U. "The impact of screening on road surface temperature." Meteorol Appl 7:97-104 (2004)
- [11] Lindberg, F., Holmer, B., Thorsson, S., "SOLWEIG 1.0 – modeling spatial variations of 3D radiant fluxes and mean radiant temperature in complex urban settings. Int. Biometeorol 52:697-713, (2008)
- [12] Lindberg, F., Onomura, S., Grimmond, C.S.B. "Influence of ground surface characteristics on the mean radiant temperature in uban areas." Int J Biometeorol 60(9):1439-52, (2016)
- [13] M. Jaud, et al. "Method for orthorectification of terrestrial radar maps." ISPRS Journal of Photogrammetry and Remote Sensing 97, 185-194 (2014)
- [14] (<http://owl.phy.queensu.ca/~phil/exiftool/>)
- [15] Congedo, L., "Basic tutorial 1: Land Cover Classification of Landsat Images," <<https://fromgistros.blogspot.com/2018/02/basic-tutorial-1.html>> (2018)
- [16] PIX4d Software: <https://pix4d.com/> Accessed on
- [17] Minkina, W. and Dudzik, S. 2009. Infrared Thermography: Errors and Uncertainties. Wiley Press, 192 pp. (2009)
- [18] <https://www.rdocumentation.org/packages/Thermimage/versions/2.2.3/topics/raw2temp>
- [19] Oltra-Carrio, R. Sobrino, J. A., Franch, B., Nerry, F., «Land surface emissivity retrieval from airborne sensor over urban areas», Remote Sens. Of Environment, 123, 298-305,(2012)
- [20] http://urban-climate.net/umep/UMEP_Manual
- [21] Bird, R. E., and R. L. Hulstrom, *Simplified Clear Sky Model for Direct and Diffuse Insolation on Horizontal Surfaces*, Technical Report No. SERI/TR-642-761, Golden, CO: Solar Energy Research Institute, (1981)



Norges miljø- og biovitenskapelige universitet
Noregs miljø- og biovitenskapslelege universitet
Norwegian University of Life Sciences

Postboks 5003
NO-1432 Ås
Norway